2014

Stable Isotopes of Fluid Inclusions in *L. pertusa* and *M. annularis*

An application to paleotemperature determination

VU University Amsterdam
Frans Keijzer 1919857

Master Research Project
Earth Sciences (Solid Earth)
AM 450200 (27 ECTS)

Abstract

This is a study based on determining the stable isotope composition of fluid inclusions of cold- and warm-water corals from the Bahamas and Curaçao respectively. Geochemical data were obtained using a new online technique called the 'Amsterdam Device' which comprises δ^2H and $\delta^{18}O$ analyses of fluid inclusions with a continuous-flow crushing device.

The first goal of this study is to test the stable isotope variations in the fluid inclusion of the cold-water coral *L. pertusa.* This study aligns with the first analysis of Feenstra E.J., 2013, which suggested the included fluid is not of seawater composition. Like Feenstra E.J., the average stable isotope composition of the inclusion fluid is higher in $\delta^{18}O$ and lower in δ^2H in relation to seawater, indicating that the fluid in cold-water corals is not of seawater composition. This is likely due to non-equilibrium fractionation effects of the coral. Kinetic fractionation effects could explain the simultaneous depletion of $\delta^{18}O$ and δ^2H. However, this can not explain the fact that $\delta^{18}O$ is enriched with respect to isotope equilibrium for aragonite. Rayleigh fractionation should be considered as possible mechanism for the isotope variations in fluid inclusions, since the chemical system is open and the trend is similar to the Global Meteoric Water Line.

The second goal of this study is to test whether or not the included fluid can be used for paleotemperature determination. For this technique, the ambient seawater composition during time of coral growth (δ_w) is needed, however, it has been identified as a limitation of oxygen isotope paleothermometry.

Since the data suggests fluid inclusions in *L. pertusa* are not of seawater composition, the inclusions do not represent (δ_w) and therefore this technique does not work on this particular coral species. However, the data of *M. annularis* fluid inclusions suggests no complex fractionation effects and that this fluid is of seawater composition since the $\delta^{18}O$ is approximately the same as seawater. Paleotemperature calculations using the oxygen isotope composition of the included water confirm this statement. Therefore, fluid inclusions in *M. annularis* might be representative for the ambient seawater during the time of coral growth and offer a solution for the identified limitation of oxygen paleothermometry. Therefore, this new technique could in principle be of great value for marine climatic reconstructions.

Since this study focuses mainly on paleotemperature determination, average positive hydrogen composition in relation to SMOW is assumed to be of minor importance in relation to oxygen.

Table of contents

1. Introduction

1.1 Previous Research

Over the past few decades, stable isotope analysis on fluid inclusions has played a more dominant role in climate reconstruction. Schwarcz et al. (1976) first discovered that the oxygen isotopes of fluid inclusions in speleothems can be used to estimate $\delta^{18}O_w$ of the seepage water from which a speleothems was deposited, since the inclusions are assumed to preserve their oxygen and hydrogen isotopic ratios since the time of deposition. They crushed the calcite samples under vacuum and the liberated water was collected in break-seal tubes. In 2006, Vonhof et. al. designed a relatively low cost continuous-flow technique for the analysis of fluid inclusions in speleothems.

In addition to speleothems, the skeletons of calcareous marine organisms such as corals and foraminifera also play a major role in reconstructing the particular dynamic environment in which they inhabit. In 1947, Harold Urey first noticed that during calcium carbonate precipitation the oxygen isotope fractionation provides a potential paleothermometer. Subsequently, this was tested experimentally by McCrea (1950) and calibrated with biogenic carbonate by Epstein (1951; 1953). However, these researchers identified two limitations of oxygen isotope paleothermometry: The first limitation concerns the fact that paleotemperature determination depends on the knowledge of the $\delta^{18}O$ composition of the ambient seawater. The second limitation is related to the fact that biogenic calcium carbonate may not always be precipitated in equilibrium with the water.

Epstein et al. (1953) analyzed calcite and biogenic aragonite at temperatures between 7 and 30°C and they constructed a calcium carbonate paleotemperature scale, which is still used nowadays. They re-determined their previous relationship between temperature and $\delta^{18}O$ using modified procedures for removing organic matter.

However, the isotopic equilibrium of oxygen in aragonite is less well known than calcite. At 25°C, calcite is slightly depleted in $\delta^{18}O$ relatively to inorganic aragonite by 0,6‰ (Tarutani et. al., 1969). Grossman and Ku (1986) constructed a temperature dependence of the aragonite-water paleotemperature equation:

$$T\,(^{\circ}\ C) = 20.6 - 4.34(\delta^{18}O_{ar} - \delta_w)\ ,$$

in which $T\ (^{\circ}\ C)$ is the temperature in degrees Celcius, the $\delta^{18}O_{ar}$ reflects the oxygen isotope composition of the aragonite skeleton of the scleractinian and δ_w is the oxygen isotope composition of the ambient seawater. Grossman and Ku observed a strong covariance between different aragonitic organisms. Therefore, Grossman and Ku constructed individual formulas for foraminifera and gastropods. In addition, Leder et. al., (1996) focused on the $\delta^{18}O$ of the coral *Montastrea annularis.* They suggested that the relationship between temperature and the $\delta^{18}O$ of the coral could be expressed by the equation:

$$T\ (^{\circ}\ C) = 5.33 - 4.519(\delta^{18}O_{ar} - \delta_w)\ ,$$

in which again $T\ (^{\circ}\ C)$ is the temperature in degrees Celcius, the $\delta^{18}O_{ar}$ reflects the oxygen isotope composition of the aragonite skeleton of the scleractinian coral and δ_w is the oxygen isotope composition of the ambient seawater.

1.2 Fluid Inclusions

Studies on fluid inclusions in scleractinian corals are scarce. However, Gaffey (1988) identified that significant amounts of water (up to 3%) occur in skeletal carbonates as minute inclusions that is readily released during heating. In addition, Cuif and Dauphin (2005) concluded that it is likely that water is present in coral skeletons. They studied the structural and chemical elements of the fine scale growth patterns of fibers in coral skeletons and stated that glucids (carbohydrates) are present in the fiber mineralizing compounds of the coral which include water in their complex molecular assemblages. They also suggested that organic material associated with the coral skeleton is hydrated, since they showed that the main part of the water is linked to organic compounds up to 275 – 330°C.

During the study of Feenstra (2013), the samples were heated up to 110 - 120°C and significant amounts of water were measured after crushing the samples, indicating that this water is not linked to organic compounds but might occur as fossilized included fluid.

1.3 Isotope fractionation effects

As mentioned earlier, the second limitation of oxygen isotope paleothermometry is related to the fact that biogenic calcium carbonate may not always be precipitated in equilibrium with the water. This results in significant distortion of temperature signals. The offsets from equilibrium are not yet well understood (Marali et al., 2013). However, different processes such as 'vital effects' (Adkins et al., 2003), kinetic fractionation (McConnaughey, 1989) and Rayleigh fractionation (Gagnon et al., 2007) are suggested.

The 'vital' effects or biological fractionation effects (Weber and Woodhead, 1971) are caused by biological processes such as metabolism, enzymatic responses, photosynthesis, and biomineralization. Vital effects are characterized by a positive offset of the $\delta^{13}C$ (Figure 1.3.1) relative to the linear isotope kinetic trend. Since symbiotic micro-algae in photosynthetic corals prefer ^{12}C, the carbon pool in zooxanthellate corals is enriched in ^{13}C (McConnaughey, 1989a)

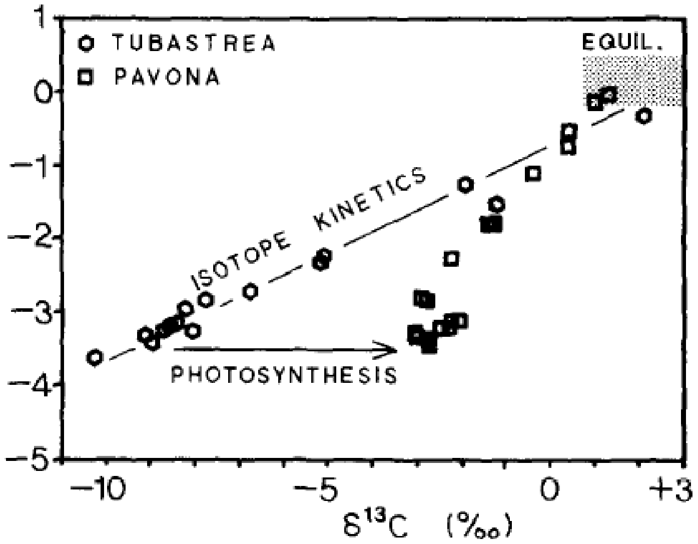

Figure 1.3.1: *Plot of $\delta^{18}O$ versus $\delta^{13}C$ of isotopic chemistry of photosynthetic coral Pavona clavys and non-photosynthetic coral Tubastrea sp. The ' vital effects' (photosynthesis) are represented by an increase of $\delta^{13}C$ relative to the isotope kinetics. The isotope fractionation effects (isotope kinetics) are represented by a simultaneous depletion of* of $\delta^{13}C$ and $\delta^{18}O$ (after McConnaughey, 1989a).

Kinetic isotope fractionation effects are caused by CO_2 hydration and hydroxylation (McConnaughey, 1989a) and are characterized by a simultaneous depletion of $\delta^{13}C$ and $\delta^{18}O$. Strong kinetic depletions tend to occur in rapidly growing skeletons (McConnaughey, 1989a).

Rayleigh fractionation, which is called after ' Lord Rayleigh', is an isotope fractionation process which describes an exponential relation between the partitioning of two reservoirs as one reservoir decreases in size (Kendall and McDonnell, 1998). Rayleigh fractionation should only be applied to chemically open systems where the isotopic species remaining in the system at the moment of removal are in isotopic and thermodynamic equilibrium with the isotopic species which are removed at every instant. Gagnon et al. (2007) observed increasing Mg/Ca with decreasing Sr/Ca outside of the central band of calcification in scleractinian cold-water coral samples of *Desmophyllum dianthus.* They explained the isotopic behaviour by Rayleigh fractionation from a closed pool: 'anytime there is a closed system and a tracer is discriminated against or preferentially incorporated during co-precipitation, Rayleigh fractionation occurs'.

1.4 Lophelia pertusa

The distribution of the cold-water coral *Lophelia pertusa* extends from New-Zealand to the west coast of North-America but mainly throughout the Atlantic Ocean (Rogers, 1999). It also occurs extensively in the Caribbean Sea and Gulf of Mexico (Fig 1.4.1). The coral occurs at a range of depths of 50 to 2000 meters (Freiwald and Roberts, 2005).

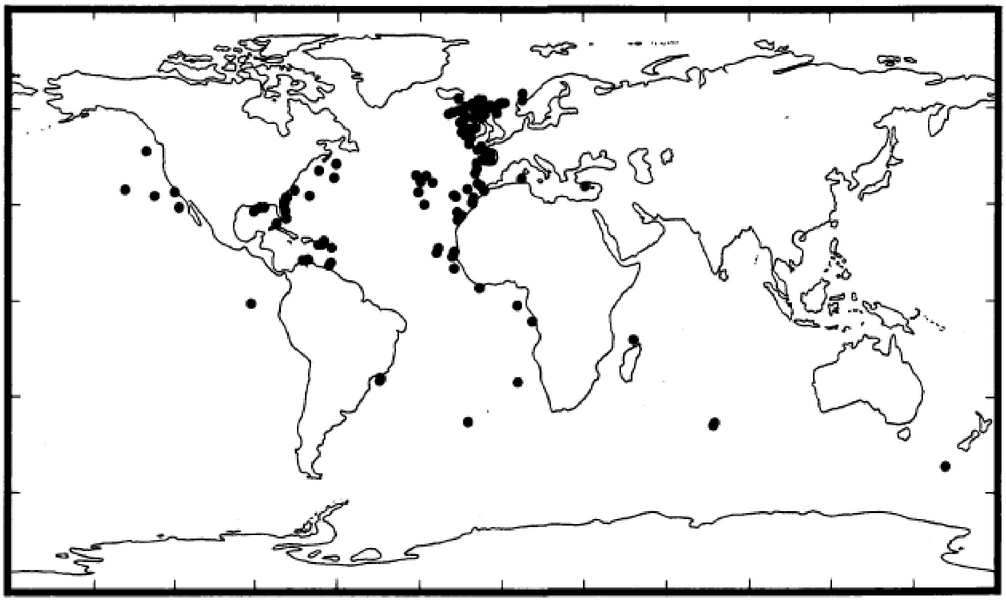

Fig 1.4.1: *Global distribution data of L. pertusa occurences (after Rogers, 1999).*

Initially, a *Lophelia pertusa* colony develops on a piece of hard substrate (Wilson, 1979b) and can form mound structures with relief exceeding 300 meters (Van Weering, 2003). The coral prefers water temperatures between 4 and 13^{0}C and zones where tidal currents and internal waves occur to transport sufficient food particles (Mienis et al., 2007). In addition, high currents prevent the corals to be buried by sediments.

Macroscopically, *Lophelia pertusa* has an extrovert, introvert and elongate morphotype (Fig 1.4.2). In all morphotypes, the rate of skeletal growth is highest during juvenile stages with a decreasing trend when becoming adult (Freiwald et. al., 1997). Regarding skeleton growth, there is a distinct difference between the different morphotypes. Whereas the extro- and introvert types clearly produce annual patterns with the full scale of tree-rings laid down over the corralite (Fig 1.4.2A-B), the elongate morphotype does not produce the full scale of tree-rings over the entire of the corralite (Fig 1.4.2C)

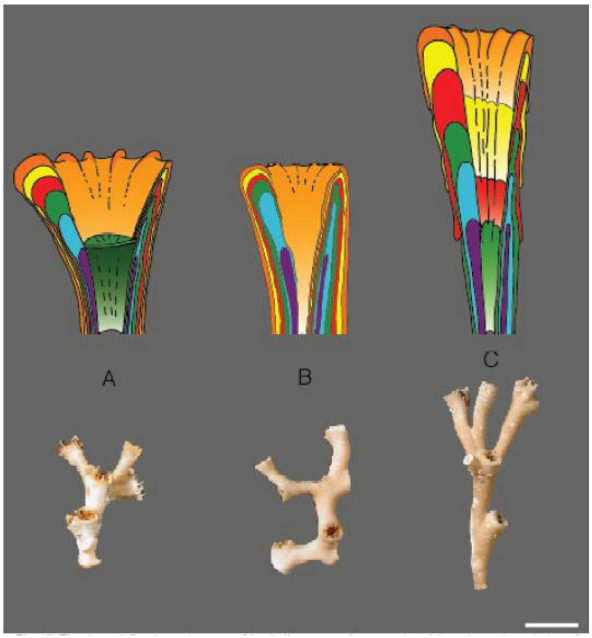

Fig 1.4.2: *Upper row: the schematic evolution of presumably annual increments of (A) extrovert, (B) introvert and (C) elongate morphotypes of Lophelia pertusa. Lower row: The three defined morphotypes of Lophelia pertusa (after Kaszemeik and Freiwald, 2003).*

In general, *Lophelia* polyps build carbonate exoskeletons of fibrous elongate aragonite crystals and granular crystals, both can be found in any skeletal elements such as septa, inner theca wall and outer theca wall (Pratz, 1882). The fibrous crystals radiate from the granular crystals, which are the centers of calcification (Gagnon et al., 2007). A thin section from the study of Kaszemeik and Freiwald (2003) clearly shows that both the theca and the septa contain centres of calcification (Fig 1.4.3)

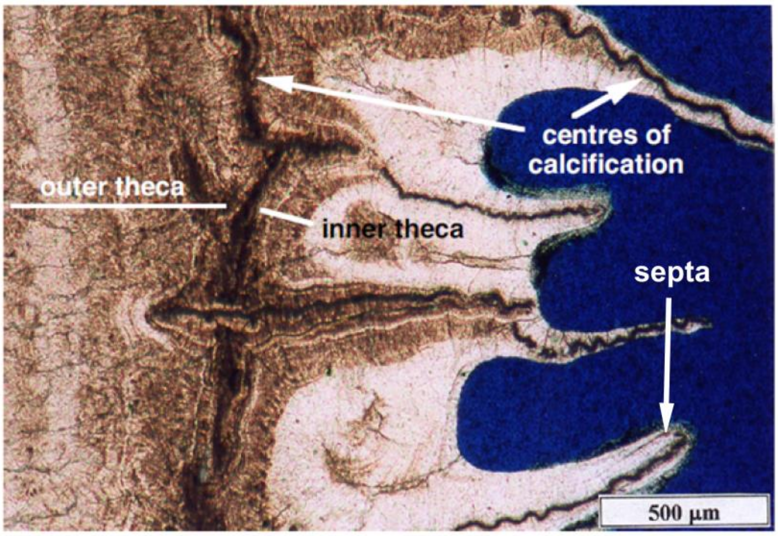

Fig 1.4.3: *Thin section of a Lophelia pertusa skeleton indicating the major skeletal elements and the centres of calcification. Both the septa and the theca contain centres of calcification, which are black on this thin section (modified after Kaszemeik and Freiwald, 2003)*

1.5 Montastrea annularis

Montastrea annularis is a scleractinian which is considered to be one of the most dominant coral species of modern western Atlantic reefs (Goreau, 1959). *M. annularis* ranges in depth from the intertidal to over 80 m (Goreau and Wells, 1967) and it is distributed geographically from Bermuda (Logan, 1988) to Brazil (Laborel, 1969), throughout the Caribbean Sea.

Fig 1.5.1: *Global distribution of M. annularis (after Veron and Stafford-Smith, 2002)*

Knowlton and Weil (1994) suggested a partitioning of the *Montastrea annularis* species into three separate species. Next to *M. annularis*, they identified *M. faveolata* and *M. franski* as being significantly different species in comparison to *M. annularis*.

Macroscopically, *M. annularis* occurs as branching, lobate plocoid colonies formed by long, thick disjunct columns (Weil and Knowlton, 1994). The columns often wide distally and are formed by extratentacular buddings of small polyps (Fig 1.5.2A). Only the top parts of these columns are covered by living tissue. In contrast to the other species, margins on the sides of columns are typically senescent (Weil and Knowton, 1994). Corralites occur on top of the columns and distributed equally which gives the top of the columns a smooth appearance (Fig 1.5.2B)

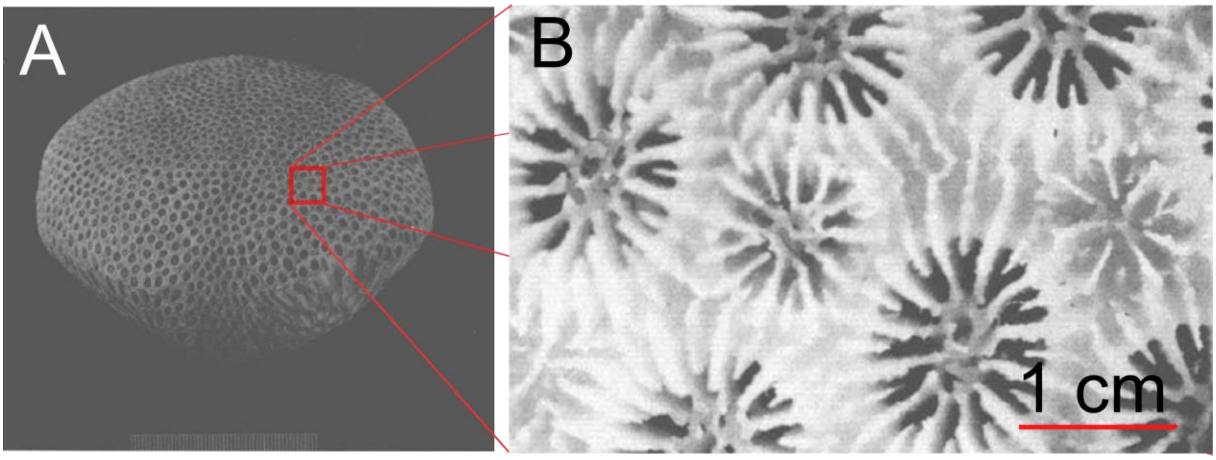

Fig 1.5.2: (A): *Photograph of the holotype M. annularis. Scale markings are in mm.* ***(B)*** *Photograph of the corralites which occur on top of the columns (modified after Weil and Knowton, 1994).*

Like *L. pertusa*, *M. annularis* is built up of aragonite crystals which are formed by zooxanthellatic algae that reside within the tissue of the corals (Barnes and Taylor, 1973). However, the rate of calcification of *Montastrea* strongly depends on the light intensity. Therefore, the average rate of coral calcification decreases with increasing depth (Goreau, 1959). Consequently, the density of its skeleton increases with depth, since fast growing corals are less dense than slowly growing corals (Wells, 1956).

Microscopically, the skeleton of *M. annularis* consists of cycles of high density (HD) and low density (LD) bands which are proved to be annual (Dodge, 1974). Weber (1975) considered the HD bands to form in the months of warmest water temperature. Dodge (1974) interpreted the skeleton of *M. annularis* to be comprised of an endo- and an exothecal part (Figure 1.5.3). The endothecal area consists of the polyp's skeleton which is a vertical tube or corallite wall in which plates radiate vertically from the tube's center. The vertical features are interpreted as septa when they occur in the endothecal part and as costa when they occur in the exothecal part. The exothecal part consists of a mosaic of void space, costa en dissepiments. Dissepiments are horizontal cut offs of coral tissue from the lower parts of the skeleton. HD banding primarily results from the thickening of exothecal septa (costa) and dissepiments.

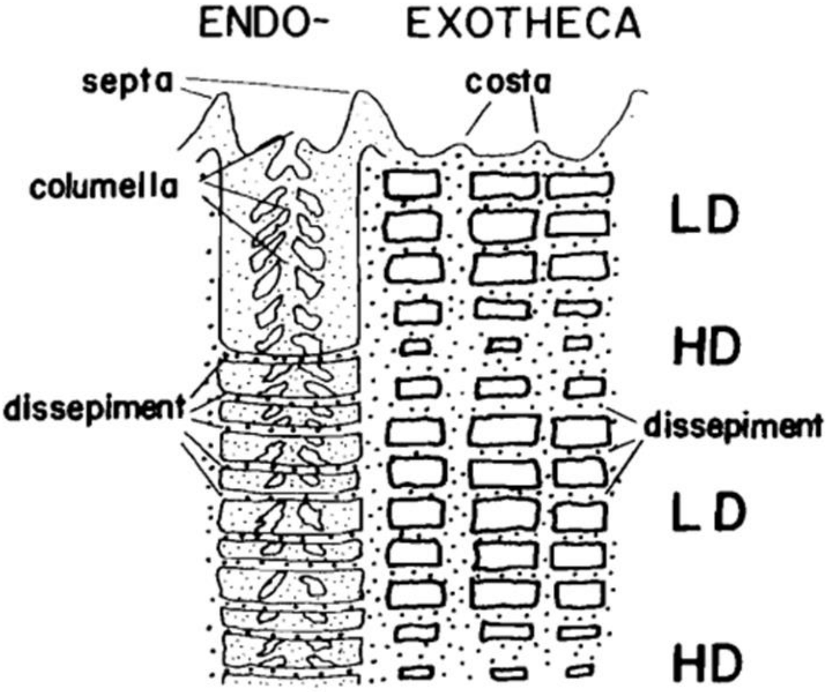

Figure 1.5.3: *Schematic illustration of the interpretation of the skeletal structure of M. annularis of Dodge (1974), indicating the main skeletal elements and the areas of HD and LD banding.*

1.6 Biomineralization

To fully understand the isotope variations of the fluid inclusions and skeletal carbonate of corals, it is important to understand how the skeletons made of calcium carbonate are formed. The coral skeletons described above are both the result of the process of biomineralization. Biomineralization is the study of the formation, properties and structure of inorganic solids deposited in a biological system (Mann, 2001). Nowadays, coral exoskeletons are composed of aragonite crystals which are formed due to triggering of the calicoblastic basal ectoderm of the coral polyp’s tissue (Kaszemeik and Freiwald, 2003).

In general, coral calcification comprises two ions that make the following reaction in which calcium carbonate is directly precipitated from seawater (Tambutté, 2011):

$$\mathrm{Ca^{2+} + CO_3^{2-} \Leftrightarrow CaCO_3} \qquad (1)$$

However, carbonate ions may also be formed from bicarbonate (2) or CO_2 hydration (3):

$$\mathrm{Ca^{2+} + HCO_3^{-} \Leftrightarrow CaCO_3 + H^{+}} \qquad (2)$$

$$\mathrm{CO_2 + H_2O + Ca^{2+} \Leftrightarrow CaCO_3 + 2H^{+}} \qquad (3)$$

Over the years, many models of coral calcification have been presented. However, the model of McConnaughey (1989a) has been generally accepted. McConnaughey suggested that the area in which the calcium carbonate precipitates, which he named extracellular calcifying fluid (ECF), is located between the skeleton and the calicoblastic membrane. Figure 1.6.1 is a schematic representation of the precipitation model of McConnaughey (1989a). The bilipid layer is impermeable to ionic transport. Therefore, Ca^{2+} can be transported to the ECF by two pathways. Either it is pumped by an enzymatic system, represented by Ca-ATPase, or it leaks in from the surrounding seawater, as in an open system (Ip et al., 1991). Similar to calcium, carbon can also be transported to the ECF by two pathways. Either it can enter the ECF by diffusive transport from the surrounding seawater, or via diffusion of CO_2(aq) across the cell membrane.

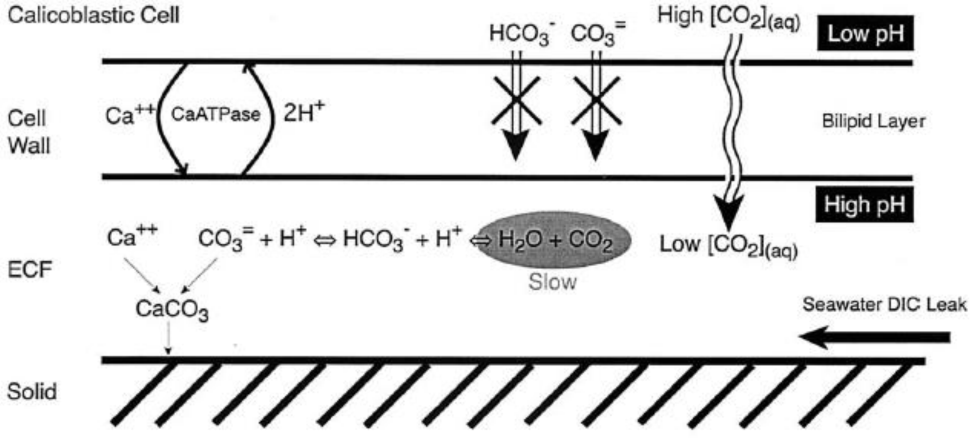

Figure 1.6.1: *A schematic representation of the coral calcification model of McConnaughey (1989a) in which the area of carbonate precipitation is named the extracellular calcifying fluid (ECF). (after Adkins, 2003).*

1.7 Aims

Whereas the $\delta^{18}O_{ar}$ can be obtained relatively easy from stable isotope analysis on the skeleton of the scleractinian corals, the δ_w is difficult to be obtained and has been identified as a limitation of oxygen isotope paleothermometry.

Hence, the first major aim of this study is to determine the origin of fluid inclusions in both cold and tropical water scleractinian corals and whether or not the water filled voids can be used for paleothermometry. Like Schwarcz et. al. (1986) concluded for speleothems, the isotope composition of fluid inclusions in scleractinian corals can be representative for the paleo-seawater in which the corals grew

This study aims to further test the stable isotope variations of fluid inclusions and skeletal elements of cold water coral *L. pertusa*. The stable isotope variations in the fluid inclusion waters are most likely linked non-equilibrium fractionation effect of the polyp of *L. pertusa* (Van Breukelen and Mienis, 2002 unpublished). This study also tests test the link between skeletal fluid inclusion isotope variation and the bio-mineralization processes of *Lophelia pertusa* from the Bahamas, and compares the results with the study of Feenstra, 2013. Feenstra, 2013 collected *L. pertusa* samples from the Rockall Through, west of Ireland. Both the sedimentological and the oceanographic setting of the Great Bahama Bank research area differs significantly from the settings of the Irish continental slope sites. Therefore, it will be the ideal environment to further test the link between skeletal fluid inclusion isotope variation and the bio-mineralization processes of *Lophelia pertusa.*

In addition, this study also focusses on the fluid inclusions in the tropical coral *Montastrea annularis* from Curaçao. The data of Feenstra (2013) yielded promising results regarding isotope variation of the fluid inclusion, since there was much less variation observed. This indicates no complex fractionation effects and therefore the included fluid might represent the ambient seawater.

Therefore, this study further tests the question whether or not the fluid inclusions in *L. pertusa* and *M. Annularis* are representative for δ_w. If so, this technique could in principle be of great value in reconstructing past marine climates

In the next chapter, the geological setting of the research areas will be discussed summarizing the major geological events concerning the formation of the study area and the presence of corals. Subsequently, the methods will be presented in chapter 3. This section comprises a detailed description of the sampling methods and the geochemical techniques used in this study. Chapter 4 presents the results of the geochemical analyses. In chapter 5, the results of the geochemical analyses will be discussed in detail and the quality of the crush experiments will be evaluated. In addition, the applicability of the fluid inclusions as proxy for paleotemperature determination will be reviewed. Ultimately, the main conclusions of this study will be presented in chapter 6. The appendix contains photographs of the coral specimens in which the sampled parts are indicated and the fluid data of *Lophelia* and *Montastrea.*

2. Geological Setting

This study comprises two study areas: (1) Santaren Channel near the Bahamas and (2) the inner lagoon of Curaçao.

2.1 The Bahama Platform

The first study area, the Bahama Platform, is located in the northeastern part of the Caribbean Sea. The platform comprises multiple shallow water carbonate banks, which extend more than 1400 km from the island of Hispaniola to the coast of Florida (Curran and White, 1995). The banks are separated by inter- or intraplatform basins and troughs that can reach water depths exceeding 4000 m (Curran and White, 1995). For the origin of these basins, three different theories are proposed, which do not confer with each other. The first theory proposes a direct structural control of the existing sea-floor topography in which the deep channels and banks are derived from horst and graben structures (Ball, 1967a; Sheridan et. al., 1988). In the theory, the banks and channels reflect a long-term dynamic equilibrium between erosional (turbidity currents that carve and deepen channels) and normal depositional processes, such as shallow-water carbonate accumulation that keeps up with the platform subsidence (Dietz et. al., 1970). The third theory coins the idea that the present channel and bank interference evolved since the Late Cretaceous. Prior to that, the channel and banks were one ‘megabank’ (Meyerhoff and Hatten, 1974) and was ultimately cut up by rapid subsidence of the canyons and upbuilding of adjacent carbonate banks (Schlager and Ginsburg, 1981)

Tectonically, the Bahama Platform is bordered by the Cuban orogen in the southwest and the Caribbean lithospheric plate in the south. In the northeast, the structure of the Bahama Escarpment fracture zone (Sheridan, 1976) limits the platform. The eastern margin of the platform, which borders the basin of the Atlantic Ocean, is characterized by a precipitous drop as great as 28° to 40° to abyssal depths (Emiliani, 1965).

The platform itself was most likely established in the Late Jurassic during the break-up of Pangaea. During the break-up, the Bahama-Cuban area was a transform zone linking the young Gulf of Mexico and the Atlantic Ocean (Sheridan, 1988). Volcanic activity accompanied the rifting of Pangaea due to the nature of the colliding Caribbean and North American plates. Multichannel seismic reflection data found evidence for this theory in the tilted fault blocks of Jurassic volcaniclastics in the Straits of Florida (Sheridan, 1981). In addition, in the northwestern Bahamas, under the Florida Straits, the Northwest Providence Channel, and the northernmost Tongue of the Ocean, the basement rocks consist of ‘intermediate’ or ‘transitional´ rift crust composed of the Jurassic volcaniclastic tilted fault blocks (Sheridan et. al., 1988). Due to the oblique subduction of the North American plate under the Caribbean plate near Cuba, the orientation of the Bahama Banks is consistent with left-lateral wrench faulting (Sheridan et. al., 1988). This interaction between the Caribbean and North American plates occurred during the Late Cretaceous and Tertiary orogenesis and also caused the Cuban fold- and thrustbelt to be formed (Masaferro, 2002). The zone of deformation associated with the Cuban orogeny extends 100 km to the northeast of Cuba (Fig 2.1.1). The northernmost boundary of this zone is the Santaren Anticline, which is about 8 km wide and 70 km long. Syntectonic sediments, charactarized by seismic onlap indicate tectonic uplift during Neogene times (Masaferro, 2002).

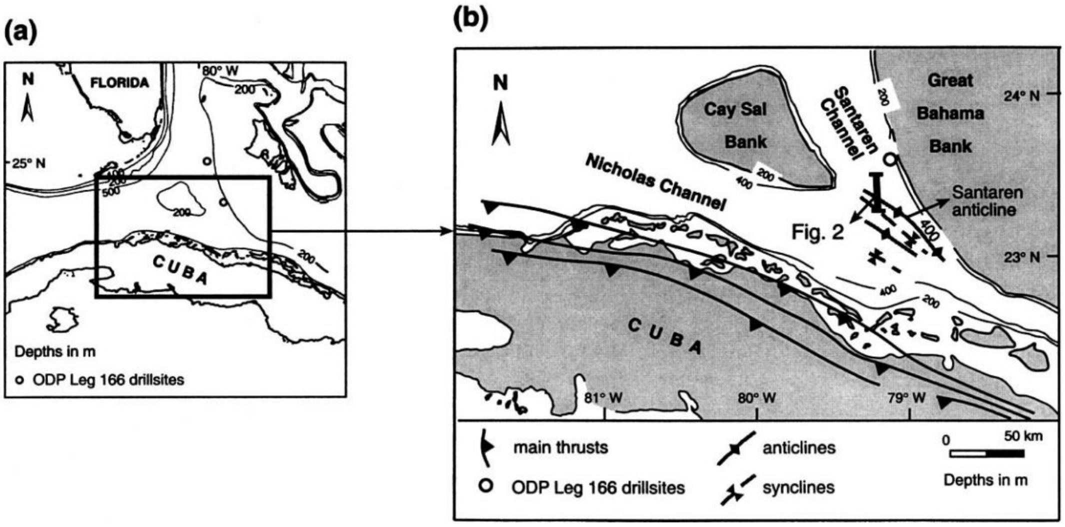

Figure 2.1.1: (A): *Map of central Cuba, southern Florida and the Bahamas.* ***(B)*** *Simplified structural map of the Cuban fold and thrust belt and the Bahamas, indicating the location of the northernmost boundary of the deformation zone (after Masaferro, 2002).*

During the Ocean Drilling Program (ODP) Leg 166, a number of cold water coral mounds were discovered in the Santaren Channel (Fig 2.1.2), at the western side of the Great Bahama Bank (Anselmetti et al., 2000). In addition, Correa et. al. (2012b) documented cold-water coral ridges at the base of the Miami Terrace in the Straits of Florida and are entirely biogenic in origin and are waveform. The cold-water coral ridges are oriented perpendicular to the southward flowing bottom current (Correa et. al., 2012b) and are juxtaposed to a sand dune field free from corals. Both the ridges and the dunes are asymmetrical in shape but face in opposite directions which provides strong evidence that the cold-water corals are not settled on the sand dunes.

Grasmueck et. al. (2007) used an Atonomous Underwater Vehicle to gain more insight in the influence of currents on coral mound morphology and distribution. Their AUV data revealed several trends:

(1) Currents along the western slope of the GBB are tidal dominated and flow both south and northward. Whereas the flow direction in the centre of the Straits is northward, the flow direction along the Miami Terrace slope is southward. Dispite the bi-directional currents, the sediment wedges attached to the coral mounds are pointing in one direction

(2) Taller coral mounds occur in areas which are dominated by bi-direction tidal bottom currents

(3) Uniform bottom current direction causes chains of closely spaced smaller coral mounds to develop

(4) Coral mounds grow into the direction of the currents, suggesting that coral growth, and not sediment accumulation controls the morphology of the mounds.

(5) The orientation of the coral ridges is perpendicular to the main current direction

Trend (4) and (5) align with observations Correa et. al. (2012b) made when documenting the cold-water coral ridges at the base of the Miami Terrace.

Other studies concluded that the average mound distribution in the Santaren Channel site amounts to approximately 14 mounds/km^2 (Correa et. al., 2012). Seismic data shows mound-like structures up to approximately 50 m high above the reflection of the seawater-sediment contact. The mounds appear to be entrenched on a shallow seismic reflection that was interpreted as a seismic sequence boundary (Anselmetti, 2000). The reflection was dated as 0,6 Myr which indicates that the mounds are Middle Pleistocene to Holocene in age.

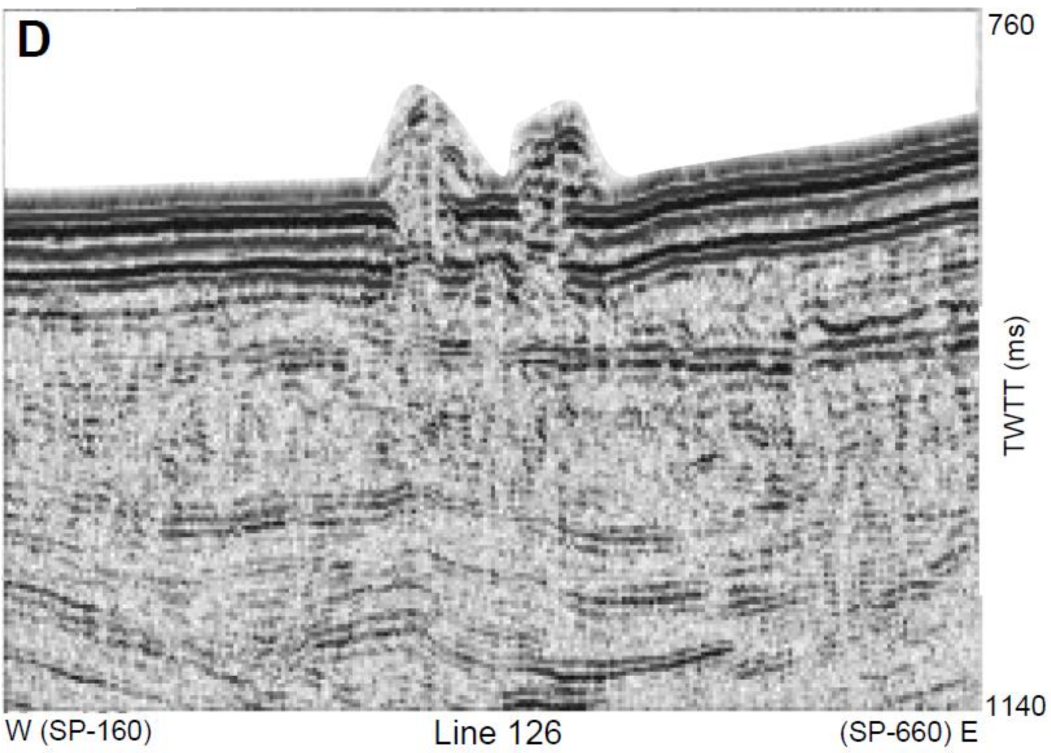

Figure 2.1.2: *Seismic image of examples of mound-shaped lithoherms at the bottom of the Santaren Channel, which are likely formed by deep-water corals. The mounds appear to be entrenched on a shallow seismic reflection that was interpreted as a seismic sequence boundary and was dated 0.6 Myr. (after Eberli et al, 2002)*

Earlier studies concluded that the distribution and morphology of the cold-water coral mounds on the western flank of the GBB are driven by a complex interplay of hydrodynamics, antecedent topography and sedimentation rates (Correa et. al., 2012). These authors constructed a conceptual model illustrating the forces that underlie cold-water coral mound development, distribution and morphology on the slope of GBB (Fig. 2.1.3). In contrast to the ridges situated at the base of the Miami Terrace, the cold-water corals on the slope of the GBB colonize during mound initiation on structural foundations such as turbidites and debris flow deposits (Mullins et al., 1984). This material is derived from the bank top and slope due to submarine sliding which causes mass gravity flow deposits. This sediment export pattern is intimately linked to the configuration of Great Bahama Bank as a flat-topped platform during Late Pliocene and Quaternary times (Eberli & Ginsburg, 1987, 1989). The mound may become partially or entirely buried under high sedimentation rates, or flourish when coral growth and sedimentation rate are near equilibrium (Correa et. al., 2012). This depends on their position with respect to the off-bank sediment depocenters (Fig 2.1.3).

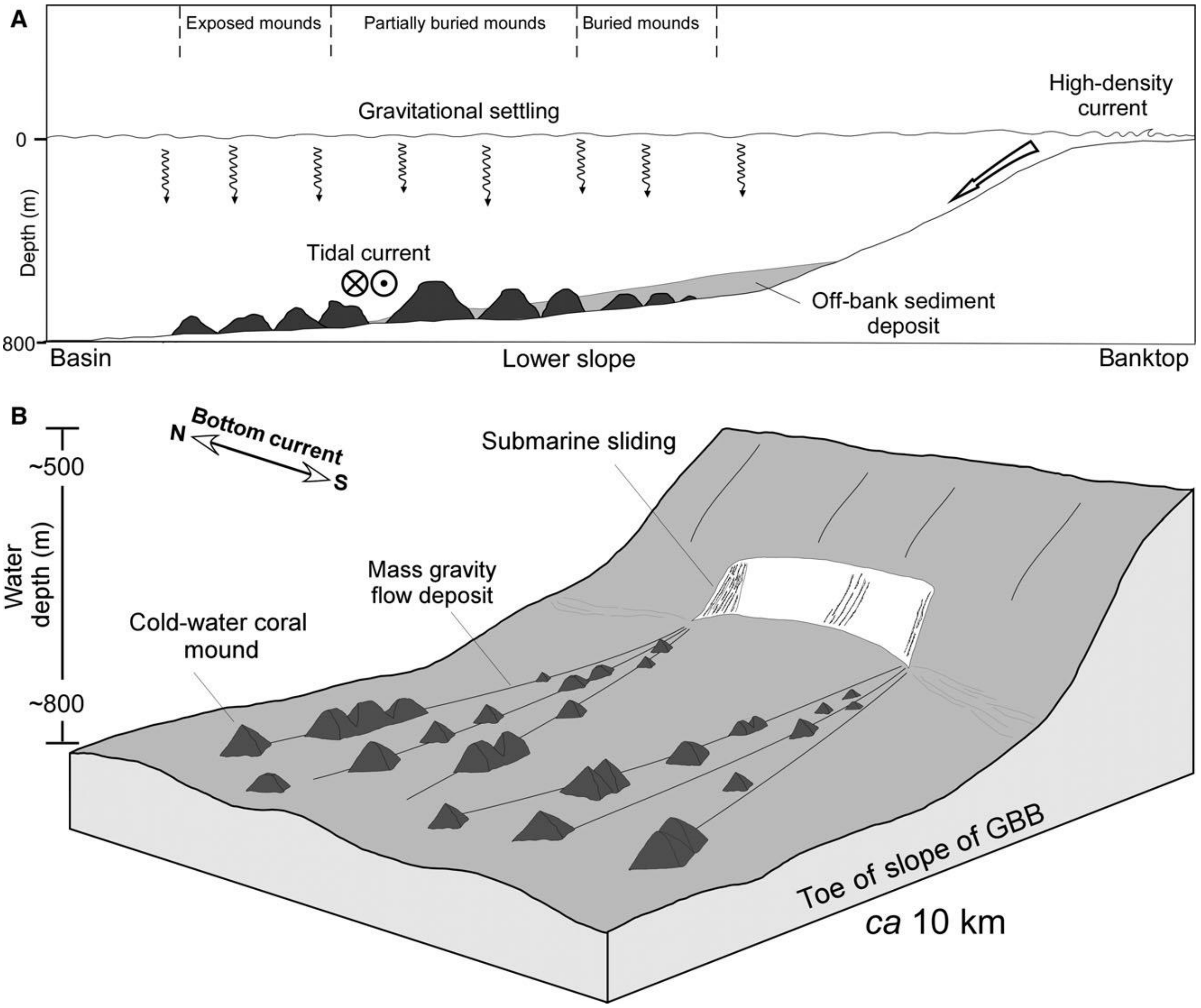

Figure 2.1.3: *Conceptual model of the slope of the Great Bahama Bank, illustrating the forces that underlie the distribution and development of cold-water coral mound.* ***(A)*** *Generalized profile of the slope of the GBB showing various mound sizes. Proximal slopes are buried by off-bank sediment deposits.* ***(B)*** *Illustration of the slope of the GBB showing mass gravity flow deposits. The boulders and debris from the flow deposits can be used as a foundation for cold-water colonies and ultimately, coral mounds (after Correa et. al., 2012).*

The mass gravity flow deposits illustrated and described by Correa et. al. (2012) align with the observations of Mulder et. al. (2012). Mulder et. al. (2012) identified large slope failures and mass transport complexes on the western slope of the GBB by using new high-quality multibeam and seismic data. In addition, the survey revealed erosional and bypass features perpendicular to the platform margin, which suggests that these are the result of energetic downslope processes. Moreover, they identified gully-related turbidite systems and the presence of cold-water coral mounds. Like Correa et. al. (2012), Mulder et al. (2012) suggest that the cold-water coral mounds on the slope of the GBB preferentially seem to settle on topographic highs such as boulders.

2.2 Curaçao

The island of Curaçao is located in the southern Caribbean Sea, and it is part of the Netherlands Antilles, a group of E-W oriented islands located 70 km north of Venezuela. Curaçao is situated on the Venezuelan Borderland, a broad orogenic belt associated with the collision of the South American and Caribbean plates in the late Cretaceous to early Tertiary (Maresch 1974). The island comprises two large antiforms, one in the southeast and one in the northwest of the island. In the centre of these antiforms, the basement is exposed.

The Curaçao basement consists of the Curaçao Lava Formation (Cretaceous basalts) and Tertiary siliciclastic sandstones descended from the basalts (Beets, 1972). The basement is unconformably overlain by the Seroe Domi Formation, a 350 m thick Neogene section of partially dolomitized limestones and silicislastic sandstones cropping out along the leeward coast of Curaçao (De Buisonjé, 1974). On top of the Seroe Domi Formation lies a 60 m thick package of Quaternary Limestone Terraces with fringing and lagoonal reefcoralgal grainstones and boundstones. These terraces where formed during Pleistocene times, when global sea-level changes, along with regional tectonic activity relatively uplifted the island of Curaçao, resulting in the formation of five geomorphologic terraces composed of raised fossil reefs (Alexander, 1961). The Pleistocene tectonic activity caused the shelf area to reduce which resulted in high wave energy in the shallow waters of the windward side of the islands. Therefore, living shallow-water reefs are mainly located on the leeward side and are fringing in nature (Bak 1977).

The leeward reef at Curaçao has been studied extensively over the past 35 yr. It has been divided into 7 zones (Bak, 1975, 1977; Bak and Luckhurst , 1980). The reef is characterized by a gently sloping submarine terrace, which horizontally extends 30-100 m, followed by the drop-off at a depth of 10 to 12 m. From here, the reef steeply slopes to a depth of 50 to 60 m (Figure 2.2.1). Bak (1977) distinguished seven zonal communities along a reef transect on the basis of cluster analysis and reef physiognomy:

(1) the eulittoral Cyanophycean community;

(2) the lower eulittoral community, which is characterized by algae such as *S. polyceratiu* and *L. papillosa;*

(3) the shallow reef community with a depth of 1-4 m and is characterized by the corals *A. palmata* and *D. clivosa;*

(4) the gorgonian community, which has a depth of 4-6 m and is characterized by the gorgonians *P. acerosa* and *P. americana;*

(5) the drop off community has a depth of 6-12 m and is characterized by the coral *M. mirabilis.* In this community*, M. annularis* is dominant;

(6) the roof shingle community on the upper part of the steep slope has a depth of 12-27 m and is characterized by *A. agaricites,* roof shingle-like corals and the roof shingle-like forms of species such as *P. astreoides;*

(7) on the lower part of the steep slope with a depth of 27-50 m, the deep algal community occurs. It is characterized by a conspicuous algal turf, and by a more scattered growth of corals such as *A. lamarckii, A. grahamae* and *M. formosa).*

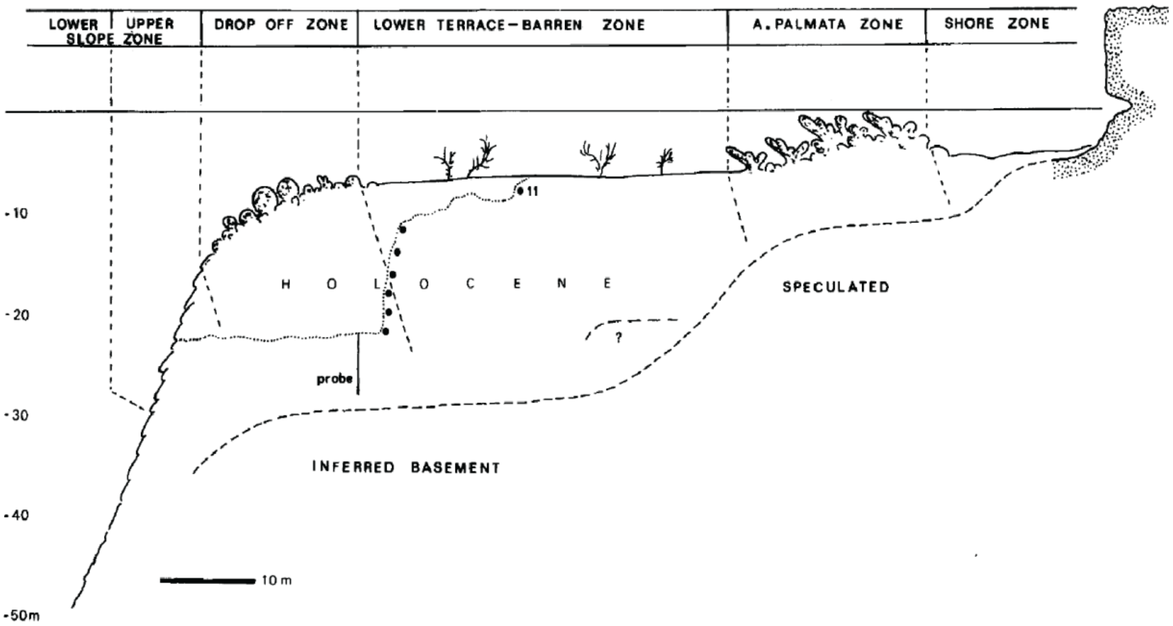

Fig 2.2.1: *COT section through the reef at Bullenbaai, Curaçao illustrating the different zones (after Bak, 1977)*

3. Methods

3.1 Sampling Material

For the first part of the study, samples of *Lophelia pertusa* were collected during the M95 ‘CICARB’ Cruise on the *RV Meteor* that started from Kingston en ended in Point-á-Pitre in April 2013 (Fig 3.1.1). The first CWC samples were taken from known reef occurrences in the Straits of Florida (Fig 3.1.2). These CWC mounds were mapped and studied intensively by Correa et. al., (2012), Grasmueck et. al., (2007), Mulder et. al., (2012).

During the M95 cruise, hydroacoustic surveys discovered several other deep-water coral mounds were in the Santaren Channel, more south of the known deep water reef occurrences in the Straits of Florida. These mounds occurred in patches on the distal slope of GBB (Fig. 3.1.3). At three different sites, including both the known and the unknown reef patches, samples of the CWC mounds were successfully collected (Figure 3.1.4). The samples were obtained using a Van Veen Grab Sampler, a gravity corer and a box corer (Table 3.1). The water depths in which the coral mounds were found ranged from 558 to 599 meters.

The quality of the corals of station 540-1 was poor. From the collected corals from station 541-1 and 583-1, a number of cold-water coral specimens were chosen to use for this study and were given code names related to station number and the tool which obtained the corals (Table 3.2). Subsequently, random polyps of each of the coral specimens were cut off (Fig 3.1.5) to samples of 0,55 – 0.95 g which were used for fluid inclusion analysis.

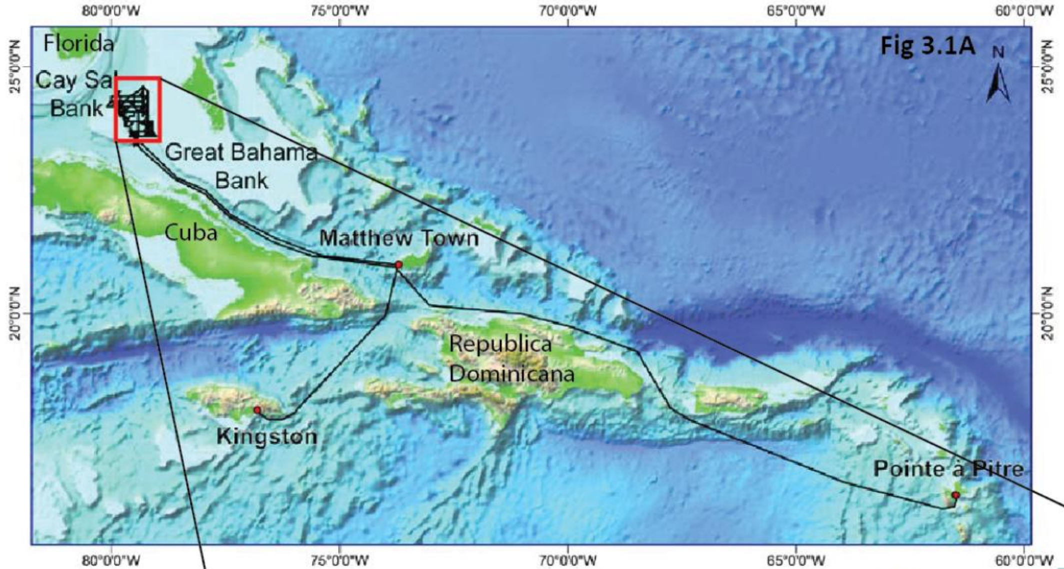

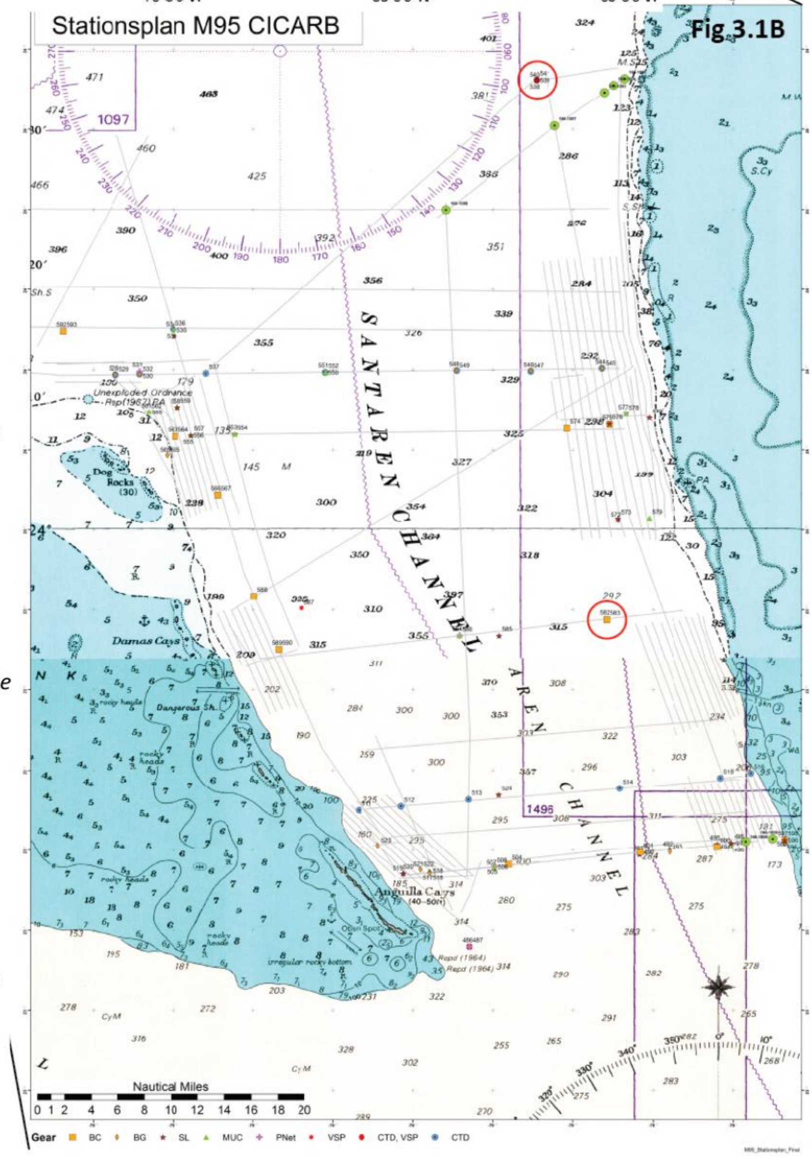

Fig 3.1.1A: A map of the Caribean Sea and the location of the Santaren Channel including the sailed path of the RV Meteor during the M95 Cruise. The study area is indicated in red. Source: M95 Cruise report RV Meteor

***Fig 3.1.1B**: The final station plan of the M95 'CICARB' Cruise. The location of stations from which the samples are obtained are indicated with a red circle. In the north, stations 540 and 541 include the known deep water reef occurrences in the Straits of Floridea which are studied and mapped intensively by Correa et. al., 2012. Hydroacoustic surveys in the south discovered station 583, a series of deep water coral mounds on the distal slope on the GBB. Depth is discplayed in nautic fanthoms*

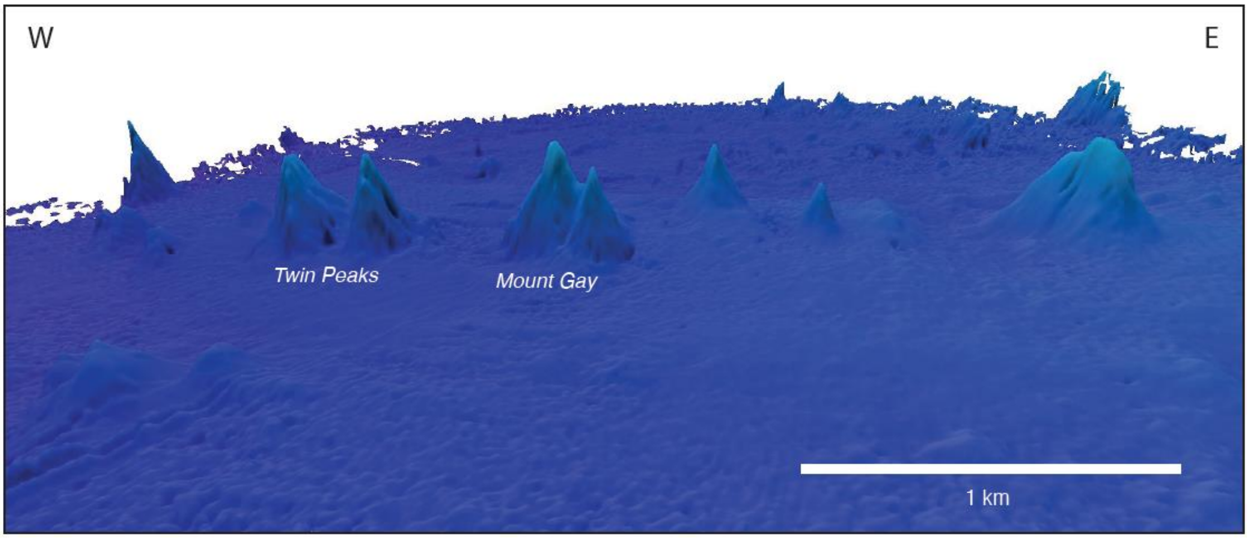

Fig 3.1.2: *Zoomed Multibeam echosounder image of the known cold water reef occurrences on the distal toe-of-slope of the GBB, studied by Correa et al., 2012. Water depth is approximately 590 m and the coral mounds are 50 m high. Image looks to the west into the distal parts of the Santaren Channel. Two CWC mounds were successfully sampled. Data were obtained during the M95 'CICARB' on the research vessel RV Meteor using an Atlas Hydrosweep DS-2 Multibeam echosounder.*

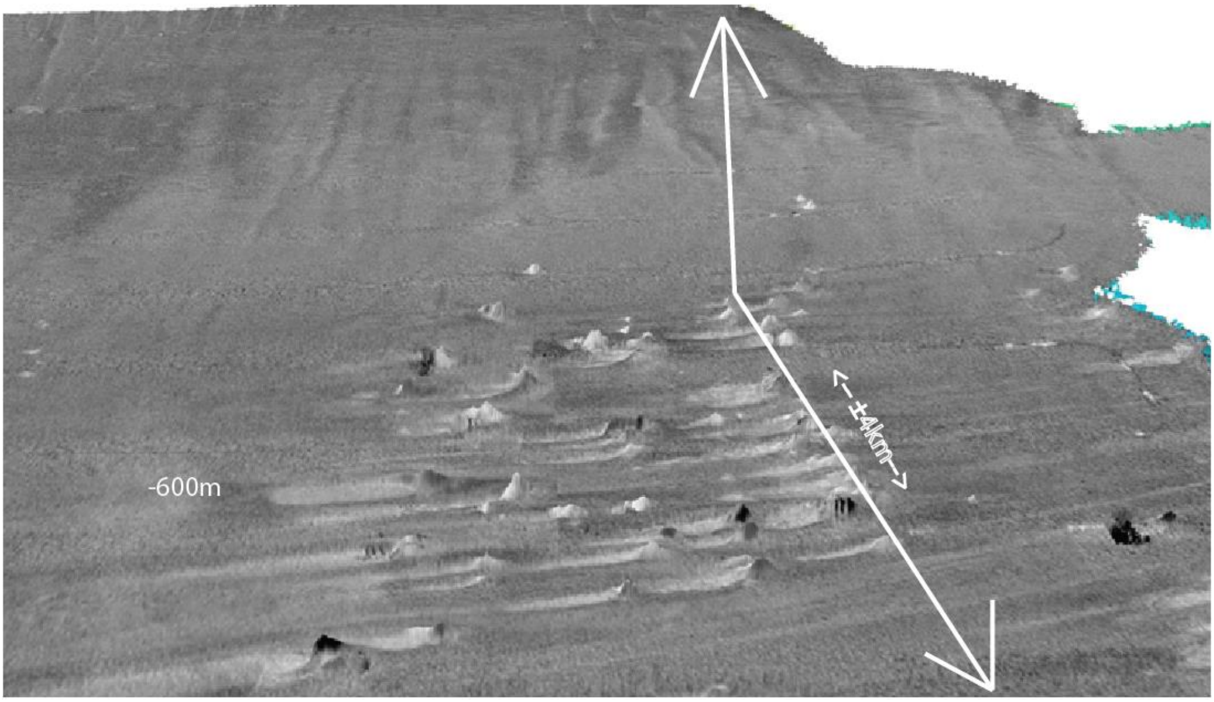

Figure 3.1.3*: A backscatter image of the unknown CWC mounds including Station 583, on the western slope of the GBB, looking to the east. The mounds occur at the toe of slope of the GBB. The water depth range in this image is approximately 600 ± 50 m. At one location, the CWC mounds were successfully sampled. The data were obtained during the M95 'CICARB' Cruise to the Bahama's from Kingston to Point-á-Pítre using the onboard Multibeam ATLAS HydroSweep DS-2 echosounder.*

Figure 3.1.4: *Deep-water coral dominated rubble including Enallopsamnia, Lophelia and sponge fragments. The samples were obtained from Mount Gay and collected with a gravity corer (M95-541-SL)*

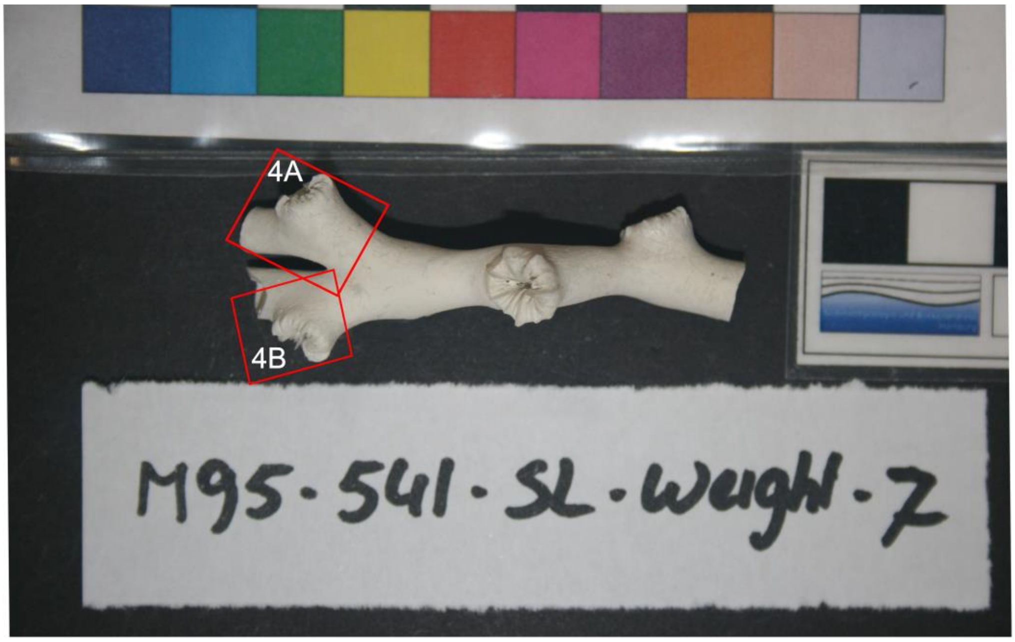

Figure 3.1.5: *Photograph of a Lophelia specimen obtained from Mount Gay (M93-541-SL). Indicated in red sampled polyps 4A and 4B which are used for fluid inclusion analysis*

Station	Date	Time UTC	PositionLat	PositionLon	Depth [m]	Gear
ME095/540-1	10.04.2013	10:06	24° 33,69' N	079° 20,72' W	598,9	Van Veen Grab
ME095/541-1	10.04.2013	10:42	24° 33,69' N	079° 20,72' W	598,2	Gravity corer
ME095/583-1	16.04.2013	21:56	23° 53,26' N	079° 15,47' W	558,6	Box corer

Table 3.1: *A Fraction of the station list of the M95 cruise including the stations from which the samples for this study were obtained.*

Crush	Cold-water coral sample (M95 code name)
1A 1B	M95-541-SL-Weight 4 M95-541-SL-Weight 4
2B	M95-541-SL-CC
3C 3B	M95-541-SL-Weight 6 M95-541-SL-Weight 6
4A 4B	M95-541-SL-Weight-7 M95-541-SL-Weight-7
5A	M95-583-BC-CWC
6A 6B	M95-541-SL-Weight-3-C M95-541-SL-Weight-3-C
7A 7B	M95-541-SL-Weight-3-B M95-541-SL-Weight-3-B
8A 8B	M95-541-SL-Weight-3-A M95-541-SL-Weight-3-A
9A	M95-583-BC-Bulk
10A	M95-540-BG

Table 3.2: *A list of the crushed cold-water coral samples and their code name which relates to the station number (M95-541) and the tool which obtained the corals (SL = Gravity Corer; BC = Box Corer; BG = Grab Sampler)*

For the second part of the study, samples of *Montastrea annularis* from Avilia Beach, Curaçao were used. The samples were collected in October 1990 and July/August 1991 and used for the analysis published in the doctoral thesis of Hemmo Bosscher at the VU University Amsterdam (Bosscher, 1992). Samples of *M. annularis* were taken on the leeward fringing reef of Curaçao, Netherlands Antilles (Figure 3.1.6),. At three locations, coral samples were taken at different depth intervals of 2 m in between 0 to 30 m water depth. The cores were taken along the major vertical growth axis of each coral colony and were derived from a water depth less than 10 m. Subsequently, slabs of 5 mm were cut from the cores for linear extension measurements. However, for this study, only cores 1, 3 and 5 were used. In addition, Bosscher collected samples of entire coral colonies from 20 m water depth. The colonies were also cut to slabs and used for linear extension measurements. Slabs of colonies 2, 4 and 7 were used for this study. Various samples of 0,350 - 0,800g were cut off along the major vertical growth axis of the slabs, representing different ages of the coral sample (Figure 3.1.7). In addition, annual HD and LD bands of the coral skeleton, indicated with X and O respectively were sampled from cores 1, 3, 5 and 6. High Density (HD) and Low Density (LD) bands were clearly visualized by Bosscher (1992) by using computerized tomography. He correlated an anomalously thick white high denisity band to the 1987 ‘bleaching’ event in the Caribean. Therefore, the dark areas of the coral skeleton are interpreted as LD bands.

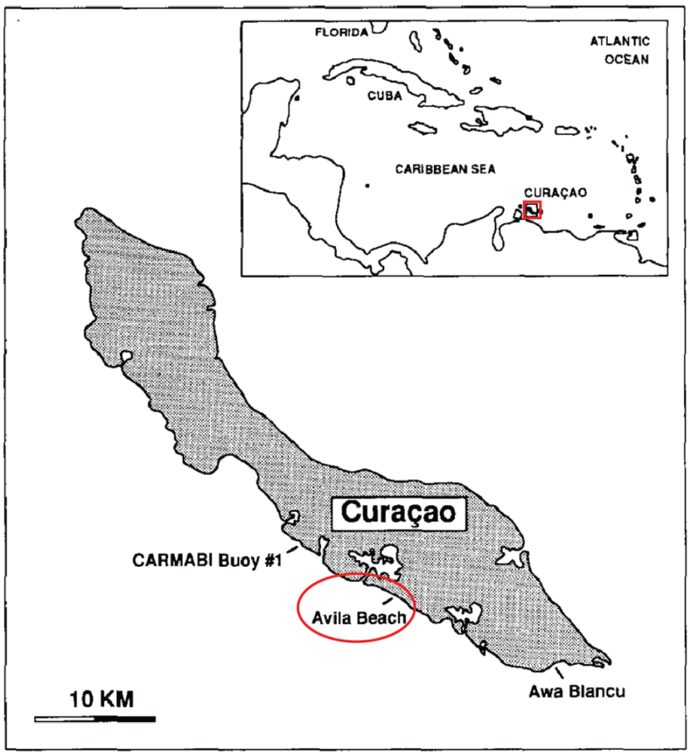

Figure 3.1.6: *Schematic map of Curaçao, Netherlands Antilles and the localities of the samples used in this study (Modified after Bosscher 1992).*

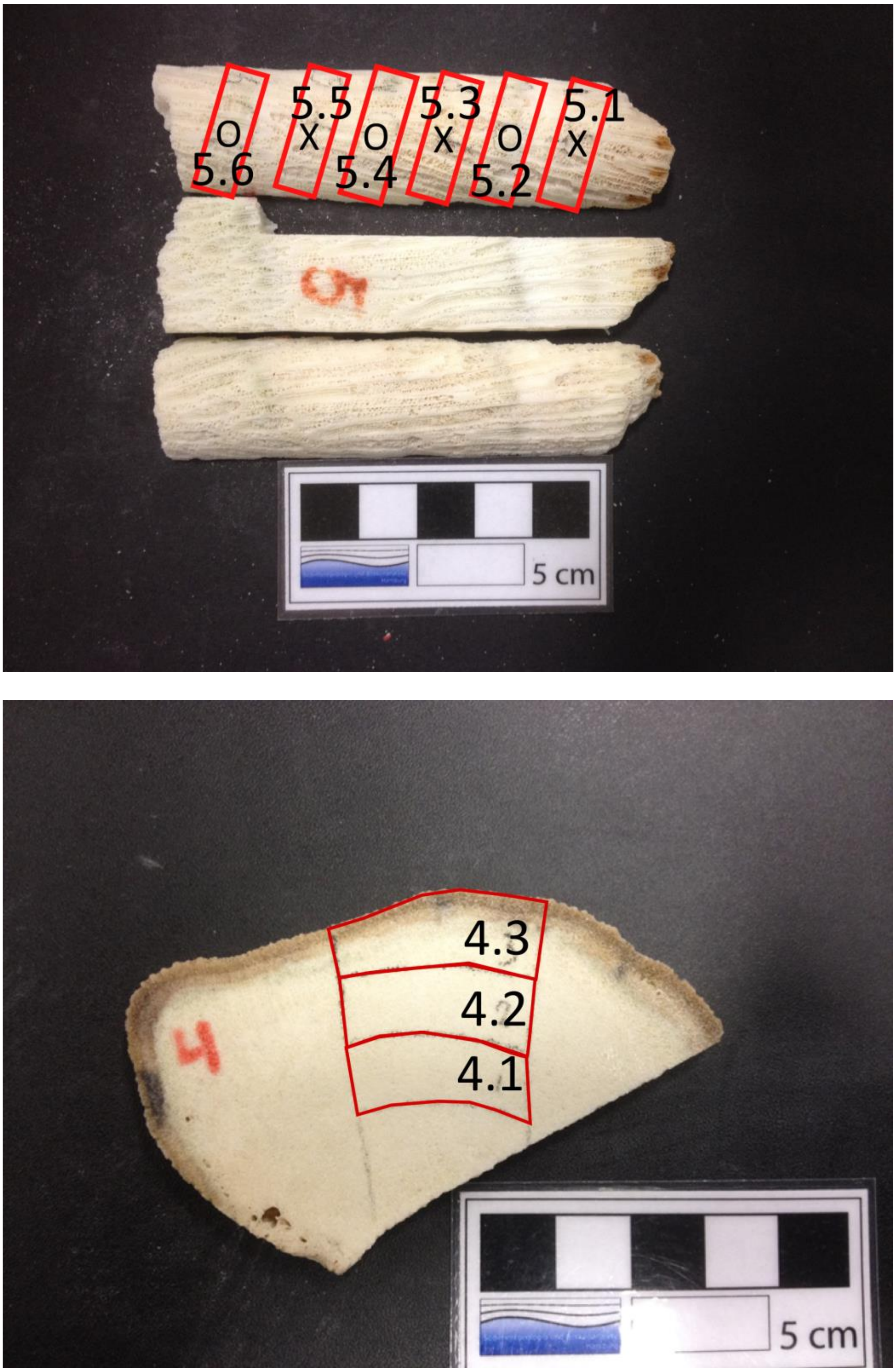

Figure 3.1.7 (A): *Photograph of M. annularis sample 5. Coral cores were samples from top (1), which represents the younger, outer part of the coral, to bottom (5)***,** *which represent the older, inner part of the coral core. High density (white) bands are indicated with an X and Low Density (dark) bands are indicated with an O.* ***(B):*** *Photograph of M. annularis sample 4. Coral colonies were sampled from bottom (1), which represents the older, inner part of the coral colonie, to top (3), which represents the younger, outer part of the coral colonie and contains the coral polyps*

3.2 The `Amsterdam Device´

Subsequently, oxygen and hydrogen isotopic analysis on fluid inclusions in *L. pertusa* and *M. annularis* was done in the Stable Isotope Laboratory at the VU University Amsterdam using the 'Amsterdam Device'. The technique is based on a commercially available continuous-flow pyrolysis furnace, a ThermoFinnigan TC-EA, which is connected to the 'Amsterdam Device' (Vonhof et. al., 2006). It is constructed around a manual crusher, made of a modified 8BG vacuum valve (Fig. 3.2.1A). When turning the valve handle, the hardened steel piston is lowered into the crushing chamber and the samples are crushed into <0.1mm up to >1mm sized fragments. The total volume of the crushing chamber is $\sim 1{,}5 cm^3$, which allows samples of approximately 0,500 to 1 g to be crushed, depending on the type of coral.

The Crusher, which was originally used for speleothem analysis (Vonhof et. al., 2006), was constructed above a small oven included with a 250 W plate heater. Inside the oven (Fig. 3.2.1B), the crusher was connected to the He carrier flow, and via a cold trap to the TC-EA, with 0.75mm i.d. annealed stainless steel capillary and Swagelock connectors (Vonhof et. al., 2006). Two (heat-resistant) Swagelock SS-4BG-VD valves were applied in the oven (valves A and B). For the two valves outside the oven (valves C and D) a Swagelock SS-42-S4 was used (Vonhof et. al., 2006).

In addition, the 'Amsterdam Device' includes a 'Cold trap' (Fig. 3.2.1C), which consists of a coiled 0.75mm i.d. stainless steel capillary (12 coils of 25mm diameter). The trap is positioned outside the oven, therefore it can be plunged in a cold gel of approximately -90 °C. The gel is mix of ethanol and liquid N_2 and it traps the H_2O from the fluid inclusion which is carried in the He flow.

At first, a standard water sample (*DNS-3* standard water) of $0{,}20\, \mu L$ was injected through the septum port repeatedly as the carrier flow was set at 90 mL/min. Subsequently, the sample was crushed and the isotope composition of the fluid inclusion was measured. Finally, another standard water sample was injected. By using a correction for *DNS-3* standard water on both the ^{18}O and the ^{2}H ,the stable isotope values of the Fluid Inclusions were obtained.

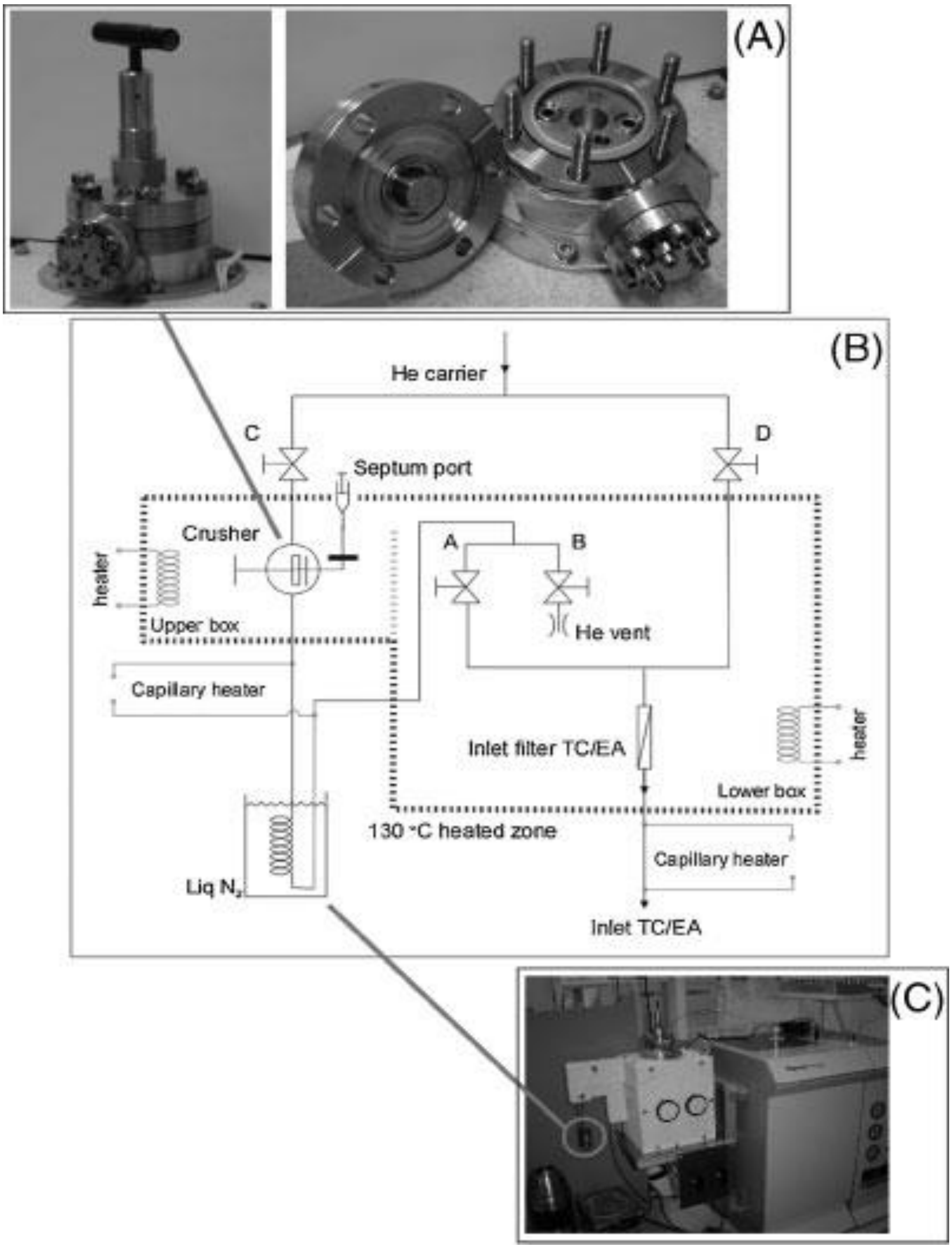

Figure 3.2.1 (A): *Photgraphs (A and C) and schematic drawing (B) of the 'Amsterdam Device', located in the Stable Isotope Laboratory at the VU University Amsterdam. The samples were crushed in the manual crusher (A). Subsequently, the included fluid was trapped with a 'Cold 'Trap' (C) which was plunged in a cold gel of approximately -90˚C prior to is was carried to the TC-EA through the He-flow (after Vonhof H.B. et. al., 2006).*

3.3 The Gasbench II

In addition, stable isotope analysis on the bulk samples of the crushed coral skeletons was done to obtain $\delta^{18}O_{ar}$. This was done on the Gasbench II and Finnigan DeltaPlus IRMS, located in the Isotope Laboratory at the VU University Amsterdam. The GasBench II is a universal online interface, which allows automated isotope ratio determination of a small gas sample. The gas (CO_2) was extracted from a solid phase (corals). For carbonates, CO_2 was formed by adding 100% H_3PO_4 to the coral samples:

$2H_3PO_4 + 3CaCO_3 = 3CO_2 + 3H_2O + Ca_3(PO_4)$

Subsequently, the CO_2, which carries the carbon and oxygen isotopic signature of the coral sample, was analyzed by Isotopic Ratio Mass Spectrometry using the Finnigan Delta plus.

In addition, the known isotope ratio of a reference gas (CO_2) was analyzed during the measurement, to determine the $\delta^{18}O$. And $\delta^{13}C$ values of the bulk coral sample. Moreover, sample size corrections were done during every run using a carbonate standard (VICS) and IAEA-CO1 was measured as a control standard. The standard deviation of the measurements for $\delta^{18}O$ and $\delta^{13}C$ was < 0.2 ‰ and < 0.1‰ respectively.

3.4 Thermometry

For *Lophelia pertusa* from the Santaren Channel, the formula of Smith, Schwarz et al. (2000) was used to determine the $\delta^{18}O$ equilibrium value for aragonite:

$T\ (^{0}\mathrm{C}) = 19{,}8 - 4(\delta^{18}O_{ar} - \delta_w)$,

CTD measurements estimated the in situ sea water temperature at the depth from which the coral specimens were derived to be 9,0°C and the salinity to be 35 PSU
Lynch-Stieglitz et. al., (1999) stated that salinity and δ_w are often well correlated in the oceans and since the relation can be described by the formula:

$\delta^{18}O_{seawater} = -14{,}34 + 0{,}419S$

the $\delta^{18}O_{seawater}$ (δ_w) was calculated and is 0,325‰ VSMOW. Subsequently, $\delta^{18}O$ equilibrium value for aragonite was calculated and is 3,025‰

For *Montastrea annularis* from Curaçao, the formula of Leder (1996) was used to determine the $\delta^{18}O$ equilibrium value for aragonite:

$T\ (^{0}C) = 5.33 - 4.519(\delta^{18}O_{ar} - \delta_{w})$,

The mean annual ocean water temperature at Curaçao is 26,5°C *(http://www.ospo.noaa.gov).* The δ_{w} was determined to be 1,34‰ (Schmidt, 1999), therefore equilibrium value for aragonite is $-3{,}34\permil$ (VSMOW)

4. Results

In this section, the results of this study are presented. Table 4.1 shows all the data of the oxygen and hydrogen analysis on the fluid inclusions and oxygen and carbon analysis of the carbonate skeleton of *L. pertusa.* In addition, table 4.2 contains all the data of the fluid inclusions and the carbonate skeleton of *M. annularis.* In the first part of this section, the results of the fluid inclusions and carbonate skeleton in *Lophelia pertusa* will be presented, followed by the results of fluid inclusions and carbonate skeleton measurements of *M. annularis.*

4.1 *Lophelia pertusa* Fluid Inclusions

The isotopic compositions of the fluid inclusions in the cold-water coral *Lophelia pertusa,* relatively to SMOW are shown in Figure 4.1.1. The δ^2H ranges from -25.60 to +95.68 (‰ VSMOW) and the $\delta^{18}O$ ranges from -5.94 to +5.82 (‰ VSMOW). SMOW (0;0) is indicated in red.

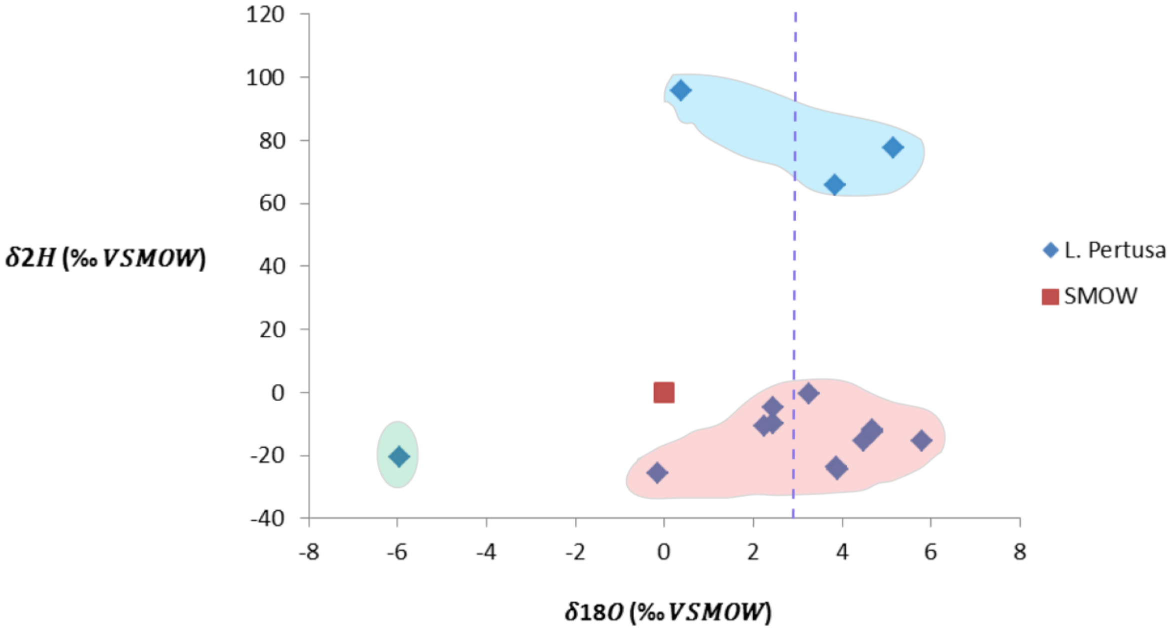

Figure 4.1.1: *A Plot of the stable isotope composition of fluid inclusions in Lophelia pertusa from the Bahamas relative to SMOW including 3 clusters of datapoints. The blue dotted line represents the $\delta^{18}O$ equilibrium value for aragonite which is +3,03‰ at the Santaren Channel (based on Smith, Schwarz et al., 2000).*

The data consist of roughly three clusters of data points. Cluster 1, indicated in red comprises the majority of the data points, they show an enrichment of $\delta^{18}O$ and a minor depletion of $\delta^{2}H$ relative to SMOW and the isotope equilibruim. The second cluster, indicated in blue, consists of three data points which show an major enrichment in $\delta^{2}H$ and an enrichment of $\delta^{18}O$, comparable to Cluster 1. In addition, there is one data point, indicated in green, which shows a major depletion of $\delta^{18}O$ and a minor depletion of $\delta^{2}H$.

4.2 *Montastrea annularis* Fluid Inclusions

The isotopic compositions of the fluid inclusions in the tropical coral *Montastrea annularis,* relatively to SMOW are shown in Figure 4.2.1. The $\delta^{2}H$ ranges from -23,37 to +87,74 ‰ vs VSMOW and the $\delta^{18}O$ ranges from -0,83 to 7,68 ‰ vs VSMOW. In addition, the mean isotopic composition is 2,04‰ for $\delta^{18}O$ and 48,27 ‰ vs VSMOW for $\delta^{2}H$.

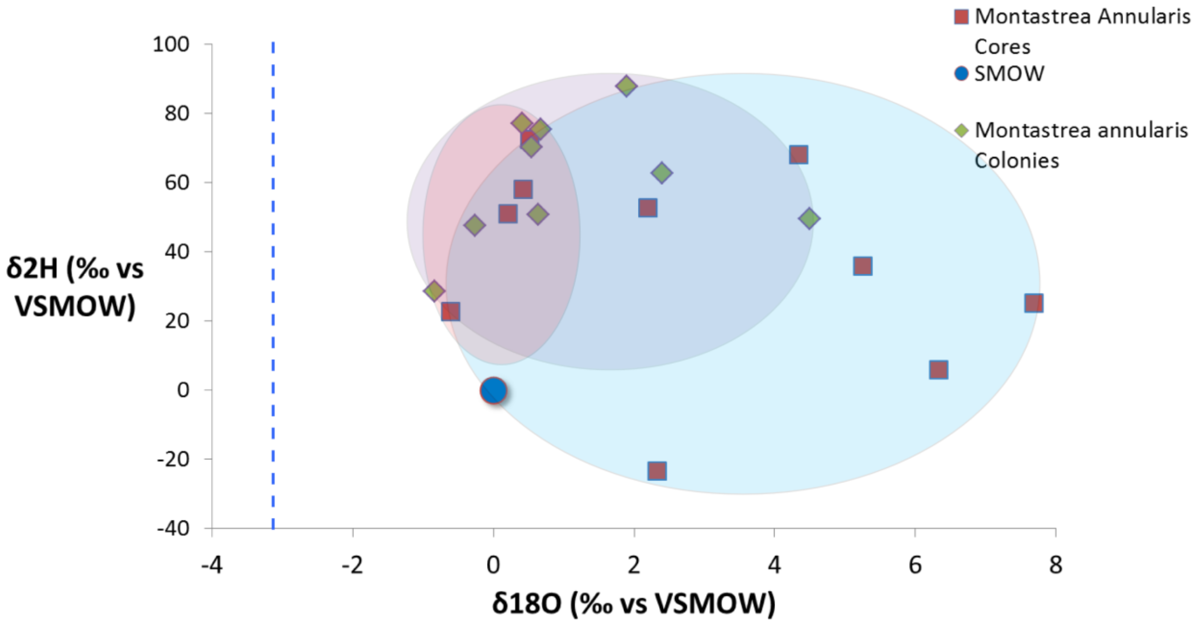

Figure 4.2.1: *The isotopic composition of fluid inclusions in the tropical coral Montastrea annularis relatively to SMOW including the range of the data points (blue) and a possible cluster of data points (red). The blue dotted line represents the equilibrium value for aragonite at the mean temperature of the seawater at Curaçao based on Leder et. al., (1996).*

The stable isotope compositions of the fluid inclusion plot in the area of the blue circle in Figure 4.2.1. The spread of the data is relatively large for both $\delta^{2}H$ and $\delta^{18}O$. In general, the isotope composition of fluid inclusions in *M. annularis* show an enrichment of $\delta^{2}H$ relatively to SMOW.

However, sample 3.4 (Table 4.2) seems to be the only exception to this trend shows a major depletion in $\delta^{2}H$. Furthermore, the majority of the data shows an enrichment in $\delta^{18}O$ relative to SMOW whereas sample 6.1, 7,2 and 7,3 are slightly depleted in $\delta^{18}O$.

However, the majority of the data suggests a cluster of the datapoints which is indicated in red in Figure 4.2.1. This cluster appears to be clustered at approximately 0 to 0.5 (‰ VSMOW) for $\delta^{18}O$ and 50 – 60 (‰ VSMOW) for $\delta^{2}H$.

4.3 Stable Isotopes of skeletal carbonate of *L. pertusa*

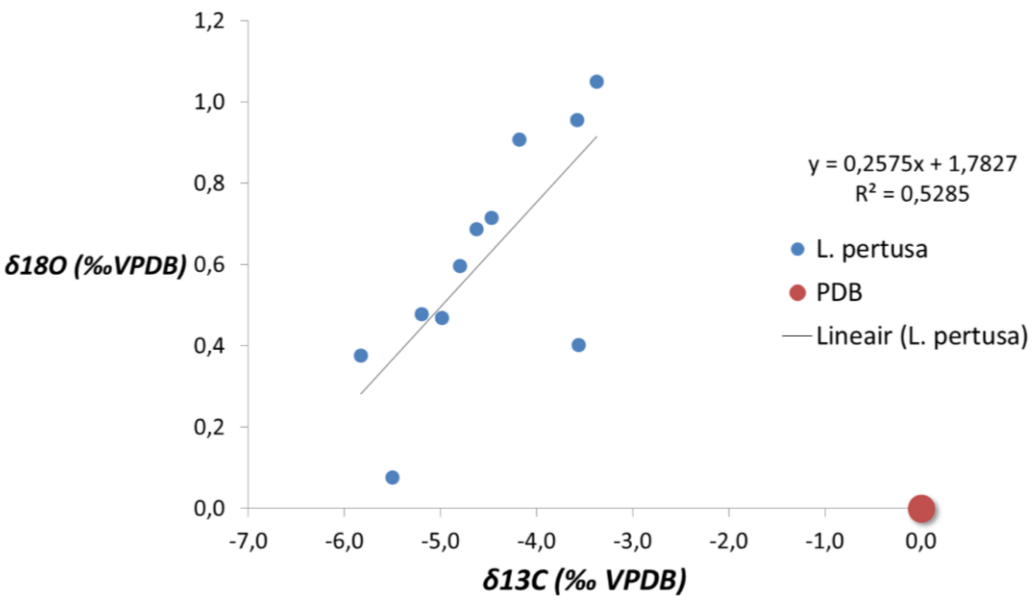

Figure 4.3.1: *A plot of the oxygen and carbon stable isotopes of the carbonate skeleton of Lophelia pertusa from the Bahamas versus PDB, indicated in red. The values plot significantly lower than the* $\delta^{18}O$ *equilibrium value for aragonite which is +3,03‰, (based on Smith, Schwarz et al., 2000) which extends this graph.*

The isotopic compositions of the carbonate skeleton of the cold water coral *Lophelia pertusa* from the Bahamas, relatively to PDB are shown in Figure 4.3.1. The $\delta^{13}C$ ranges from -5,830 to -3,373 (‰ VPDB) and the $\delta^{18}O$ ranges from 0,077 to 1,049 (‰ VPDB). The data points show a linear trend described by the formula

$$y = 0{,}2575x + 1{,}7827$$

In which $x = \delta^{13}C$ and $y = \delta^{18}O$ of the carbonate skeleton and $R^2 = 0.5285$

4.4 Stable Isotopes of skeletal carbonate of *M. annularis*

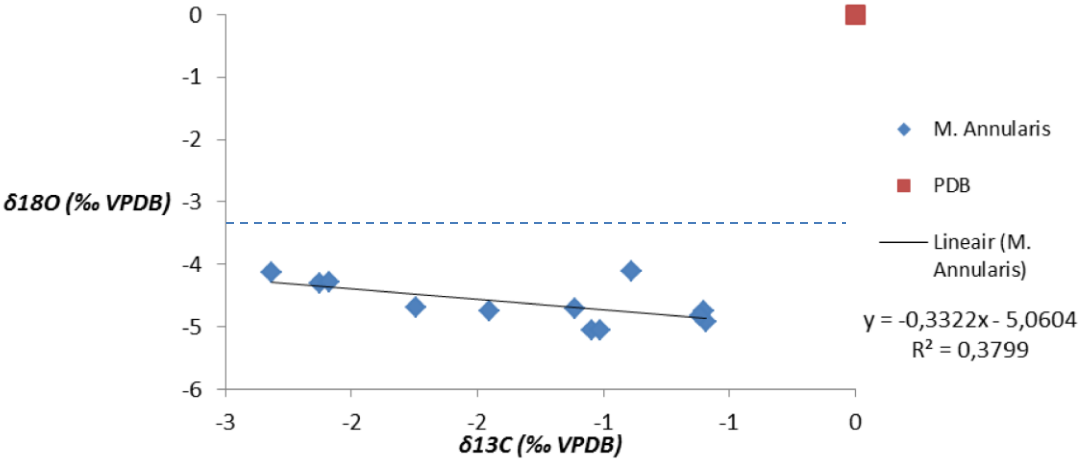

Figure 4.4.1: *A plot of the oxygen and carbon stable isotopes of the carbonate skeleton of Montastrea annularis versus PDB, indicated in red. The blue dotted line represents the equilibrium value for aragonite at the mean temperature of the seawater at Curaçao based on Leder et. al., (1996).*

The isotopic compositions of the carbonate skeleton of the tropical coral *Montastrea annularis,* relatively to PDB are shown in Figure 4.4.1. The $\delta^{13}C$ ranges from -2.318 to -0.595 ‰ (VPDB) and the $\delta^{18}O$ ranges from –5.599 to -4.103 ‰. The data points show a linear trend described by the formula

$$y = -0.3322x - 5.06047$$

In which $x = \delta^{13}C$ and $y = \delta^{18}O$ of the carbonate skeleton and $R^2 = 0.3799$

Species	**Origin**	**Crush**	**Comments**	**Area H2**	**Area CO**	**δ18O (‰ vs VSMOW)**	**d2H (‰ vs VSMOW)**	**δ13C (‰ vs VPDB)**	**δ18O (‰ vs VPDB)**
Lophelia Pertusa	Bahamas Station 541	1A		47,900	137,300	4	-15	-3,561	0,403
Lophelia Pertusa	Bahamas Station 541	1B		75,700	211,000	5	-12	-5,192	0,477
Lophelia Pertusa	Bahamas Station 541	2B		144,700	398,500	5	-13	-	-
Lophelia Pertusa	Bahamas Station 541	3B		249,500	698,500	4	-24	-	-
Lophelia Pertusa	Bahamas Station 541	3C		72,900	216,200	6	-15	-4,468	0,715
Lophelia Pertusa	Bahamas Station 541	4A		50,100	145,400	2	-10	-3,577	0,955
Lophelia Pertusa	Bahamas Station 541	4B		61,400	178,700	2	-11	-4,179	0,906
Lophelia Pertusa	Bahamas Station 583	5A		61,700	178,700	2	-5	-3,373	1,049
Lophelia Pertusa	Bahamas Station 541	6B		18,382	54,864	4	66	-4,984	0,469
Lophelia Pertusa	Bahamas Station 541	7A		55,053	165,693	4	-25	-4,627	0,687
Lophelia Pertusa	Bahamas Station 541	7B		45,793	128,452	3	0	-4,795	0,597
Lophelia Pertusa	Bahamas Station 541	8A		104,512	278,956	0	-26	-5,830	0,376
Lophelia Pertusa	Bahamas Station 541	8B		162,900	403,513	-6	-21	-5,499	0,077
Lophelia Pertusa	Bahamas Station 583	9A		36,992	116,224	5	78	-	-
Lophelia Pertusa	Bahamas Station 540	10A		17,525	57,285	0	96	-	-

Table 4.1: *Summary of all the Lophelia pertusa measurements including the origin of the samples, station number, crush number, area H2 and CO, the isotope composition of the fluid inclusions and the isotope composition of the carbonate skeleton*

Species	Origin	Crush	Comments	Area H2	Area CO	δ18O (‰ vs VSMOW)	d2H (‰ vs VSMOW)	δ13C (‰ vs VPDB)	δ18O (‰ vs VPDB)
Montastrea Annularis	Curaçao Avilla Beach	1.1	Core	33,842	99,232	0	58	-	-
Montastrea Annularis	Curaçao Avilla Beach	1.2	Core	41,580	120,833	8	25	-	-
Montastrea Annularis	Curaçao Avilla Beach	1.3	Core	25,874	79,168	4	68	-	-
Montastrea Annularis	Curaçao Avilla Beach	2.1	Colony	29,240	95,483	0	77	-1,115	-4,701
Montastrea Annularis	Curaçao Avilla Beach	2.2	Colony	33,955	111,876	4	50	-1,049	-5,053
Montastrea Annularis	Curaçao Avilla Beach	2.3	Colony	32,212	103,912	1	51	-0,590	-5,599
Montastrea Annularis	Curaçao Avilla Beach	3.1	Core	82,381	230,664	5	36	-2,318	-4,129
Montastrea Annularis	Curaçao Avilla Beach	3.2	Core	113,894	312,951	6	6	-2,088	-4,284
Montastrea Annularis	Curaçao Avilla Beach	3.3	Core	40,148	121,109	0	51	-2,127	-4,302
Montastrea Annularis	Curaçao Avilla Beach	3.4	Core	116,905	324,863	2	-23	-	-
Montastrea Annularis	Curaçao Avilla Beach	4.1	Colony	32,669	109,870	2	88	-0,595	-4,916
Montastrea Annularis	Curaçao Avilla Beach	4.2	Colony	36,635	118,576	2	63	-1,452	-4,745
Montastrea Annularis	Curaçao Avilla Beach	4.3	Colony	31,393	101,506	1	70	-0,600	-4,745
Montastrea Annularis	Curaçao Avilla Beach	5.1	Core	42,316	128,846	2	53	-	-
Montastrea Annularis	Curaçao Avilla Beach	5.2	Core	21,916	71,120	1	72	-	-
Montastrea Annularis	Curaçao Avilla Beach	6.1	Core	65,694	192,466	-1	23	-0,889	-4,103
Montastrea Annularis	Curaçao Avilla Beach	7.1	Colony	30,009	97,507	1	75	-1,014	-5,052
Montastrea Annularis	Curaçao Avilla Beach	7.2	Colony	31,117	100,511	0	48	-1,746	-4,686
Montastrea Annularis	Curaçao Avilla Beach	7.3	Colony	49,598	148,310	-1	29	-0,618	-4,824

***Table 4.2**: Summary of all the Montastrea annularis measurements including the origin of the samples, station number, crush number, area H2 and CO, the isotope composition of the fluid inclusions and the isotope composition of the carbonate skeleton*

5. Discussion

5.1 Analysis of *Lophelia pertusa* Fluid Inclusions; Comparison with Data from Feenstra (2013)

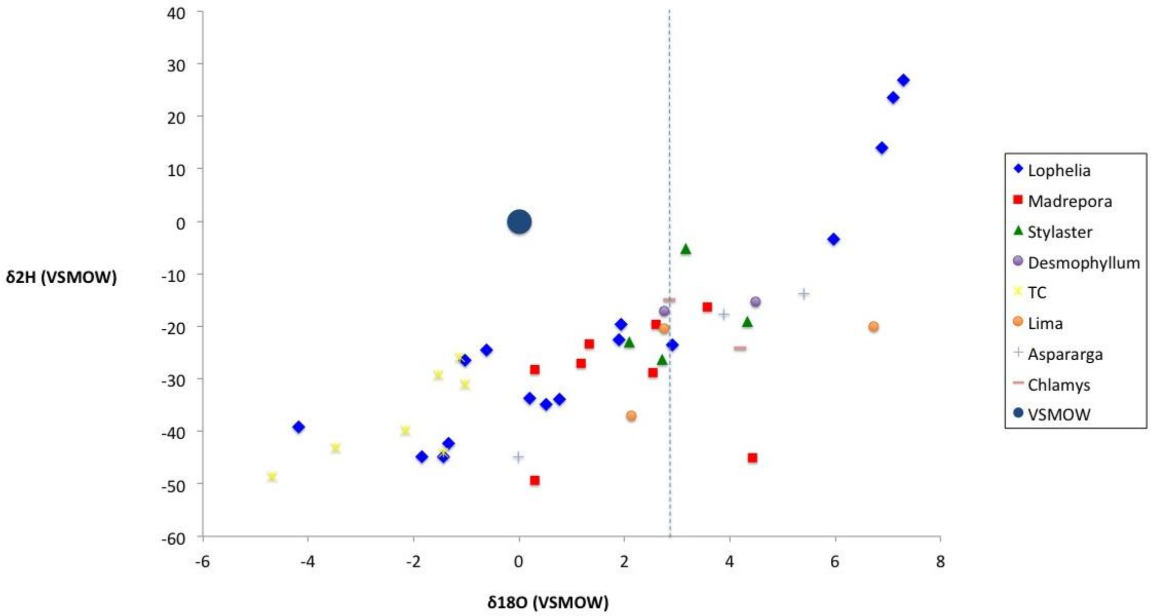

Fig 5.1.1: *Unpublished data from Feenstra (2013) including the stable Isotope values of fluid inclusions in cold water corals and bivalves from the Rockall Trough margin, on the western flank of the Irish continental slope. The data, and Lophelia pertusa (blue) in particular, show a large distribution regarding to oxygen isotope values. Oxygen Isotope values vary significantly from -4,188 to 7,294‰ VSMOW. The blue dotted line represents the equilibrium value for aragonite at the mean temperature of the Rockall Trough based on Smith, Schwarz et al. (2000) (after Feenstra, 2013).*

First analyses from fluid inclusions in *L. pertusa* by Feenstra (2013) show a significantly varying oxygen and hydrogen isotope composition (Figure 5.1.1). However, the variation in stable isotope chemistry show a linear trend. An important observation is the fact that the isotope composition of fluid inclusions in *Lophelia* is both enriched and depleted in comparison to the oxygen equilibrium value for aragonite based on Smith (2000).

Based on the linear trend for *Lophelia* of Figure 5.1.1, several measurements of this study are assumed to be invalid. The dataset of this study consists of three clusters of which cluster two and three, including sample 8B; 6B; 9A and 10A (Figure 5.1.2) are assumed to be invalid due to analytical problems of the 'Amsterdam Device' or quality of the sample and are therefore not used for further calculations. This section describes and discusses why these are assumed to be invalid.

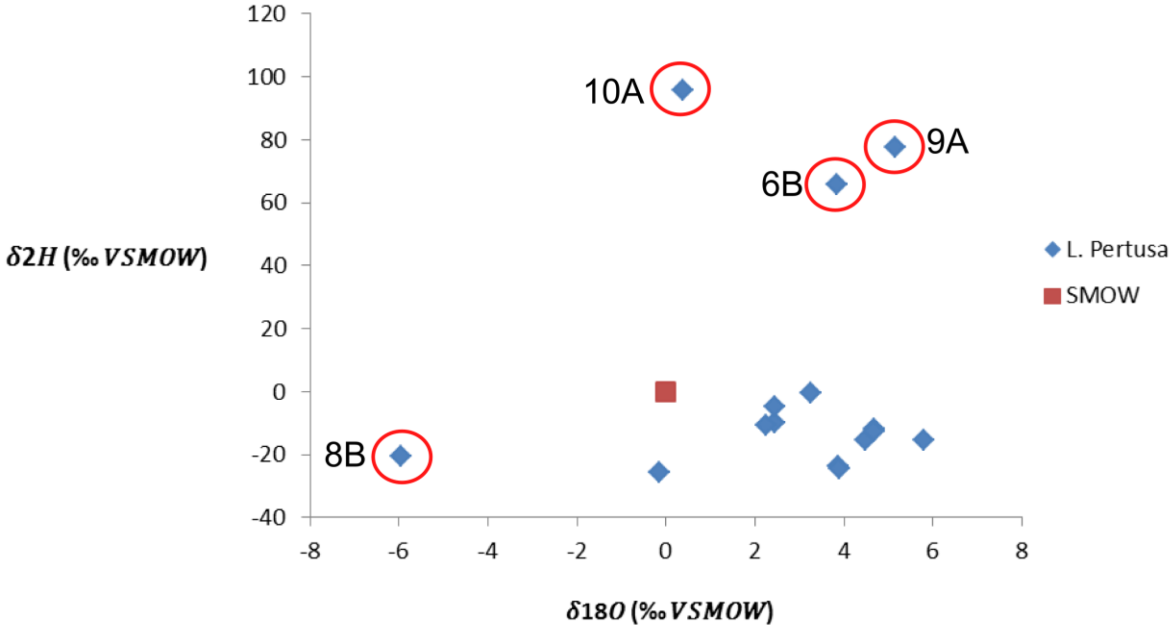

Figure 5.1.2: *A plot of the stable isotope composition of fluid Inclusions in Lophelia pertusa from the Bahamas. Indicated in red are data point which are considered to be invalid due to analytical problems of the 'Amsterdam Device' or quality of the sample.*

Point 8B is equivalent to the point indicated with the red circle in Figure 5.1.3. This figure shows a plot of the area H_2 versus the area *CO* of fluid inclusions in *L. pertusa* from the Bahamas. The area (Volt × seconds) is a measure of the 'Amsterdam Device' of the amount of H_2 or *CO* in fluid inclusions of the crushed samples. The data points suggest a positive linear trend described by the formula

$$y = 2.7493x$$

in which $y =$ the area CO and $x =$ area H_2 of the fluid inclusions and $R^2 = 0.9917$. However, crush 8B does not correspond with the linear trendline. This feature is interpreted as that during the crush of this sample, a significant part of the CO in the fluid inclusion leaked away or retained during transportation to the TC-EA. This possibly caused a relative depletion of the amount of CO relative to the amount of H_2 and therefore the mass spectrometer measured a depletion of $\delta^{18}O$. Therefore, point 8B is assumed to be invalid and is not used for further calculations.

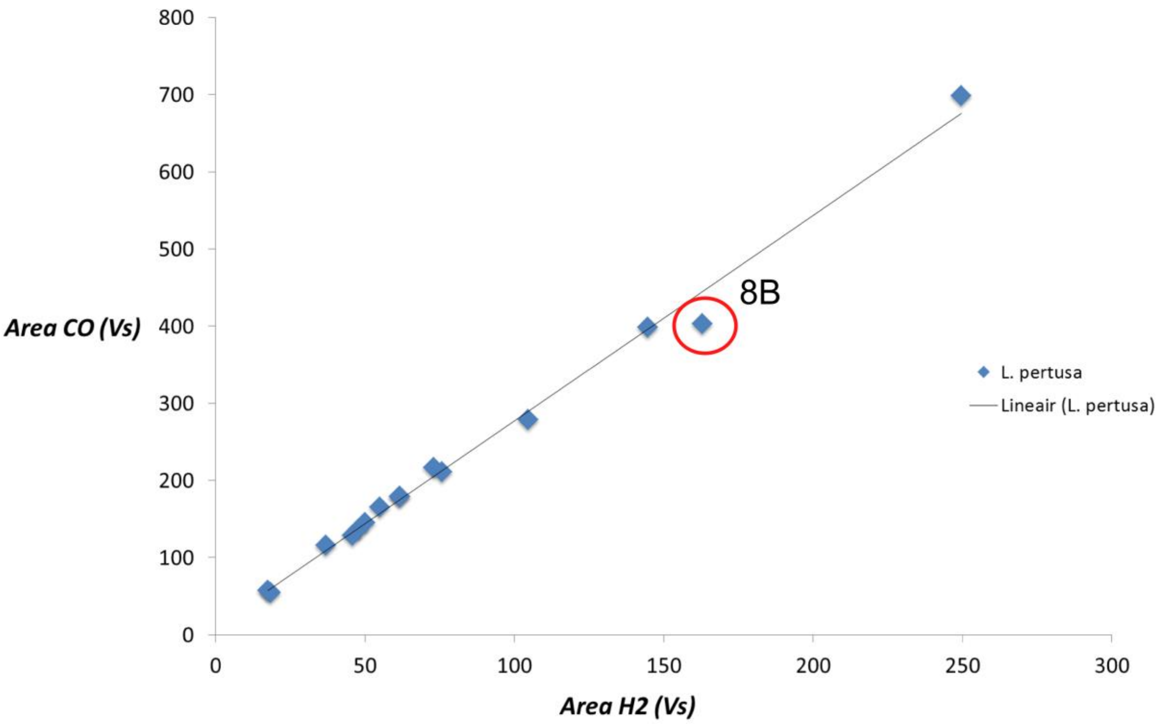

Figure 5.1.3: *A plot of the area H_2 versus the area CO (Volt × seconds) of fluid inclusions in Lophelia Pertusa from the Bahamas. Sample 8A with the red circle is considered to be invalid due to analytical problems of the 'Amsterdam Device'.*

However, there are three more data points (6B, 9A and 10A), which are considered to be incorrect due to the fact that they released a low amount of H_2. Figure 5.1.4 shows a plot of the Area H_2 versus the δ^2H of fluid inclusions in *L. pertusa* from the Bahamas The data points suggest a negative logarithmic trend described by the formula:

$$y = -42\ln(x) + 178.14$$

In which $y =$ the δ^2H and $x =$ area H_2 of the fluid inclusions and $R^2 = 0.5873$. The trend suggests that the 'Amsterdam Device' is sensitive for low amounts of H_2, which will ultimately cause the δ^2H value in fluid inclusions to be significantly high when low amounts of H_2 are released.

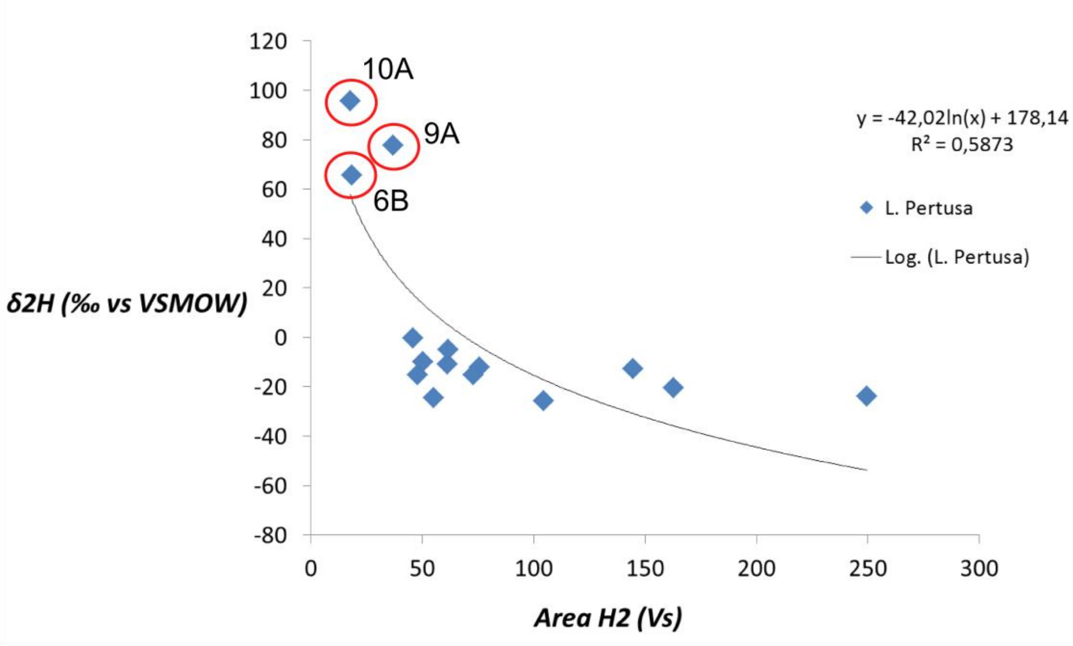

Figure 5.1.4: *A plot of the area* H_2 *versus the* $\delta^2 H$ *of fluid inclusions in Lophelia pertusa from the Bahamas. Samples 6B, 9A and 10A, encircled in red, are considered to be invalid due to analytical problems of the 'Amsterdam Device'.*

Figure 5.1.5 shows the stable isotopes of fluid inclusions in cold water corals from both the Rockall Through margin (*Lophelia*) and the Bahamas (*Lophelia* Keijzer). Lines y1 and y2 represent the linear trendlines for *Lophelia* (Feenstra, 2013) and *Lophelia* including data points of this study, respectively. The linear trendline y1 ($R^2 = 0.8578$) is characterized by the formula $y = 6.1212x - 30.147$ and the linear trendline y2 ($R^2 = 0.7645$) is characterized by the formula $y = 6.6265x - 35.214$.

There is a difference of $6.6265 - 6.1212 = 0.453$ (7,63%) between the slopes of the trendlines. However, this deviation is less than 10%. These observations suggest that the stable isotope values of fluid inclusion from the Bahamas coincide with the stable isotope values of fluid inclusion from the Rockall Trough.

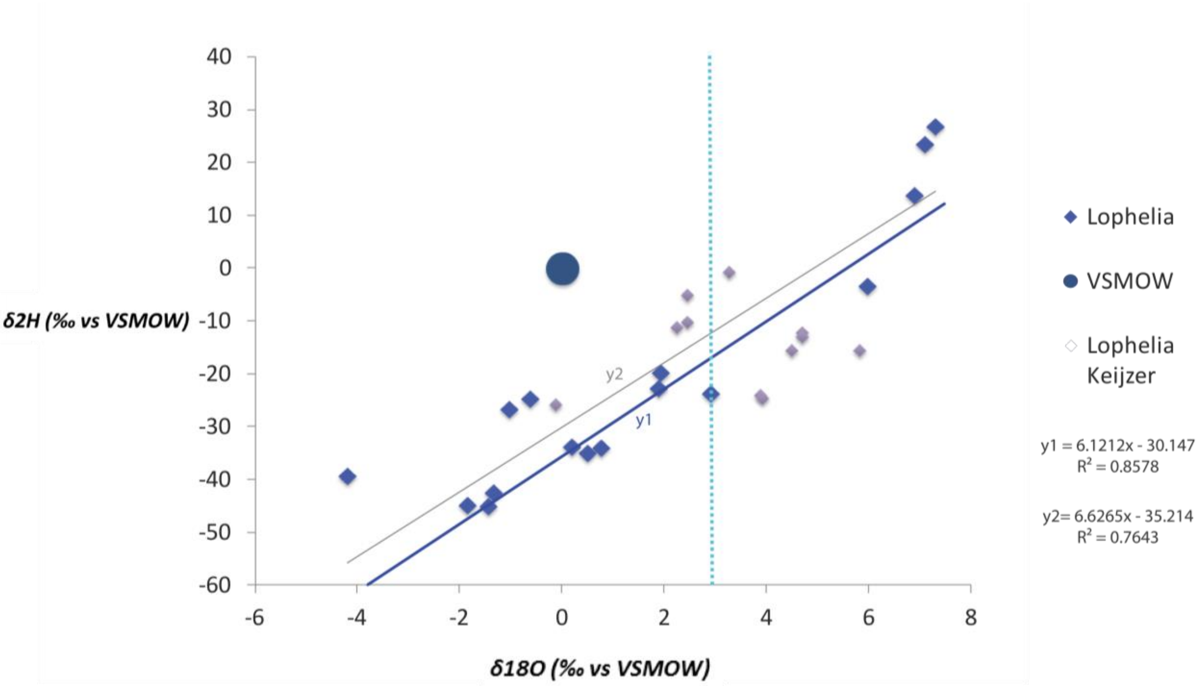

Figure 5.1.5 *Stable isotope composition of fluid inclusions in cold water corals (L. pertusa) from the Rockall Trough margin (Feenstra, 2013) and from the Bahamas (Keijzer, 2014). The data from two independent studies seem to coincide and trend lines of both datasets are very much alike. The assumed incorrect measurements of this study are not displayed in this diagram. The blue dotted line represents the equilibrium value for aragonite at the mean temperature of the Santaren Channel based on Smith, Schwarz et al. (2000).*

Like the Feenstra (2013), the oxygen isotope value of fluid inclusions from *L. Pertusa* from the Bahamas is both enriched and depleted with respect to the oxygen equilibrium value for aragonite based on Smith (2000). Since the variations in isotope chemistry of this dataset also show a linear trend, it is also suggested that this is due to non-equilibrium isotope fractionation effects. Like Feenstra (2013), this study also shows a trend which is characterized by a simultaneous depletion of δ^2H and $\delta^{18}O$, similar to kinetic isotope fractionation effects. However, the fact that the fluid values of *Lophelia* from the Bahamas are also enriched with respect to equilibrium, complicates this interpretation.

Feenstra (2013) suggests Rayleigh Fractionation should be considered as possible mechanism for the isotope variations in fluid inclusions. Figure 5.1.6 shows that there is no direct correlation between the fluid and the carbonate skeleton of *Lophelia* from the Bahamas, suggesting the chemical system to be open. Therefore, Rayleigh Fractionation should also be considered in this study as a mechanism for the isotope variations in fluid inclusions since Rayleigh fractionation applies in strict sense to chemically open systems. In addition, the linear trend of the fluid data aligns with the slope of the Global Meteoric Water Line (GMWL) which is regulated by Rayleigh Fractionation processes (Gagnon, 2007)

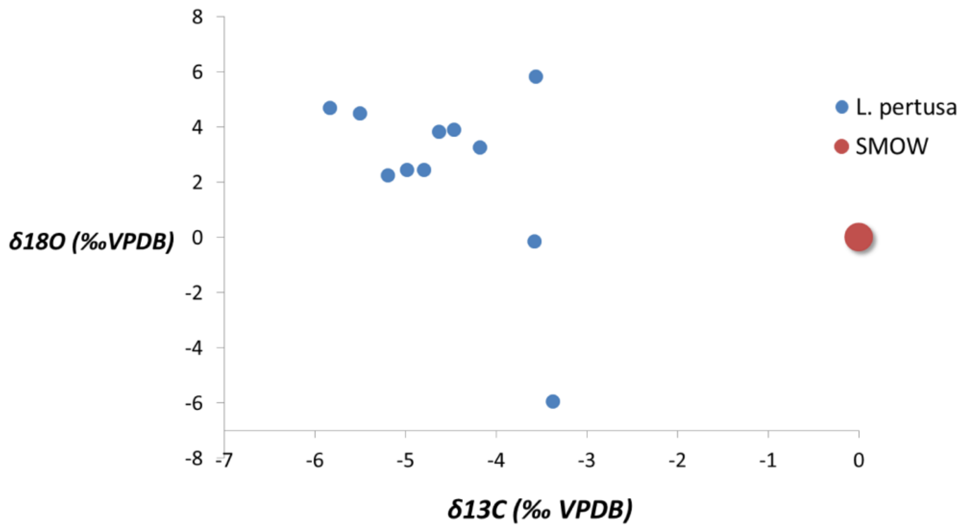

Figure 5.1.6: *A plot of the area* $\delta^{18}O$ *of the fluid inclusions versus the* $\delta^{13}C$ *of the carbonate skeleton of Lophelia pertusa from the Bahamas. No direct correlation can be observed from this data suggesting the chemical system to be open.*

5.2 Analysis of *Montastrea annularis* Fluid Inclusions

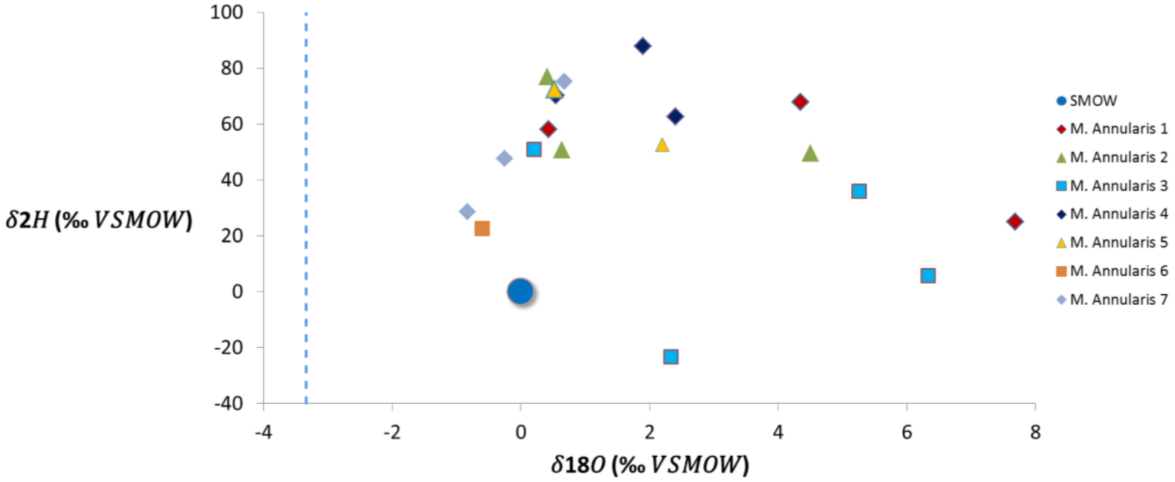

Figure 5.2.1: *Stable isotopes of fluid inclusions in M. annularis including the stable isotope composition of each individual coral specimen indicating significant variations in both δ^2H and $\delta^{18}O$ per M. annularis sample. The blue dotted line represents the equilibrium value for aragonite at the mean temperature of the seawater at Curaçao based on Leder et. al., (1996).*

In this study, seven tropical coral specimens (Figure 3.1.5) of *M. annularis* were crushed. Figure 5.2.1 shows a plot of the stable isotopes of fluid inclusions in *M. annularis* of each individual coral specimen. The isotope compositions of fluid inclusions show significant variations in both δ^2H and $\delta^{18}O$. The $\delta^{18}O$ in particular varies from -0,83 to +7,68‰ (VSMOW). The values of samples 4, 5 and 7 plot relatively close to each other. The values of sample 2 also plot relatively close to each other. However, the isotopic composition in each individual sample varies significantly.

During crushing of the coral specimens, a distinction was also made between *M. annularis* cores and colonies (Figure 3.1.5). Figure 5.2.2 shows the fluid inclusion data of *M. annularis*, including the distinction between colonies and cores. Cores, indicated as red squares, are covered by the blue ellipsoid and colonies, indicated as green diamonds are covered by the purple (smaller) ellipsoid. The *M. annularis* colonies show significant less variation in both δ^2H and $\delta^{18}O$. This observation coincides with the observation that the isotope composition of sample 2, 4 and 7, which represent coral colonies, plot relatively close together. In addition, when analysing the colonies in detail, some other striking features can be observed.

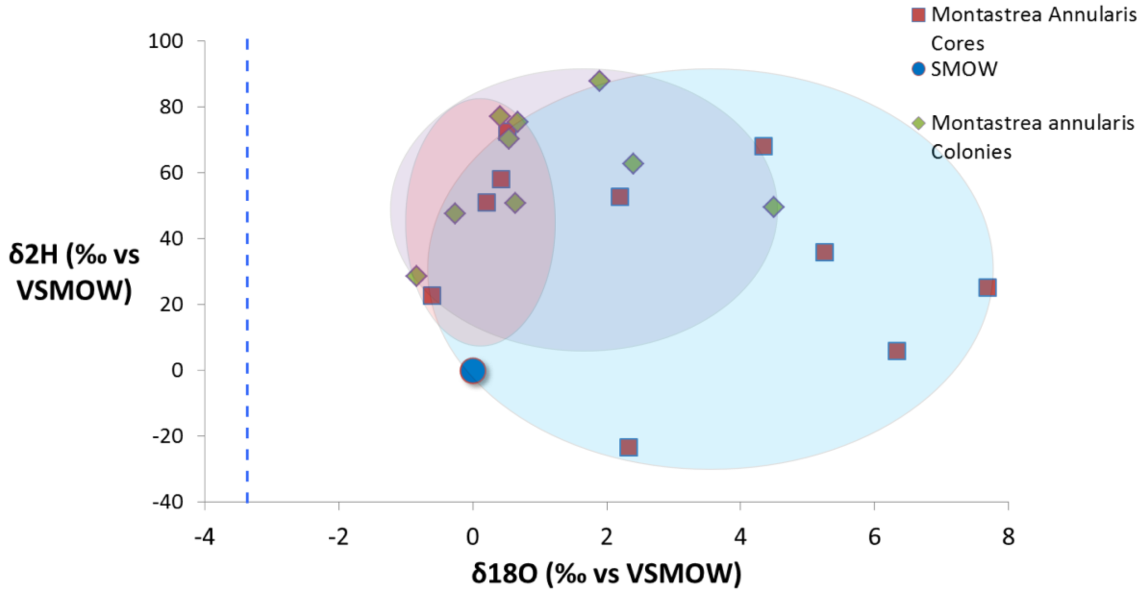

Figure 5.2.2 *Stable isotope composition of fluid inclusions in M. annularis cores, indicated in blue, and plates, indicated in purple. In addition, the red circle indicates a cluster of 53% of the data points. The blue dotted line represents the assumed equilibrium value for aragonite at the mean temperature of the seawater at Curaçao based on Leder et. al., (1996).*

Figure 5.2.3 shows a plot of the stable isotopes of fluid inclusions in *M. annularis* colonies at various depths in these colonies. The isotope composition of the fluid inclusions of the bottom of the colonies show significant higher δ^2H values and slightly higher $\delta^{18}O$ with respect to the top measurements, suggesting a fractionation process in *M. annularis* which causes changes in the composition of the fluid inclusion with increasing depth and time of deposition. The isotope composition of the included water at the top of the plates is close to that of SMOW, whereas the isotope composition of the deeper included water is more variable and less close to sea water composition.

It is difficult to explain an increase in both δ^2H and $\delta^{18}O$ with the fractionation effects described in the introduction. However, the isotope variations could be caused by other factors. The trend might indicate seasonal or annual variables like input of meteoric H_2O which might increase the δ^2H of the ambient seawater which *M. annularis* includes in its skeleton voids. Yet, this interpretation complicates the slight increase in $\delta^{18}O$.

The trend cannot be observed in the core samples of the coral (Figure 5.2.4). The composition of the included water at various depths in coral cores varies significantly. Therefore, the trend observed in the *M. annularis* colonies could also be an analytical error of the 'Amsterdam Device', since it is sensitive for low amounts of hydrogen.

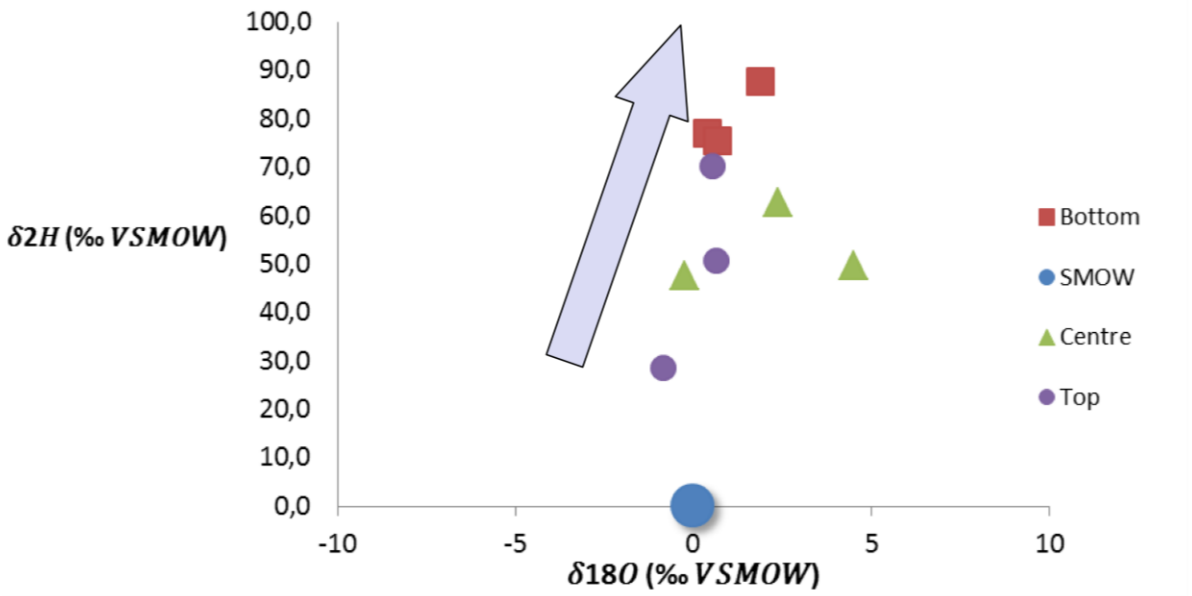

Figure 5.2.3: *A plot of the isotope composition of fluid inclusions in M. annularis colonies including the stable isotope composition of fluid inclusions at various depth in the coral plates. The blue arrow suggests a possible linear fractionation trend.*

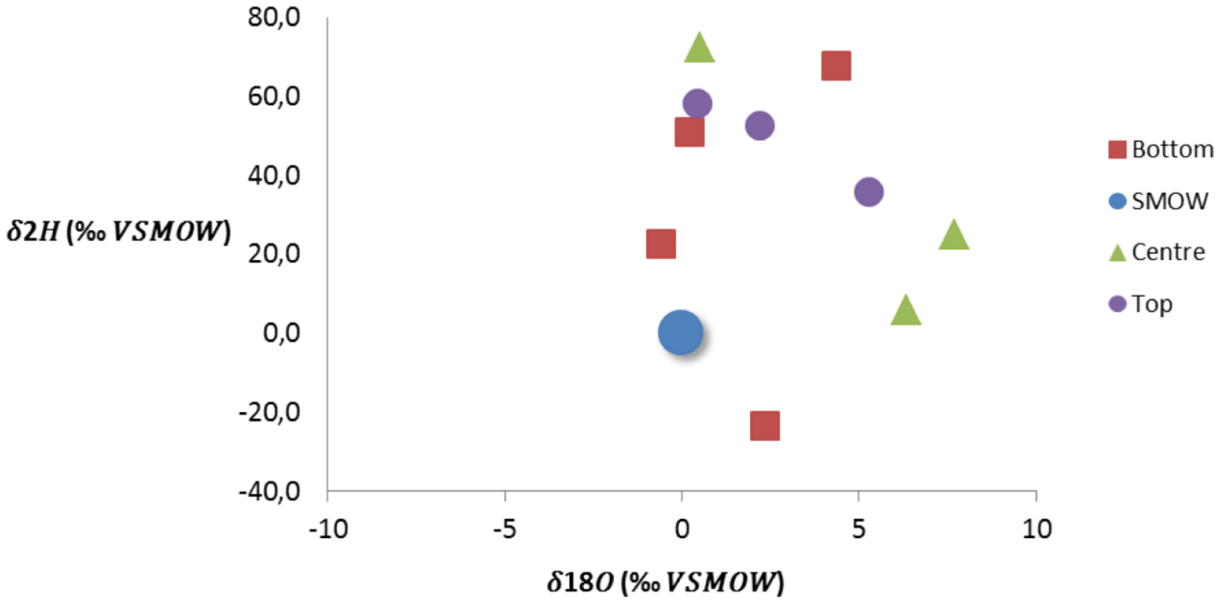

Figure 5.2.4: *A plot of the isotope composition of fluid inclusions in M. annularis at various depths in the coral cores. Whereas a linear trend can be observed in Figure 5.2.3, no trend can be observed in this data.*

Like the *Lophelia* fluid inclusions from the Bahamas, the Curaçao data also show a negative logarithmic relation described by the formula

$$y = -50.58\ln(x) + 236.66,$$

in which $x = Area\ H2$ and $y = \delta^2 H$ (‰ vs VSMOW) and $R^2 = 0.7618$. The trend suggests a relationship between a low amount of released hydrogen and a relatively high measured hydrogen value (VSMOW) of the fluid inclusions. In other words, the higher the amount of hydrogen released, the more likely the $\delta^2 H$ of the fluid inclusions will be equivalent to seawater.

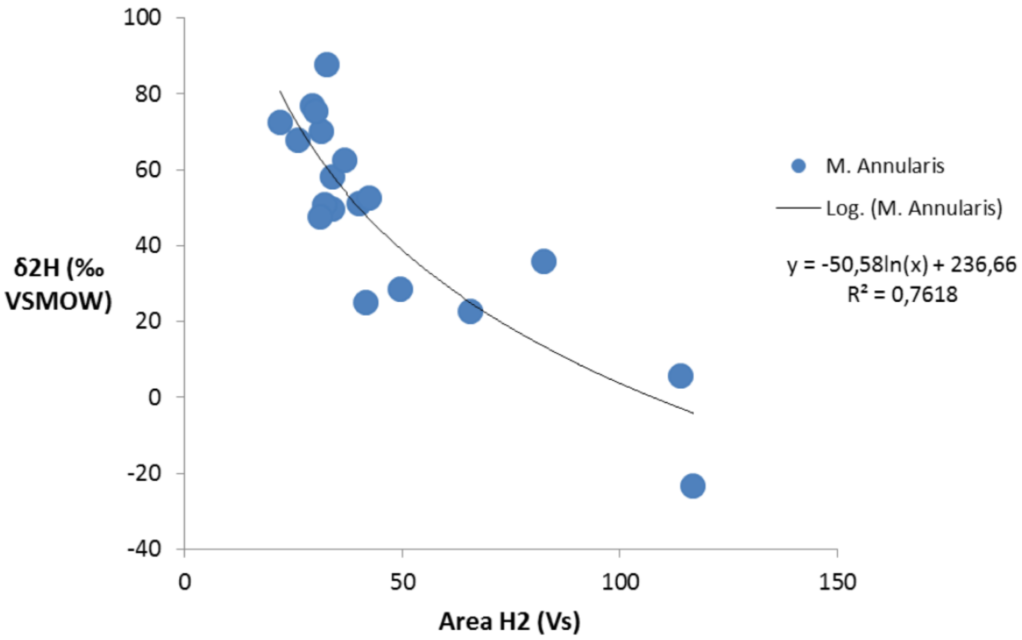

Figure 5.2.5: *A plot of the area H_2 (Volt × seconds) versus the $\delta^2 H$ (‰ VSMOW) of the fluid inclusions in M. annularis indicating the sensitivity of the 'Amsterdam Device' to low amounts of hydrogen.*

The clear trend regarding the sensitivity of the 'Amsterdam Device' to low amounts of hydrogen can not be observed in Figure 5.2.6. This figure show a plot of the $\delta^{18}O$ (‰ vs VSMOW) vs. Area CO of fluid inclusions in *M. annularis*.

The large variability of the oxygen isotope values is difficult to explain and interpret with this dataset. Although nothing can directly explain the varying isotope values, the data suggests a cluster of ±53% of the values indicated with the red circle in Figure 5.2.2. The oxygen isotope compositions of this cluster show a rather fixed value at SMOW and approximately aligns with the $\delta^{18}O$ value of the seawater at Curaçao (Schmidt, 1999), and might therefore be representative for the ambient seawater.

The isotope composition of the fluid inclusions tends to cluster at the value for seawater, and does not plot anywhere near the isotope equilibrium (-3.34‰) for aragonite at the mean temperature at Curaçao based on Leder (1996). These observations indicate that the included fluid is not affected by any complex fractionation processes described in this report and therefore it is suggested that the included fluid might be representative for the ambient seawater.

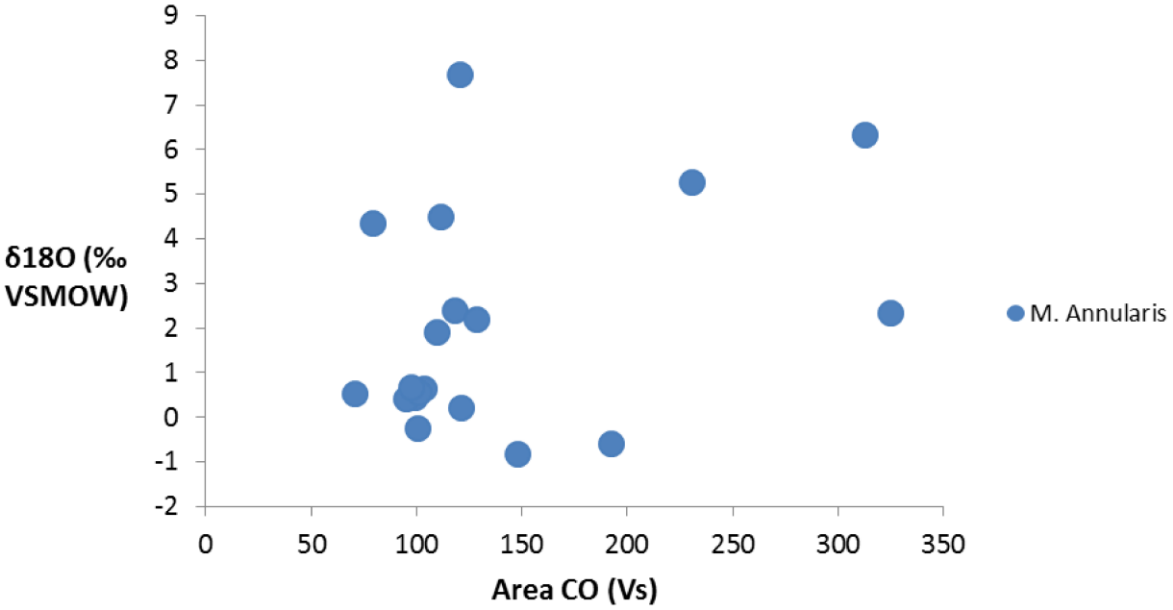

Figure 5.2.6: *A plot of $\delta^{18}O$. (‰ vs VSMOW) vs. Area CO of Fluid Inclusions in M. annularis. No direct link can be observed between the amount of released CO of the fluid inclusion and the $\delta^{18}O$.*

5.3 Analysis of *Montastrea annularis* Carbonate Skeleton Data

In contrast to the fluid inclusions, the skeleton of *M. annularis* does indicate fractionation effects. Figure 5.2.1 shows a plot of the stable isotope data of the carbonate skeleton of *M. annularis* specimen 2, 3, 4 and 7, which represent colonies. The measurement is a bulk analysis of the crushed sample. Therefore, the accuracy of the measurements is rather questionable. However, some observations can be made from this data. Firstly, the individual coral specimens plot relatively close together. The oxygen isotope data of the various specimens show more or less fixed values.

Sample 3 shows the highest $\delta^{18}O$ (-4,1 to -4,3 ‰). The other samples plot less fixed but with significantly lower values (-4,7 to -5,1 ‰) than Sample 3, suggesting that there is a significant difference between different samples (cores and colonies) of *M. annularis.* Weber (1975) concluded that $\delta^{18}O$ of the skeleton of *M. annularis* should increase with increasing depth. This does not align with these results, since *M. annularis 3* (core) was obtained from a depth lesser than other coral specimens (colonies).

M. annularis 2, 4 and 7 show a significant positive offset $\delta^{13}C$ with respect to *M. annularis 3.* This pattern is similar to the pattern Weber and Woodhead (1972) observed. Therefore, a 'vital effect' (photosynthesis) is suggested as possible cause for a relative increase of $\delta^{13}C$.

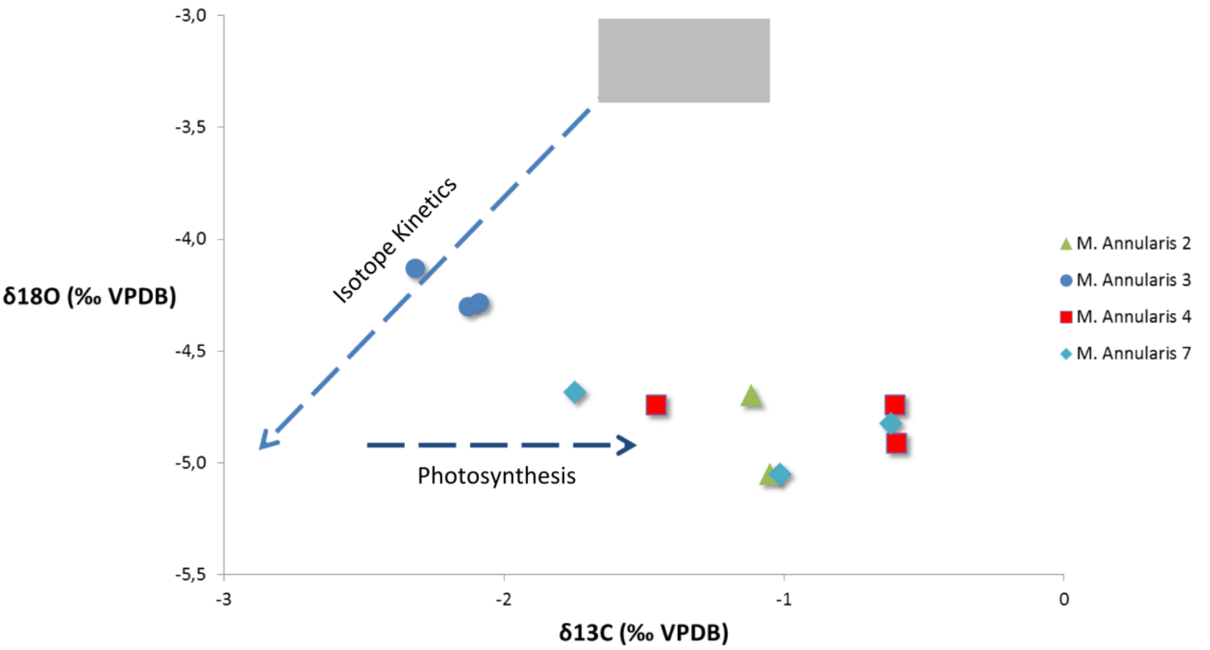

Figure 5.2.1: *A plot of the stable isotopes of the carbonate skeleton of various individual M. annularis specimens (cores and colonies) showing significant different stable isotope values between M. annularis cores (3) and colonies (2, 4, and 7). A possible cause for these variations are 'vital effects' (photosynthesis).*

5.4 Analysis of *Montastrea annularis* Fluid Inclusions; HD and LD banding

Figure 1.4.3 schematically illustrates the interpretation of the skeletal structure of *M. annularis* of Dodge (1974), indicating the main skeletal elements and the areas of HD- and LD-banding. The banding occurs in the exothecal part of the skeleton which consists of a mosaic of void space. According to this interpretation, HD bands consist of less void space in comparison to LD bands. Therefore, more fluid is expected in the LD bands of the skeleton. This hypothesis aligns with the data of this study and is shown in Figure 5.4.1. The figure shows the average area of CO and H_2 of the fluid inclusions of *M. annularis* from Curaçao. Since the area is a measure for the amount of CO and H_2 in the fluid inclusion, there can be concluded that the LD bands contain more amounts of fluid with respect to the HD bands, suggesting that ambient seawater is 'captured' as an inclusion in the voids of the skeleton of *M. annularis.*

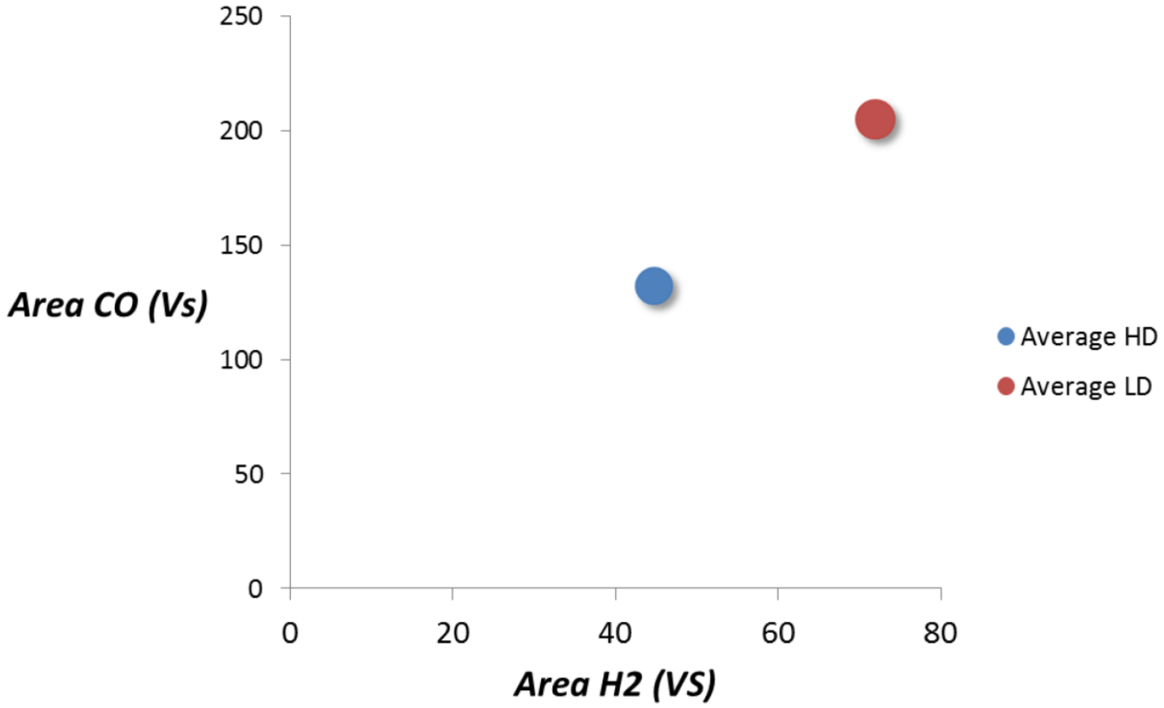

Figure 5.4.1: *A plot of the average Area CO (Vs) versus the average Area H_2 of fluid inclusions in HD and LD bands in M. annularis indicating a larger amount of fluid present in LD bands with respect to HD bands.*

To determine if there is a distinct difference in isotope composition of the included fluid between LD and HD bands, the values were compared (Figure 5.2.5). In general, it is difficult to observe trends in this data, suggesting that the fluid in the voids is not influenced by metabolic or kinetic processes. Whereas both the LD and the HD bands show similar variations in $\delta^{18}O$, HD bands show significant higher $\delta^{2}H$ with respect to LD bands. This pattern is interpreted as the cause of higher evaporation rates because Weber (1975) considered the HD bands to form in the months of warmest water temperature. During this months, seawater has slightly a higher $\delta^{2}H$ value due to the fact that ^{1}H tends to evaporate first, rather than ^{2}H (Graig and Gordon, 1965). Therefore, the assumed included ambient seawater in the HD bands has a higher $\delta^{2}H$ value in comparison with LD bands

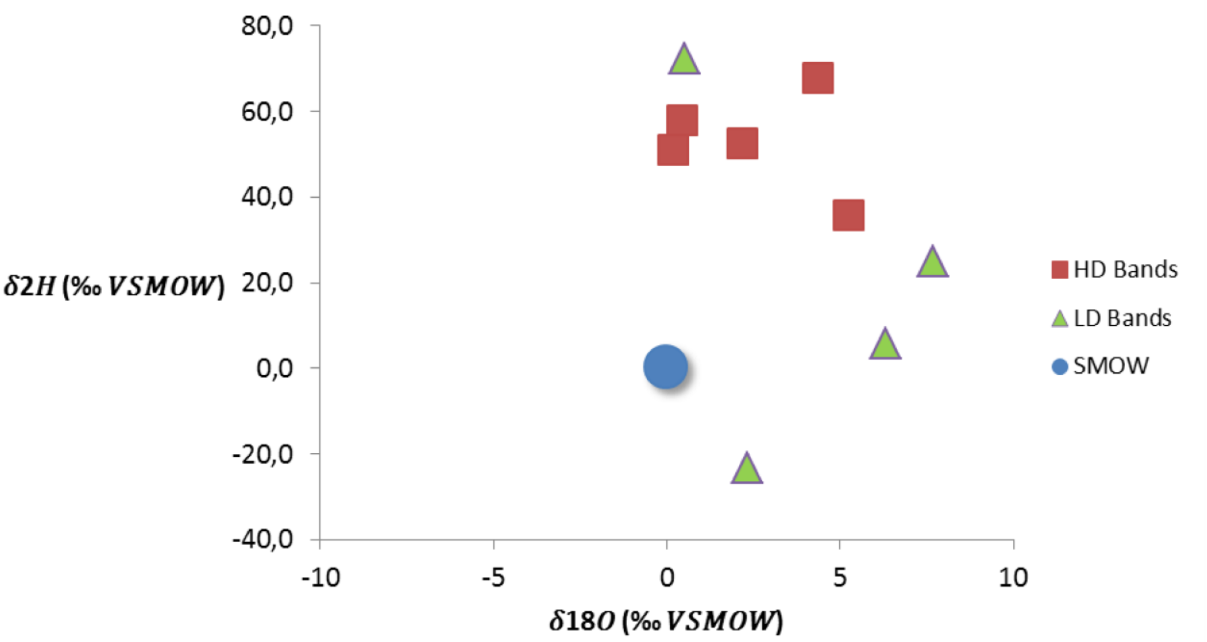

***Figure 5.2.5:** A plot of the stable isotopes of fluid inclusions in M. annularis HD and LD bands indicating higher* $\delta^{2}H$ *in HD with respect to LD bands, suggesting a seasonal effect.*

5.5 *Montastrea annularis* and *Lophelia pertusa* Fluid Inclusions: Applicability for paleothermometry

The stable isotopes of fluid inclusions in *L. pertusa* show a linear trend (Fig. 5.1.2). Generally, the fluid inclusion is higher in $\delta^{18}O$ and lower in $\delta^{2}H$ in relation to SMOW which suggests that fluid inclusions in *L. pertusa* are not of seawater composition and therefore can not be seen to represent ambient seawater values during the time of coral growth. Therefore, fluid inclusions in *L. pertusa* can not be used as application for paleothermometry. However, they can be used for understanding the metabolic processes in *L. pertusa.*

However, the analyses on the fluid inclusions in *M. annularis* described above indicated that the included fluid might be representative for the ambient seawater. First of all, the majority of the stable isotopes measurements of fluid inclusions of *M. annularis* show a more fixed composition (Fig. 5.2.3). The isotope values are clustered around approximately 0 to 0.5‰ for $\delta^{18}O$ and 50 – 60‰ for $\delta^{2}H$. The $\delta^{18}O$ is nearly equivalent to SMOW and close to the assumed isotope composition of the seawater at Curaçao suggesting no complex fractionation processes to occur. Secondly, differences in isotope composition between fluid inclusions in HD and LD bands indicate seasonal effects influencing the seawater composition, suggesting ambient seawater to be included in the skeleton voids and there are no indications of fractionation effects in the fluid inclusions.

As mentioned before, Leder et. al. (1996) suggested that the relationship between temperature and the $\delta^{18}O$ of the *M. annularis* could be expressed by the equation:

$$T\ (^{\circ}\ C) = 5.33 - 4.519(\delta^{18}O_{ar} - \delta_{w})\ ,$$

Figure 5.5.1. shows the oxygen isotope composition of the fluid inclusions in *M. annularis* ($\delta^{18}O$) versus the ambient seawater temperature, calculated with the equation from Leder et. al. (1996). The data suggests a linear trend described by the formula

$$y = 4.3349x + 27.407,$$

in which $y =$ the calculated ambient seawater temperature in °C and $x =$ the oxygen isotope composition of fluid inclusions in *M. annularis* ($VSMOW$) and $R^{2} = 0.9653$. Since the fluid inclusions are considered to be representative for ambient seawater values ($\delta^{18}O \cong 0$), only the data points which plot in the blue circle of Figure 4.2.1 are used for this calculation.

The calculated temperatures are in the range of 21.6 to 34.2 °C and fall between the two blue dashed lines. The mean annual ocean water temperature at Curaçao is 26,5°C *(http://www.ospo.noaa.gov).* According to Kinsman et al. (1969), temperatures at which evaporites can be deposited are as high as 35-40°C and even tend to be as high as 60°C. Therefore, the upper boundary sea water temperatures calculated with the isotopic composition of fluid inclusions of 34.2°C are assumed to be realistic. On the other hand, Katsaros and Buettner (1969) concluded that large amounts of rainfall can significantly drop the Sea Surface Temperature. Therefore, the lower boundary of sea water temperatures calculated with the isotopic composition of fluid inclusions of 21.6°C also can be considered to be a realistic temperature estimate.

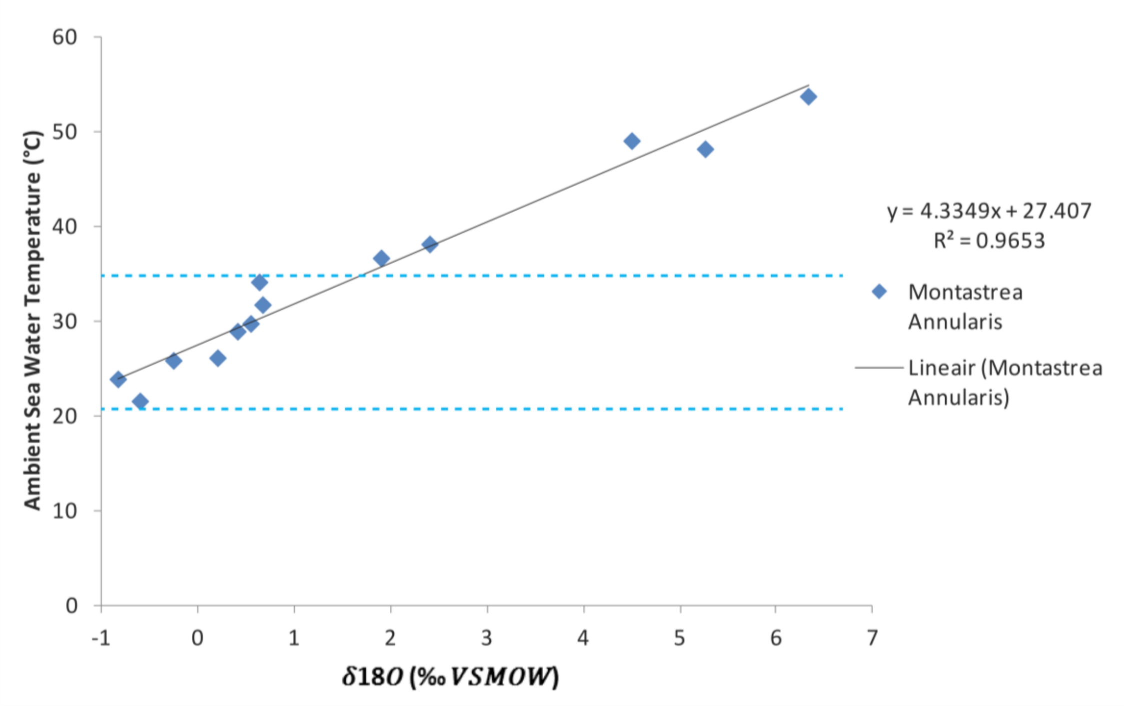

Figure 5.5.1 *Stable isotopes of fluid inclusions in M. annularis versus the ambient sea water temperature. The blue dashed lines represent the assumed lower and upper boundary of realistic sea surface water temperature at Curaçao..*

The fact that fluid inclusion and the carbonate skeleton data provide a number of realistic seawater temperatures by using the formula constructed by Leder et. al. (1996) also suggest that the fluid inclusions in *M. annularis* are representative for the ambient seawater during the time of coral growth. In contrast to *L. pertusa*, the fluid inclusions of *M. annularis* might be applicable for reconstructing paleo-seawater temperatures.

6. Conclusions

1. On average, the stable isotope composition of the inclusion fluid in *L. pertusa* is higher in $\delta^{18}O$ and lower in $\delta^{2}H$ in comparison to VSMOW, suggesting that the fluid in cold-water corals is not of seawater composition. Four data points are considered to be invalid due to analytical problems of the 'Amsterdam Device' and can be explained statistically. The stable isotope variations of fluid inclusions in this study coincide with the variations of Feenstra (2013) which shows a linear trend described by the formula $y = 6.1212x - 30.147$

2. Kinetic fractionation is suggested to cause the simultaneous depletion of $\delta^{2}H$ and $\delta^{18}O$. However, the fact that the fluid values are also enriched with respect to equilibrium, complicates this interpretation. Rayleigh fractionation should therefore be considered as possible mechanism for the isotope variations in fluid inclusions, since the chemical system is open and the trend is similar to the Global Meteoric Water Line

3. On average, the stable isotope composition of the inclusion fluid in *M. annularis* is higher for both $\delta^{18}O$ and $\delta^{2}H$ in relation to VSMOW. The majority of the data points plots at approximately 0 to 0.5 for $\delta^{18}O$ and 50 – 60 for $\delta^{2}H$, suggesting that the fluid in the tropical coral is of seawater composition. However, the positive value of $\delta^{2}H$ is not equivalent to seawater composition. A possible explanation for this is an analytical problem of the 'Amsterdam Device', which is sensitive for the low amounts of H_2 released during crushes of *M. annularis*.

4. LD bands contain significant more amounts of fluid with respect to HD bands. In addition, HD bands show significant higher $\delta^{2}H$ with respect to LD bands, suggesting a seasonal effect to cause the isotope variations of the seawater.

5. A distinction was made between *M. annularis* cores (less than 10m water depth) and colonies (20 m water depth). Coral colonies show significant less variation in both $\delta^{2}H$ and $\delta^{18}O$, suggesting that they are more suitable for fluid inclusions analyses than coral cores. Isotope compositions of fluid inclusions in colonies indicate minor fractionation effects, suggesting a seasonal effect. However, trends can not be observed in coral cores.

6. Since the oxygen isotope composition of the inclusion fluid in *M. annularis* is of seawater composition, fluid inclusions in *M. annularis* can be used to represent the ambient seawater composition during the time of coral growth. This is confirmed with oxygen paleotemperature calculations. Therefore, it is suggested the fluid inclusions in *M. annularis* can be used for paleothermometry, this in contrast to *L. pertusa.* This technique could in principle be of great value in reconstructing past marine climates.

Future Work

For future work, I suggest an enlargement of the crushing chamber of the ‘Amsterdam Device’. This will probably lead to a higher Area of H_2 and CO and thus to more reliable measurements of the stable isotope compositions. Furthermore, this study suggests that fluid inclusions of *M. annularis* are suitable for paleothermometry. However, more detailed and more accurate measurements are needed to confirm this statement. The fractionation processes causing the isotope variations in *L. pertusa* are still not well understood. Therefore, I suggest to study the role of Rayleigh fractionation in biogenic carbonates and their fluid inclusions

Acknowledgements

I would like to thank chief scientist Christian Betzler, the officers and the crew of the *R.V. Meteor* for their support during cruise preparations and at sea. Special thanks go to Prof. Dr. John Reijmer, for giving me the opportunity to join the cruise and to do this project. Furthermore, I would like to thank Eline Feenstra for helping me to work with the ´Amsterdam Device´, constructed by Dr. Hubert Vonhof. I thank Remy van Baal and Suzanne Verdegaal for obtaining the carbonate skeleton data with the Gasbench. I would also like to thank these people for helpful comments and support during this Master Research Project. I thank Prof. Dr. Paul Andriessen and Prof. Dr. John Reijmer for helping me obtaining a financial grant of the ´Stichting Molengraaff Fonds´.

References

Adkins et al., 2003. Stable isotopes in deep-sea corals and a new mechanism for ‘vital effects’. Geochimica et Cosmochimica Acta Vol. 67, No. 6:. 1129-1143.

Alexander, C. S., 1961. The marine terraces of Aruba, Bonaire, and Curaçao (Netherlands Antilles). Annals of the Association of American Geographers 51:102–123.

Anselmetti, F. S., G. P. Eberli, and Z.-D. Ding, 2000. From the Great Bahama Bank into the Straits of Florida: A margin architecture controlled by sea level fluctuations and ocean currents, Geol. Soc. Am. Bull., 112: 829– 844.

Bak, R. P. M., 1975. Ecological aspects of the distribution of reef corals in the Netherlands Antilles. Bijdragen tot de Dierkunde 45:181–190.

Bak, R. P. M., 1977. Coral reefs and their zonation in Netherlands Antilles. American Association of Petroleum Geologists Studies in Geology 4:3–16.

Bak, R. P. M., and B. E. Luckhurst, 1980. Constancy and change in coral reef habitats along depth gradients at Curaçao. Oecologia 47:145–155.

Ball, M. M., 1967a. Tectonic control of the configuration of the Florida-Bahama Platforms. Trans. Gulf Coast Assoc. Geol. Soc., 17: 265-267

Barnes, D.J. and Taylor, D.L., 1973. In situ studies of calcification and photosynthetic carbon fixation in the coral *Montastrea annularis*. Helgoländer wiss. Meeresunters., Bd 24:. 284–291

Beets, D.J., 1972. Lithology and Stratigraphy of the Cretaceous and Danian Succession of Curaçao. - Publications Foundation for Scientific Research in the Caribbean Region, 70: 153

Bosscher, H., 1993. Computerized tomography and skeletal density of coral skeletons. Coral Reefs, 12: 97-103

Bosscher, H., 1992. Growth potential of coral reefs and carbonate platforms. Ph.D. Thesis, VU University Amsterdam

Correa, Thiago B.S., 2012. Variability of cold-water coral mounds in a high sediment input and tidal current regime, Straits of Florida. Sedimentology 59, 1278–1304

Craig, H. and Gordon, L. I., 1965. Deuterium and oxygen-18 variations in the ocean and the marine atmosphere. In E Tongiorgi, ed, Proceedings of a Conference on Stable Isotopes in Oceanographic Studies and Paleotemperatures: 9–130

Cuif and Dauphin, 2005. The Environmental Recording Unit in coral skeletons – a synthesis of structural and chemical evidences for a biochemically driving, stepping-growth process in fibers. Biogeosciences, 2: 61-73.

Curran, H. Allen and Brian White, 1995. Terrestrial and Shallow Marine Geology of the Bahamas and Bermuda. Northampton: Geological Society of America,

De Buisonjé, P. H., 1974. Neogene and Quaternary Geology of Aruba, Curac/ao and Bonaire. Publications Foundation for Scientific Research in the Caribbean, 78, Den Haag

Dietz, R. S., Holden, J. C. and Sproll, W. P., 1970. Geotectonic evolution and subsidence of the Bahama platform. Geol. Soc. Am. Bull., 81: 1915-1928

Dodge R. E., Aller R. C. and Thomson, N. J., 1974. Coral growth related to resuspension of bottom sediments. Nature 247: 574-577

Eberli, G.P. & Ginsburg, R.N., 1987. Segmentation and coalescence of Cenozoic carbonate platforms, northwestern Great Bahama Bank. Geology, 15: 75 79.

Eberli, G.P. & Ginsburg, R.N., 1989. Cenozoic progradation of northwestern Great Bahama Bank, a record of lateral platform growth and sea-level fluctuations. In: Controls on Platform and Basin Development (Eds P.D. Crevello, J.L. Wilson, J.F. Sarg and J.F. Read), Soc. econ. Paleont. Mineral., Spec. Publ., 44: 339–351.

Emiliani, C., 1965. Precipitous Continental Slopes and Considerations on the Transitional Crust. Science, Vol. 147 no. 3654: 145-148

Epstein, S., & Mayeda, T., 1953. Variation of O< sup> 18</sup> content of waters from natural sources. Geochimica et cosmochimica acta, 4(5): 213-224.

Feenstra, E. J., 2013. Stable isotope study of fluid inclusions in cold-water corals from the rockall trough western margin, NE Atlantic Ocean. MSc Research Project, Vrije Universiteit Amsterdam

Freiwald and Roberts, 2005; Cold water Corals and Ecosystems; Springer-Verlag, Berlin Heidelberg, pp. 1243.

Freiwald, A., Henrich, R. and Pätzold, J., 1997. Anatomy of a deep-water coral reef mound from Stjernsund, West-Finnmark, northern Norway. SEPM, Special Publication, 56: 141-161.

Gaffey, 1988. Water in skeletal carbonates. J. Sedim. Petrol., 58: 397– 414

Gagnon et al., 2007. Sr/Ca and Mg/Ca vital effects correlated with skeletal architecture in a scleractinian cold-water coral and the role of Rayleigh fractionation. EPSL 261: 280-295.

Goreau, T. E., 1959. The ecology of Jamaican coral reefs I. Species composition and zonation. Ecology 40: 67-90

Goreau, T.E. and J. W. Wells, 1967. The shallow-water Scleractinia of Jamaica: revised list of species and their vertical distribution range. Bull. Mar. Sci. 17: 442453.

Grasmueck, M., Eberli, G., Correa, T., Viggiano, D. A., Luo, J., Wyatt, G., Reed, J., Wright, A., & Pompon, S., 2007. IAUV-based environmental characterization of deepwater coral mounds in the straits of Florida. In Offshore Technology Conference

Ip, Y.K., Lim, A.L.L., Lim, R.W.L., 1991. Some properties of calcium-activated adenosine triphosphatase from the hermatypic coral Galaxea fascicularis. Mar. Biol., 111: 191–197

Kaszemeik and Freiwald. 2003. *Lophelia pertusa* (Scleractinia) – from skeletal structures to growth patters and morphotypes. Final ACES Delivery report: p.p. 26

Katsaros, K., & Buettner, K. J., 1969. Influence of rainfall on temperature and salinity of the ocean surface. Journal of Applied Meteorology, 8(1): 15-18.

Kendall and McDonnell, 1998. Isotope Tracers in Catchment Hydrology. Elsevier Science B.V. Amsterdam, Chapter 2 Fundamentals of Isotope Geochemistry:. 51-86.

Kinsman, D. J., 1969. Modes of formation, sedimentary associations, and diagnostic features of shallow-water and supratidal evaporites. AAPG Bulletin, 53(4): 830-840.

Laborel, J., 1969. Les peuplements de MadrCporaires des cotes tropicales du BrCsil. Ann. Univ. Ab- idjan, Ecologie, ser. E 2: 1-260

Leder, J. J., Swart, P. K., Szmant, A. M., & Dodge, R. E., 1996. The origin of variations in the isotopic record of scleractinian corals: I. Oxygen. Geochimica et Cosmochimica Acta, 60(15): 2857-2870.

Logan, A., 1988. Holocene reefs of Bermuda. Sedimenta 11: 1-63.

Lynch-Stieglitz, J., Curry, W. B. and Slowey, N., 1999. A geostrophic transport estimate for the Florida Current from the oxygen isotope composition of benthic foraminifera. Paleoceanography, 14, 360–373

Mann, S., 2001. Biomineralization: Principles and Concepts in Bioinorganic Materials Chemistry. Oxford University Press: Ch. 3: 24-37

Marali et al., 2013. Skeletal microstructure and stable isotope signature of three bathyal solitary cold-water corals from the Azores. Palaeography, Palaeoclimatology, Palaeoecology 373, 25-38.

Maresch, W. V., 1974. Plate tectonics origin of the Caribbean mountain system of northern South America: discussion and proposal. Geological Society of America Bulletin, 85(5): 669-682.

Masaferro, J.L., Bulnes, M., Poblet, J. and Eberli, G.P., 2002. Episodic folding inferred from syntectonic carbonate sedimentation: the Santaren anticline, Bahamas foreland. Sedimentary Geology, 146(1-2): 11-24.

McConnaughey, T., 1989. < sup> 13</sup> C and< sup> 18</sup> O isotopic disequilibrium in biological carbonates: II.< i> In vitro</i> simulation of kinetic isotope effects. Geochimica et Cosmochimica Acta, 53(1): 163-171.

McCrea, J.M., 1950. On the isotopic chemistry of carbonates and paleotemperature scale. J. Chem. Phys., 18: 849–857

Meyerhoff, A.A. and Hatten, C.W., 1974. Bahamas salient of North America; Tectonic framework stratigraphy, and petroleum potential. Am. Assoc. Petrol. Geol. Bull., 58: 1201-1239

Mienis et al., 2007. Hydrodynamic controls on cold-water coral growth and carbonate-mound development at the SW and SE Rockall Trough Margin, NE Atlantic Ocean. Deep-Sea Research I 54: 1655-1674.

Mulder, T., Ducassou, E., Eberli, G. P., Hanquiez, V., Gonthier, E., Kindler, P., ... & Pakiades, M., 2012. New insights into the morphology and sedimentary processes along the western slope of Great Bahama Bank. Geology, 40(7): 603-606.

Mullins, H.T., Heath, K.C., H.M. Van Buren, C.R. Newton, 1984. Anatomy of modern open-ocean carbonate slope: Northern Little Bahama Bank Sedimentology, 31: 141–168

Pratz, E., 1882. Über die verwandtschaftlichen Beziehungen einiger Korallengattungen. Palaeontographica, 29: 81-123.

Rogers, A.D., 1999. The Biology of Lophelia pertusa (Linnaeus 1758) and Other Deep-Water Reef-Forming Corals and Impacts from Human Activities. International Review of Hydrobiology, 84: 315–406

Schlager, W. and Ginsburg, R.N., 1981. Bahama carbonate platform- the deep and the past. Mar. Geol., 44: 1-24

Schmidt, G. A., G. R. Bigg, and E. J. Rohling, 1999. Global Seawater Oxygen-18 Database, http://data.giss.nasa.gov/o18data/, NASA Goddard Inst. of Space Sci., New York, N. Y.

Schwarcz, H.P., 1986. Geochronology and isotopic geochemistry of speleothems. Handbook of Environment Isotope Geochemistry, Elsevier, Amsterdam: 271–303

Sheridan, R., 1976. Sedimentary basins of the Atlantic margin of North America, In: M.H.P. Bott (editor), Sedimentary Basins of Continental Margins and Cratons, Tectonophysics, 36 (l-3): 113-132.

Sheridan, R., Crosby, J.T., Bryan, G.M., Stoffa, P.L., 1981. Stratigraphy and Structure of Southern Blake Plateau, Northern Florida Straits, and Northern Bahama Platform from Multichannel Seismic Reflection Data. AAPG Bulletin, 65: 2571-2593

Sheridan, R., Mullins, H., Austin, J.A., Jr., Ball, M. and Ladd, J., 1988. Geology and geophysics of the Bahamas, the Atlantic Continental Margin. Geological Society of America, Vols. 1-2. U.S: 329-364.

Smith et al., 2000. Paleotemperatures from deep-sea corals; overcoming ‘vital effects’. Palaios 15 (1): 25-32.

Tambutté, S., et al., 2011. Coral biomineralization: From the gene to the environment. Journal of Experimental Marine Biology and Ecology 408: 58–78

Tarutani, T., Clayton, R. N., and Mayeda, T. K., 1969. The effects of polymorphism and magnesium substitution on oxygen isotope fractionation between calcium carbonate and water. Geochimica et Cosmochimica Acta. V. 33: 987-996

Urey, H. C., 1947. The thermodynamic properties of isotopic substances. J. Chem. Soc., 562-581.

Van Breukelen and Mienis, 2002. Stable isotope chemistry of corals and other deep water species from carbonate mounds in the NW and SE Rockall Trough area. Vrije Universiteit (VU); unpublished.

Veron J.E.N., Stafford-Smith M.G., 2002. Coral ID. Australian Institute of Marine Science, Townsville. CD-ROM

Vonhof H.B. et. al., 2006; A continuous-flow crushing device for on-line δ^{2}H analysis of fluid inclusion water in speleothems; Rapid Commun. Mass Spectrom.; 20: 2553–2558

Weber, J. N., White, E. W. and Weber, P. H., 1975. Correlation of density banding in reef coral skeletons with environmental parameters: the basis for interpretations of chronological records preserved in the coralla of corals. Paleobiology 1: 137 149

Weber, J. N., & Woodhead, P. M., 1971. Diurnal variations in the isotopic composition of dissolved inorganic carbon in seawater from coral reef environments. Geochimica et Cosmochimica Acta, 35(9): 891-902

van Weering, T.C.E., de Haas, H.,de Stigter, H.C., Lykke-Andersen, H., Kouvaev, I., 2003. Structure and development of giant carbonate mounds at the SW and SE Rockall Trough margins, NE Atlantic Ocean. Mar. Geol. 198: 67–81.

Wells, J.W. , 1956. The Scleractinia. In: Treatise on invertebrate paleontology. Part F: the Coelenterata: 328-444.

Weil, E. and Knowlton, N., 1994. A multi-character analysis of the Caribbean coral *Montastrea annularis* and its two sibling species, *M. faveolata* and *M. franski*. Bulletin of Marine Science 55(1): 151-175.

Wilson, J. B., 1979b. 'Patch' development of the deep-water coral Lophelia pertusa (L.) on Rockall Bank. – Journal of Marine Biology Ass. U.K. V. 59: 165-177.

Appendix I: *Lophelia Pertusa* sampling photos

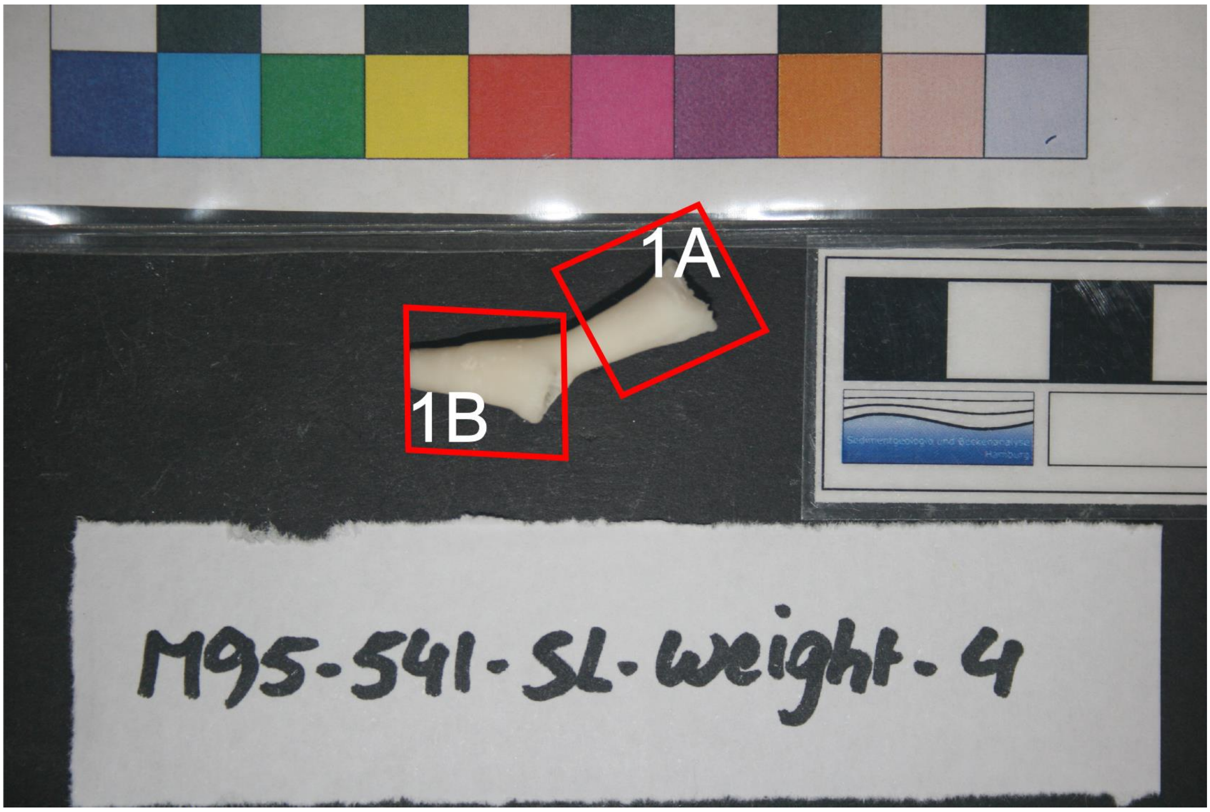
1A
1B
M95-541-SL-weight-4

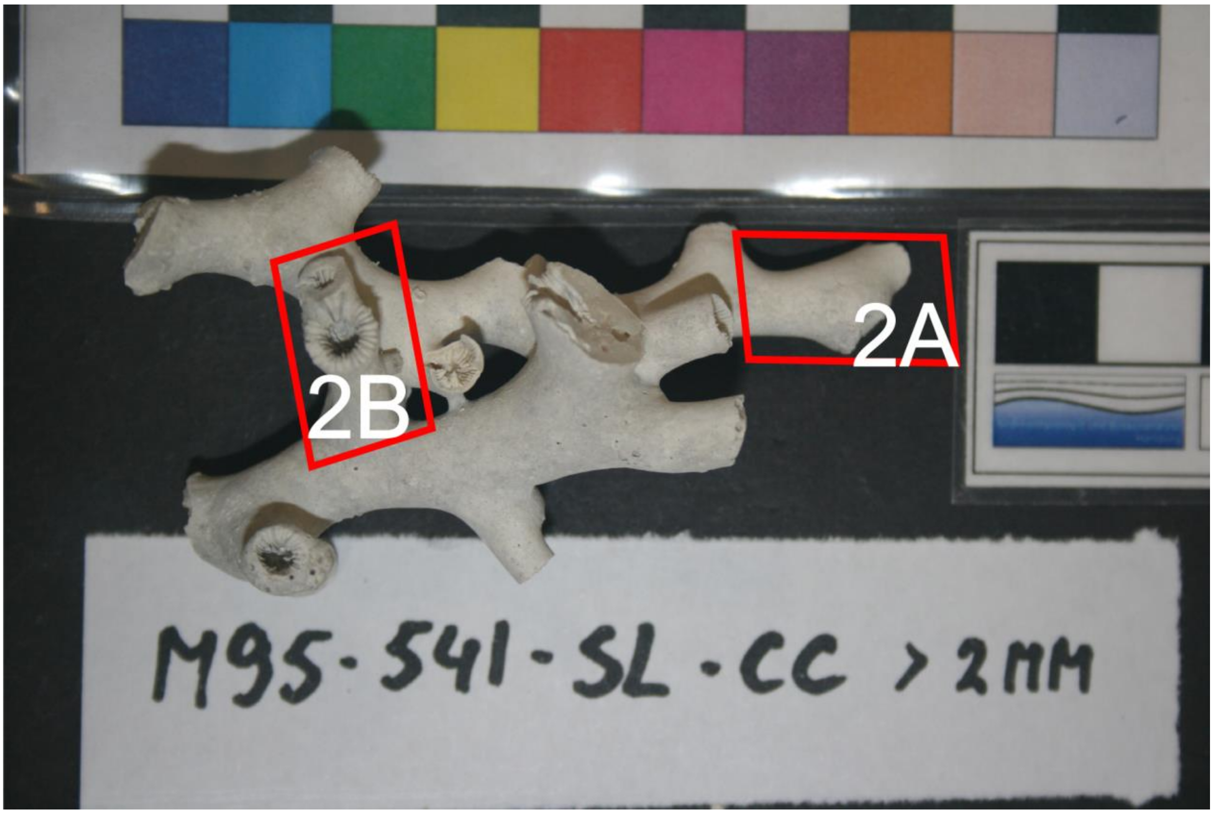
2B
2A
M95-541-SL-CC >2MM


3B
3A
3C
M95 · 541 · SL · weight · 6


4A
4B
M95 · 541 · SL · weight · 7

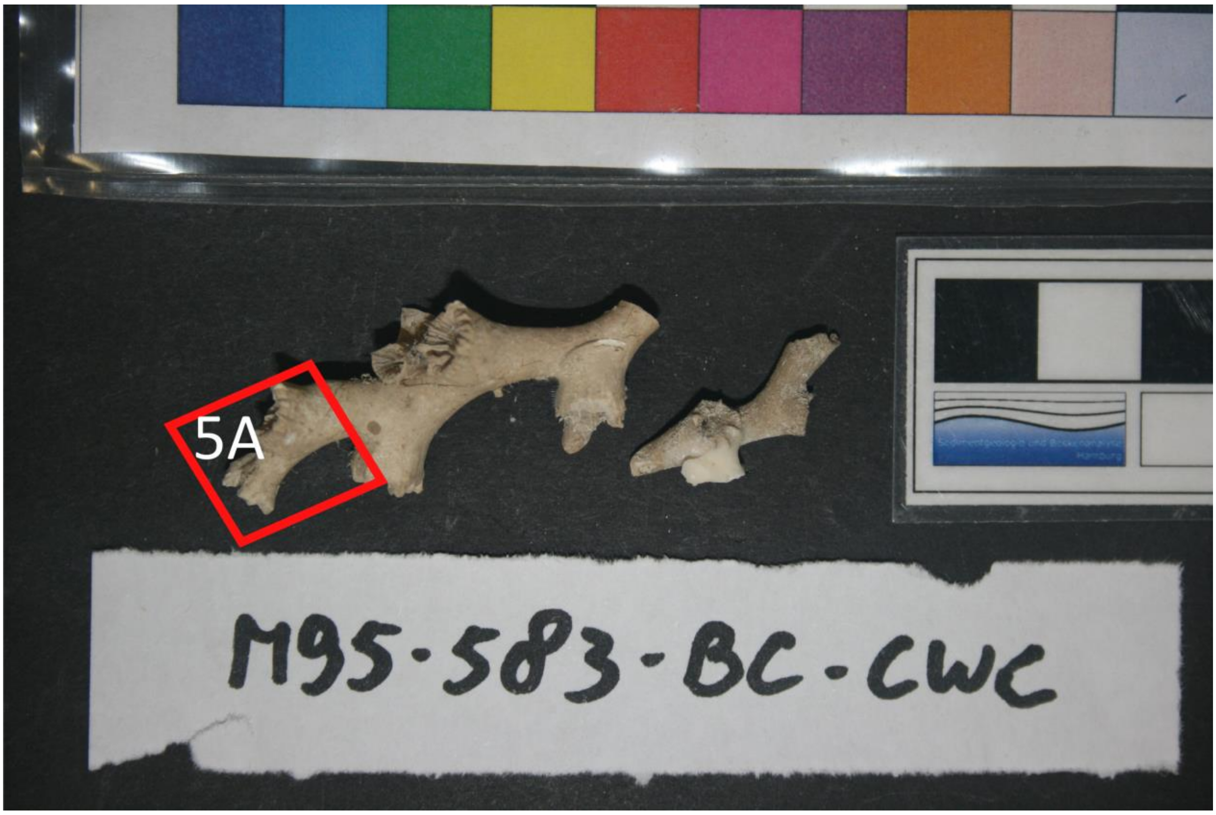
5A
M95-583-BC-CWC


6B
6A
M95-541-SL-weight-3-C

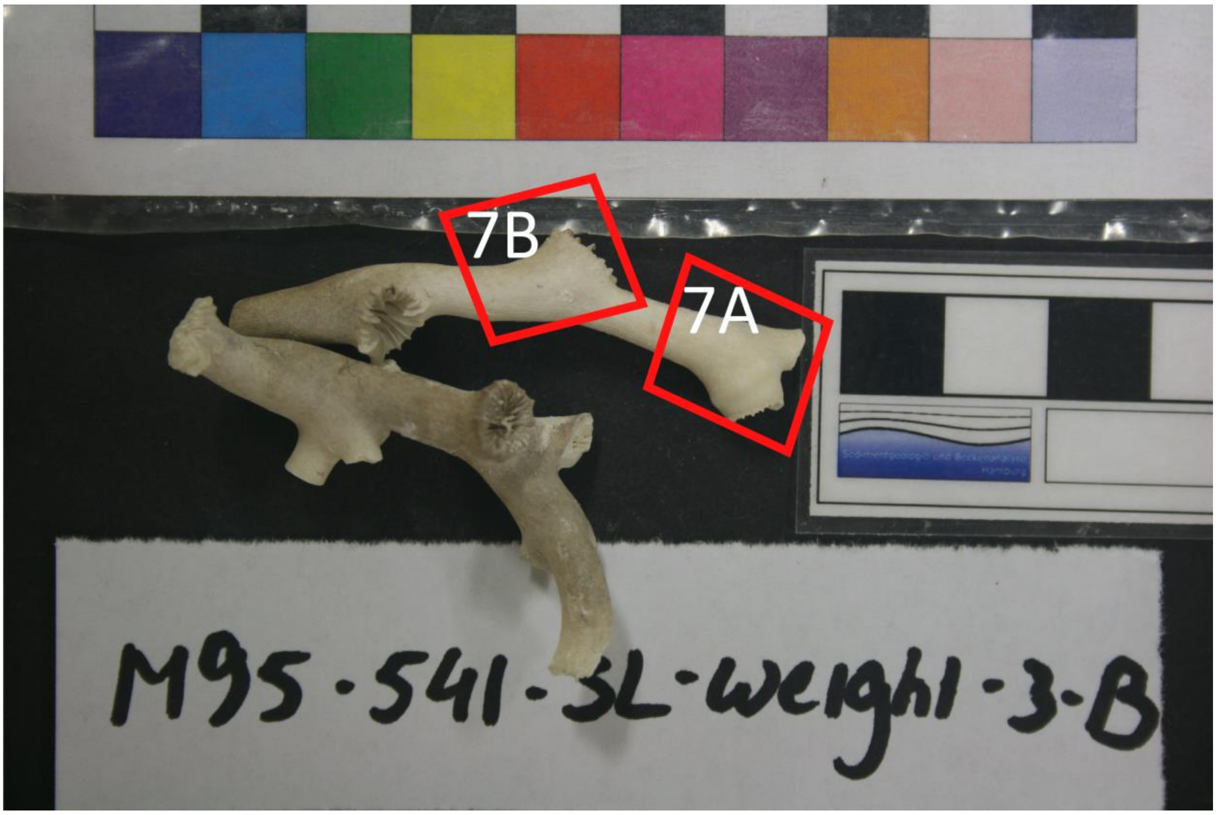
7B
7A
M95-541-SL-weight-3-B


8A
8B
M95-541-SL-weight-3-A


9A
M95-583-BC


10A
M95-540-BG Ⓐ

Appendix II: *Montastrea Annularis* sampling photos


1.3
1.2
1.1
X
O
X
1
5 cm

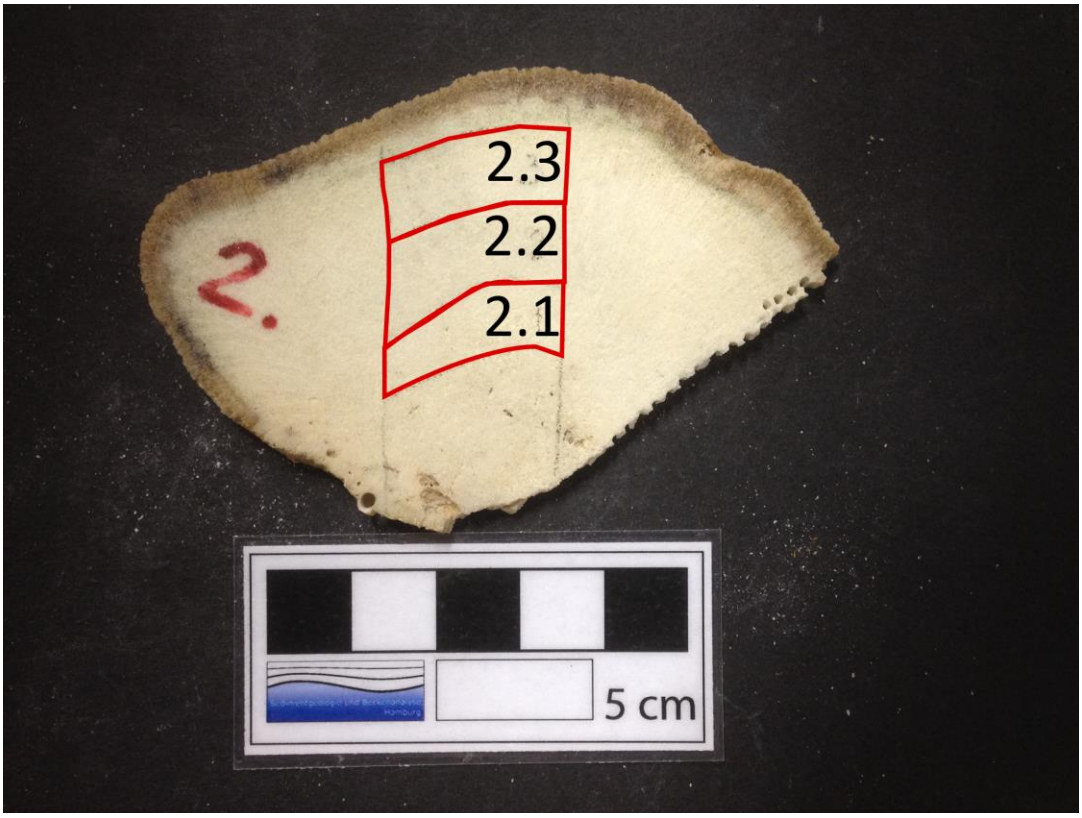
2.
2.3
2.2
2.1
5 cm

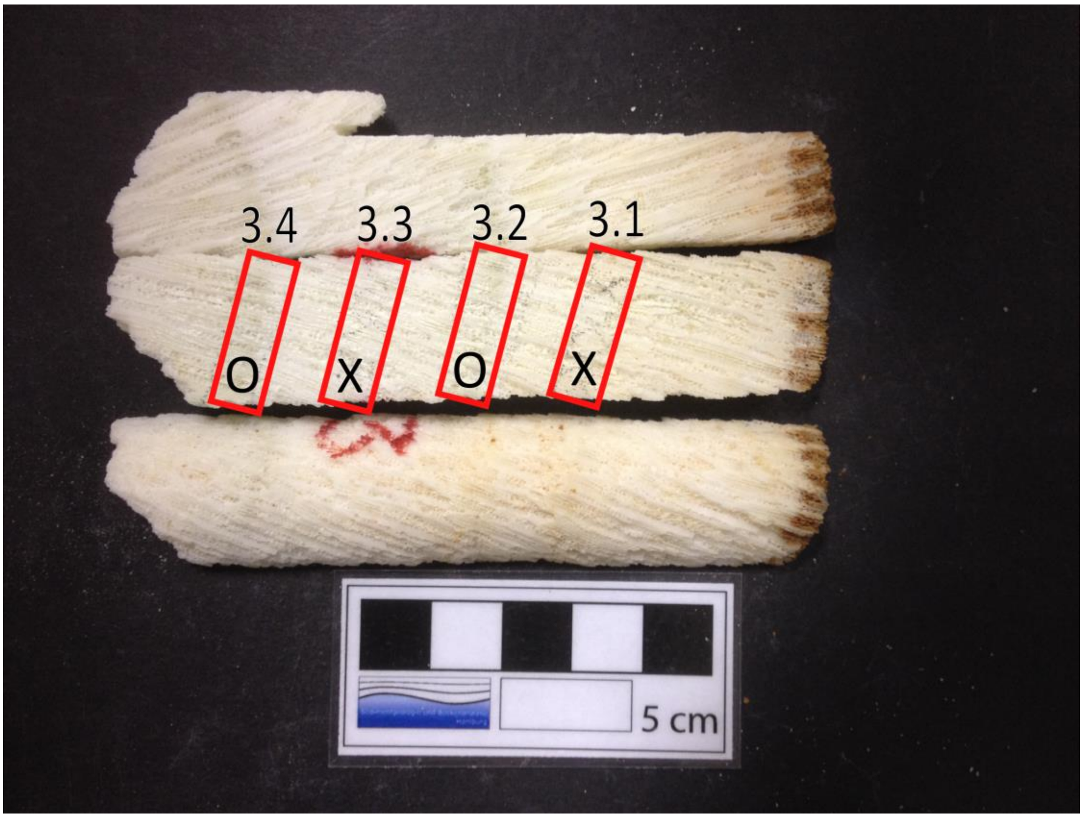
3.4
3.3
3.2
3.1
O
X
O
X
5 cm


4.3
4.2
4.1
5 cm


5.5
5.3
5.1
O
X
O
X
O
X
5.6
5.4
5.2
5
5 cm

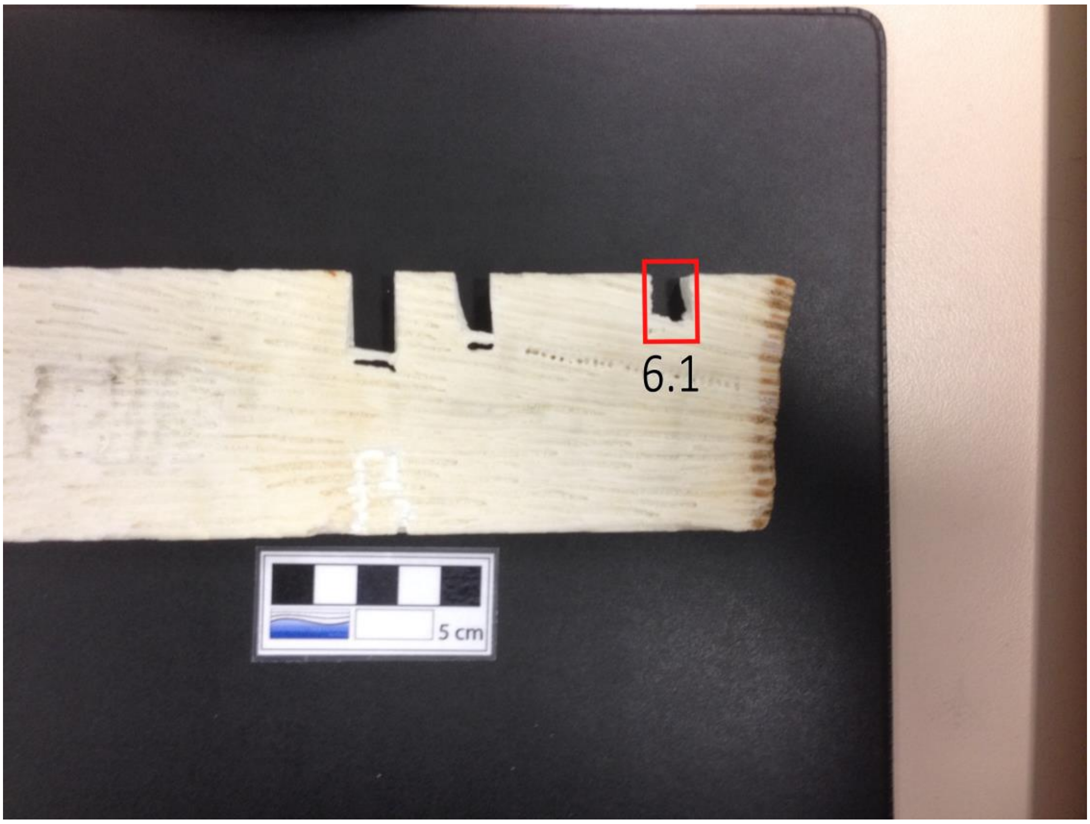
6.1
5 cm

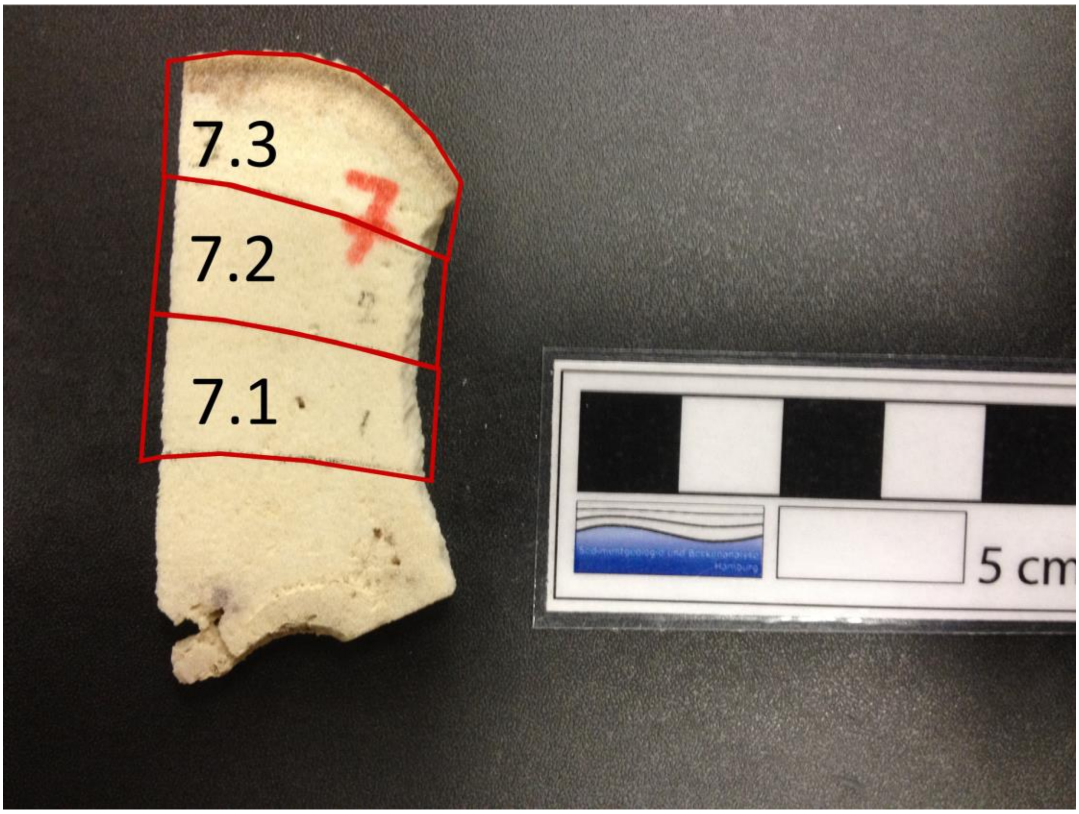
7.3
7
7.2
7.1
5 cm

Appendix III: *Lophelia Pertusa* Fluid Data

Sample	Area H2	δ2H	Area CO	δ18O	Area H2	δ2H	Area CO	δ18O	δ18O corr	d2H corr	Weight
16 May 1A											
DNS 3 0,2 µL	210,50	-60,20	616,80	-25,30							
DNS 3 0,2 µL	156,10	-44,90	446,60	-24,90							
DNS 3 0,21 µL	155,50	-41,40	439,50	-24,50							
DNS 3 0,22 µL	162,10	-37,00	469,90	-23,00							
DNS 3 0,22 µL	170,40	-39,00	481,00	-23,40							
Crush 1A					47,90	-49,60	137,30	-12,90	4,49	-15,3	0,55g
DNS 3 0,05 µL	46,80	-44,20	133,00	-18,70							
22 May 1B											
DNS 3 0,2 µL	360,50	-63,90	1031,50	-15,60							
DNS 3 0,2 µL	220,10	-48,20	604,40	-25,80							
DNS 3 0,2 µL	178,80	-45,40	492,90	-25,90							
DNS 3 0,2 µL	149,60	-39,20	400,90	-25,30							
DNS 3 0,2 µL	135,50	-38,80	359,00	-25,10							
Crush 1B					75,70	-44,20	211,00	-13,10	4,69	-12,0	0,65g
DNS 3 0,08 µL	84,90	-41,90	236,30	-19,10							
DNS 3 0,09 µL	66,50	-41,00	181,60	-19,70							

Sample	Area H2	δ2H	Area CO	δ18O	Area H2	δ2H	Area CO	δ18O	δ18O corr	d2H corr	Weight
23 May 2B											
DNS 3 0,2 µL	268,80	-57,30	761,50	-17,50							
DNS 3 0,2 µL	200,60	-47,50	547,00	-28,40							
DNS 3 0,2 µL	190,90	-43,70	519,20	-22,90							
DNS 3 0,2 µL	166,80	-41,80	448,80	-27,20							
DNS 3 0,2 µL	154,20	-46,10	417,00	-26,60							
DNS 3 0,2 µL	143,90	-39,20	380,40	-26,50							
Crush 2B					144,70	-45,80	398,50	-20,20	4,69	-12,8	0,65g
DNS 3 0,18 µL	148,60	-42,70	401,40	-26,20							
24 May 3B											
DNS 3 0,2 µL	346,90	-57,30	962,70	-28,90							
DNS 3 0,2 µL	276,90	-52,30	799,30	-19,90							
DNS 3 0,2 µL	217,30	-60,10	635,90	-20,90							
DNS 3 0,2 µL	205,30	-46,50	581,00	-27,80							
DNS 3 0,2 µL	183,60	-44,50	511,50	-26,90							
DNS 3 0,2 µL	176,80	-43,30	481,40	-26,50							
Crush 3B					249,50	-58,30	698,50	-18,30	3,87	-23,7	0,95g
DNS 3 0,26 µL	215,80	-45,00	588,90	-23,50							
DNS 3 0,28 µL	213,80	-40,80	574,30	-23,80							

Sample	Area H2	δ2H	Area CO	δ18O	Area H2	δ2H	Area CO	δ18O	δ18O corr	d2H corr	Weight
28 May 4A											
Keila 2 0,2 µL	370,10	-99,50	1105,50	-17,70							
Keila 2 0,2 µL	243,50	-109,20	701,40	-33,60							
Keila 2 0,2 µL	176,90	-120,70	498,50	-34,80							
Keila 2 0,2 µL	170,90	-130,70	475,60	-37,10							
Keila 2 0,2 µL	152,80	-140,70	431,50	-37,90							
DNS 3 0,2 µL	159,20	-45,30	440,40	-25,00							
DNS 3 0,2 µL	158,10	-38,30	438,50	-24,40							
DNS 3 0,21 µL	146,10	-42,90	410,20	-24,60							
DNS 3 0,22 µL	173,00	-42,20	483,40	-24,50							
DNS 3 0,22 µL	171,90	-41,40	483,40	-23,70							
Crush 4A					50,10	-48,30	145,40	-15,60	2,45	-10,0	0,95g
DNS 3 0,6 µL	45,10	-47,80	130,70	-19,40							
DNS 3 0,55 µL	56,80	-41,40	161,10	-21,10							
29 May 4B											
DNS 3 0,2 µL	291,50	-64,30	881,60	-20,30							
DNS 3 0,2 µL	213,20	-40,10	604,9	-24,40							
DNS 3 0,2 µL	180,70	-38,90	508,7	-24,20							
DNS 3 0,2 µL	171,60	-39,40	480,5	-24,00							
Crush 4B					61,40	-43,80	178,7	-17,00	2,24	-10,9	0,95g
DNS 3 0,06 µL	54,30	-42,50	156,3	-20,60							
DNS 3 0,065 µL	55,00	-43,70	155,8	-22,00							

Sample	Area H2	δ2H	Area CO	δ18O	Area H2	δ2H	Area CO	δ18O	δ18O corr	d2H corr	Weight
29 May 5A											
DNS 3 0,2 µL	136,70	-43,30	369,7	-26,10							
DNS 3 0,2 µL	126,70	-44,70	364,1	-26,00							
DNS 3 0,2 µL	120,40	-42,80	328,6	-25,80							
DNS 3 0,21 µL	130,90	-40,40	355,7	-25,60							
Crush 5A					61,70	-61,30	178,7	-20,80	2,45	-4,9	0,95g
DNS 3 0,09 µL	90,70	-65,60	266,3	-24,60							
DNS 3 0,08 µL	74,30	-49,60	208,9	-24,30							
13 June 3C											
DNS 3 0,2 µL	121,90	-53,20	340,10	-25,00							
DNS 3 0,2 µL	122,30	-38,90	331,00	-24,80							
DNS 3 0,2 µL	125,10	-40,00	338,90	-24,50							
DNS 3 0,2 µL	120,00	-41,20	328,30	-24,70							
Crush 3C					72,90	-50,00	216,20	-12,70	5,81	-15,3	0,85g
DNS 3 0,1 µL	74,90	-44,60	213,00	-19,80							
3 September 5B											
DNS 3 0,2 µL	67,902	-52,22	174,338	-19,618							
DNS 3 0,21 µL	72,993	-65,875	192,007	-19,935							
DNS 3 0,22 µL	71,726	-61,963	187,011	-21,72							
DNS 3 0,22 µL	70,114	-49,422	182,74	-22,277							
Crush 5B	11,704	-91,121	0	0							0,95g
DNS 3 0,03 µL	16,107	117,797	44,467	-24,005							
DNS 3 0,02 µL	5,232	-121,13	60,427	0							

Sample	Area H2	δ2H	Area CO	δ18O	Area H2	δ2H	Area CO	δ18O	δ18O corr	d2H corr	Weight
4 September 7A											
DNS 3 0,2 µL	170,691	-95,057	428,6	-27,611							
DNS 3 0,21 µL	125,377	-97,264	331,334	-27,297							
DNS 3 0,21 µL	104,922	-91,357	284,158	-26,44							
DNS 3 0,22 µL	94,439	-103,01	252,391	-27,456							
Crush 7A					55,053	135,892	165,693	-22,853	3,90	-24,5	-
DSN 3 0,10 µL	40,183	121,873	107,925	-28,08							
DSN 3 0,11 µL	40,762	-79,328	111,736	-25,038							
4 september 8A											
DNS 3 0,2 µL	288,742	113,418	794,581	-32,42							
DNS 3 0,2 µL	143,358	127,662	384,291	-30,244							
DNS 3 0,21 µL	115,003	119,188	315,857	-29,808							
DNS 3 0,22 µL	83,393	121,863	238,976	-28,268							
Crush 8A					104,512	-132,427	278,956	-25,77	-0,14	-25,6	-
DSN 3 0,25 µL	94,533	117,378	255,208	-27,035							
DSN 3 0,26 µL	94,438	106,384	257,525	-27,002							
4 september 6B											
DNS 3 0,2 µL	278,828	136,776	815,372	-27,031							
DNS 3 0,2 µL	113,143	122,323	312,849	-29,56							
DNS 3 0,21 µL	74,114	117,883	206,316	-30,527							
DNS 3 0,22 µL	76,372	121,311	210,352	-30,646							
Crush 6B					18,382	-4,71	54,864	-24,575	3,83	65,8	-
DNS 3 0,06 µL	19,051	-75,059	57,275	-29,735							
DNS 3 0,04 µL	12,842	-22,034									
DNS 3 0,05 µL	5,883	14,127									

Sample	Area H2	δ2H	Area CO	δ18O	Area H2	δ2H	Area CO	δ18O	δ18O corr	d2H corr	Weight
5 september 9A											
DNS 3 0,2 µL	0	0	1270,818	-17,201							
DNS 3 0,2 µL	214,96	110,623	588,533	-23,693							
DNS 3 0,2 µL	189,449	118,136	537,638	-23,548							
DNS 3 0,2 µL	172,106	123,151	480,256	-24,892							
DNS 3 0,21 µL	169,53	103,947	462,427	-24,79							
Crush 9A					36,992	-41,186	116,224	-25,342	5,1694	77,6	-
DNS 3 0,04 µL	53,56	122,613	142,676	-31,812							
DNS 3 0,035 µL	51,294	154,452	149,186	-31,552							
22 october 7B											
DNS 3 0,2 µL	104,029	-31,22	294,19	-24,268							
DNS 3 0,2 µL	157,801	101,384	449,107	-24,836							
DNS 3 0,2 µL	149,239	-75,786	385,744	-24,74							
DNS 3 0,2 µL	29,391	-28,623	89,085	-23,727							
DNS 3 0,21 µL	162,379	-98,833	418,691	-24,704							
Crush 7B					45,793	108,347	128,452	-18,092	3,26302	-0,4	0,85g
DNS 3 0,05 µL	42,665	116,812	120,43	-22,693							
22 October 8B											
DNS 3 0,2 µL	554,79	102,035	1526,32	-14,898							
DNS 3 0,2 µL	314,672	-58,367	846,648	-7,617							
DNS 3 0,2 µL	217,061	-59,01	591,409	0,801							
DNS 3 0,20 µL	180,61	-58,689	474,857	-25,231							
DNS 3 0,21 µL	191,846	-62,53	503,139	-24,512							
Crush 8B					162,9	-68,65	403,513	-25,972	-5,9435	-20,6	0,95g
DNS 3 0,17 µL	144,449	-58,253	382,797	-21,547							
DNS 3 0,18 µL	135,515	-70,266	356,924	-22,453							

Sample	**Area H2**	**δ2H**	**Area CO**	**δ18O**	**Area H2**	**δ2H**	**Area CO**	**δ18O**	**δ18O corr**	**d2H corr**	**Weight**
24 october 10A											
DNS 3 0,2 µL	268,863	-76,461	693,983	-18,97							
DNS 3 0,2 µL	156,713	-41,611	415,229	-20,562							
DNS 3 0,2 µL	155,339	-54,218	410,555	-20,948							
DNS 3 0,20 µL	144	-44,344	383,267	-21,209							
DNS 3 0,21 µL	157,629	-53,262	413,76	-22							
Crush 10A					17,525	5,394	57,285	-18,211	0,38764	95,7	0,60g
DNS 3 0,02 µL	36,259	-92,907	116,118	-19,993							
DNS 3 0,017 µL	21,749	-65,856	74,385	-18,741							

Appendix IV: *Montastrea Annularis* Fluid Data

Sample	Area H2	δ2H	Area CO	δ18O	Area H2	δ2H	Area CO	δ18O	δ18O corr	d2H corr	Weight
24 october 1.1											
DNS 3 0,2 µL	181,139	-82,173	476,417	-23,842							
DNS 3 0,2 µL	165,675	-54,740	435,668	-23,676							
DNS 3 0,2 µL	153,724	-55,318	407,649	-23,078							
DNS 3 0,20 µL	147,761	-51,838	393,656	-23,404							
Crush 1.1					33,842	-25,856	99,232	-19,267	0,42844	58,1	0,45g
DNS 3 0,04 µL	35,566	-88,990	109,481	-21,089							
24 october 1.2											
DNS 3 0,2 µL	239,741	-62,325	626,406	-15,685							
DNS 3 0,2 µL	192,209	-45,224	512,298	8,036							
DNS 3 0,2 µL	159,310	-45,137	423,484	-18,293							
DNS 3 0,20 µL	160,654	-43,560	423,812	-18,821							
Crush 1.2					41,58	-41,302	120,833	-7,861	7,68064	25,1	0,35g
DNS 3 0,045 µL	50,380	-74,284	146,469	-15,379							
DNS 3 0,04 µL	37,806	-73,608	115,700	-16,793							
25 october 1.3											
DNS 3 0,2 µL	154,180	-82,814	404,426	-21,925							
DNS 3 0,2 µL	153,350	-47,177	404,099	-21,972							
DNS 3 0,2 µL	152,916	-56,595	403,321	-22,696							
DNS 3 0,2 µL	146,402	-47,666	386,302	-23,047							
DNS 3 0,21 µL	154,118	-53,105	406,118	-23,339							
Crush 1.2					25,874	-2,589	79,168	-15,519	4,3483	67,9	0,325g
DNS 3 0,03 µL	13,003	-38,046	45,194	-21,505							
DNS 3 0,035 µL	19,095	-74,919	63,316	-21,184							

Sample	Area H2	δ2H	Area CO	δ18O	Area H2	δ2H	Area CO	δ18O	δ18O corr	d2H corr	Weight
25 October 3.1											
DNS 3 0,2 µL	237,831	-67,690	637,477	-18,980							
DNS 3 0,2 µL	184,817	-46,020	496,762	12,619							
DNS 3 0,2 µL	168,450	-50,995	450,015	-20,601							
DNS 3 0,2 µL	157,799	-54,316	420,174	-21,580							
DNS 3 0,20 µL	158,489	-51,263	417,888	-22,187							
Crush 1.2					82,381	42,513	230,664	-14,887	5,25916	35,9	0,500g
DNS 3 0,03 µL	50,380	-74,284	146,469	-15,379							
DNS 3 0,035 µL	78,294	-84,917	217,550	-21,445							
25 october 3.2											
DNS 3 0,2 µL	379,168	-62,010	996,246	-16,087							
DNS 3 0,2 µL	209,165	-47,023	554,463	-18,921							
DNS 3 0,2 µL	179,342	-45,013	475,643	-20,413							
DNS 3 0,2 µL	159,962	-49,537	424,310	-21,140							
Crush 3.2					113,894	-50,53	312,951	-12,04	6,32812	5,7	0,575g
DNS 3 0,14 µL	115,451	-64,737	309,184	-19,646							
28 october 3.3											
DNS 3 0,2 µL	173,569	-85,598	456,643	-22,997							
DNS 3 0,2 µL	144,160	-62,263	379,661	-23,813							
DNS 3 0,2 µL	162,710	-52,519	425,319	-23,640							
DNS 3 0,2 µL	152,875	-57,631	400,912	-23,999							
DNS 3 0,2 µL	202,432	-58,082	525,379	-24,004							
Crush 3.3					40,148	26,315	121,109	-21,276	0,20302	50,9	0,440g
DNS 3 0,03 µL	36,707	-82,804	108,952	-22,877							

Sample	Area H2	δ2H	Area CO	δ18O	Area H2	δ2H	Area CO	δ18O	δ18O corr	d2H corr	Weight
28 october 3.4											
DNS 3 0,2 µL	444,371	-65,353	1153,422	-28,785							
DNS 3 0,2 µL	250,764	-56,246	659,497	-22,787							
DNS 3 0,2 µL	202,512	-50,330	532,929	-22,533							
DNS 3 0,2 µL	161,766	-53,475	443,014	7,072							
DNS 3 0,2 µL	151,613	-50,746	403,169	-22,356							
Crush 3.4					116,905	71,869	324,863	-18,285	2,33482	-23,4	0,480g
DNS 3 0,15 µL	140,333	-63,846	371,673	-21,542							
DNS 3 0,145 µL	119,799	-58,904	323,046	-21,976							
28 october 5,1											
DNS 3 0,2 µL	215,381	-65,214	560,359	-21,255							
DNS 3 0,2 µL	183,781	-50,808	481,083	-21,302							
DNS 3 0,2 µL	166,984	-50,028	440,328	-21,957							
DNS 3 0,2 µL	165,114	-55,379	435,292	-21,790							
DNS 3 0,2 µL	154,511	-41,650	412,529	5,755							
Crush 5,1					42,316	42,005	128,846	-17,513	2,19508	52,7	0,689g
DNS 3 0,05 µL	47,694	-100,128	139,637	-21,067							
29 october 5.2											
DNS 3 0,2 µL	296,981	-72,130	795,975	5,099							
DNS 3 0,2 µL	165,520	-57,415	448,259	-24,994							
DNS 3 0,2 µL	172,687	-68,232	458,387	-23,760							
DNS 3 0,2 µL	133,548	-81,785	356,939	-22,874							
DNS 3 0,2 µL	150,679	-52,129	403,277	-22,319							
Crush 5.2					21,916	11,735	71,12	-19,575	0,51922	72,4	0,720g
DNS 3 0,05 µL	34,268	-80,743	105,316	-21,407							
DNS 3 0,05 µL	30,246	-88,316	93,391	-21,486							

Sample	Area H2	δ2H	Area CO	δ18O	Area H2	δ2H	Area CO	δ18O	δ18O corr	d2H corr	Weight
30 october 6.1	**Sample Eline**										
DNS 3 0,2 µL	325,554	-75,438	878,764	-2,251							
DNS 3 0,2 µL	71,569	-51,383	214,685	-22,228							
DNS 3 0,2 µL	194,113	-71,031	511,031	-23,416							
DNS 3 0,2 µL	179,120	-46,550	473,868	-23,084							
DNS 3 0,2 µL	176,670	-55,917	468,680	-23,226							
DNS 3 0,2 µL	172,184	-57,642	456,061	-23,369							
Crush 6.1					65,694	-60	192,466	-22,396	-0,60176	22,7	0,700g
DNS 3 0,07 µL	70,949	-90,061	196,904	-23,208							
30 october 2.1											
DNS 3 0,2 µL	257,962	-61,210	683,570	21,057							
DNS 3 0,2 µL	188,930	-42,816	502,756	-21,183							
DNS 3 0,2 µL	175,506	-47,446	462,423	-22,150							
DNS 3 0,2 µL	166,531	-44,415	437,724	-22,754							
DNS 3 0,2 µL	169,008	-58,842	446,163	-22,979							
Crush 2.1					29,24	-9,416	95,483	-20,25	0,41008	77,0	0,810g
DNS 3 0,03 µL	33,934	-90,248	104,350	-22,054							
31 october 2.2											
DNS 3 0,2 µL	353,023	-33,793	904,924	-12,731							
DNS 3 0,2 µL	180,264	-17,277	473,097	-18,579							
DNS 3 0,2 µL	173,410	-32,509	451,125	-20,106							
DNS 3 0,2 µL	162,554	-40,911	424,527	-20,877							
DNS 3 0,2 µL	163,543	-35,298	425,896	-21,071							
Crush 2.2					33,955	-15,857	111,876	-14,001	4,49722	49,5	0,650g
DNS 3 0,04 µL	40,125	-72,419	62,141	-19,433							
DNS 3 0,035 µL	33,935	-71,030	105,092	-19,812							

Sample	Area H2	δ2H	Area CO	δ18O	Area H2	δ2H	Area CO	δ18O	δ18O corr	d2H corr	Weight
31 october 2.3											
DNS 3 0,2 µL	207,879	-70,112	538,456	-23,184							
DNS 3 0,2 µL	182,689	-53,766	480,21	-23,136							
DNS 3 0,2 µL	172,729	-58,557	455,222	-23,4							
DNS 3 0,2 µL	175,841	-54,175	464,081	-23,41							
Crush 2.3					32,212	25,393	103,912	-20,39	0,6355	50,8	0,800g
DNS 3 0,03 µL	39,619	-81,737	119,908	-22,415							
31 october 4.1											
DNS 3 0,2 µL	247,697	-57,947	652,098	-1,493							
DNS 3 0,2 µL	186,186	-47,591	489,889	-21,772							
DNS 3 0,2 µL	172,593	-47,064	452,412	-21,982							
DNS 3 0,2 µL	171,395	-46,012	450,57	-22,433							
Crush 4.1					32,669	-2,687	109,87	-16,804	1,89928	87,7	0,800g
DNS 3 0,03 µL	32,977	-93,57	107,57	-20,068							
31 october 4.2											
DNS 3 0,2 µL	236,877	-60,245	617,141	-20,394							
DNS 3 0,2 µL	183,381	-41,858	474,886	-21,272							
DNS 3 0,2 µL	176,882	-43,874	457,955	-21,59							
DNS 3 0,2 µL	169,217	-44,123	440,63	-21,629							
Crush 4.3					36,635	34,681	118,576	-17,185	2,40214	62,6	0,800g
DNS 3 0,03 µL	41,384	-102,03	125,376	-20,942							

Sample	Area H2	δ2H	Area CO	δ18O	Area H2	δ2H	Area CO	δ18O	δ18O corr	d2H corr	Weight
1 november 4.3											
DNS 3 0,2 µL	195,101	-79,055	524,791	-20,742							
DNS 3 0,2 µL	173,8	-53,093	461,361	-21,809							
DNS 3 0,2 µL	165,775	-52,645	439,023	-22,459							
DNS 3 0,2 µL	162,909	-53,232	430,817	-23,103							
Crush 4.3					31,393	-33,899	101,506	-20,939	0,54676	70,2	0,650g
DNS 3 0,035 µL	41,957	-101,571	125,924	-22,949							
DNS 3 0,03 µL	31,254	-108,373	98,698	-22,877							
4 november 7.1											
DNS 3 0,2 µL	158,309	-106,333	415,912	0,221							
DNS 3 0,2 µL	158,514	-63,112	414,106	-24,093							
DNS 3 0,2 µL	163,499	-52,57	427,242	-23,817							
DNS 3 0,2 µL	157,585	-55,737	413,854	-23,884							
Crush 7.1					30,009	-45,671	97,5067	-22,815	0,67018	75,3	0,717g
DNS 3 0,03 µL	32,11	-124,95	99,331	-24,874							
4 november 7.2											
DNS 3 0,2 µL	232,107	-87,067	606,762	-24,826							
DNS 3 0,2 µL	157,309	-67,243	411,714	-24,128							
DNS 3 0,2 µL	148,878	-42,936	393,017	-23,28							
DNS 3 0,2 µL	145,114	-58,021	382,503	-23,631							
Crush 7.2					31,117	-67,657	100,511	-24,334	-0,25496	47,6	0,750g
DNS 3 0,035 µL	34,739	-120,979	103,491	-25,486							

Sample	Area H2	δ2H	Area CO	δ18O	Area H2	δ2H	Area CO	δ18O	δ18O corr	d2H corr	Weight
4 november 7.3											
DNS 3 0,2 µL	366,126	-81,985	961,86	-20,96							
DNS 3 0,2 µL	217,868	-60,643	574,128	-22,581							
DNS 3 0,2 µL	185,243	-51,437	488,925	-22,066							
DNS 3 0,2 µL	171,126	-61,48	448,563	-22,229							
Crush 7.3					49,598	83,007	148,31	-22,97	-0,83024	28,6	0,781g
DNS 3 0,05 µL	55,334	-118,591	158,461	-23,558							